Three-dimensional model for estuarine turbidity maxima in tidally dominated estuaries
An idealized modeling approach

Kumar, Mohit

Important note
To cite this publication, please use the final published version (if applicable).
Please check the document version above.

THREE-DIMENSIONAL MODEL FOR ESTUARINE TURBIDITY MAXIMA IN TIDALLY DOMINATED ESTUARIES

AN IDEALIZED MODELING APPROACH

Three-Dimensional Model for Estuarine Turbidity Maxima in Tidally Dominated Estuaries

An Idealized Modeling Approach

Proefschrift

ter verkrijging van de graad van doctor
aan de Technische Universiteit Delft,
op gezag van de Rector Magnificus Prof. dr. ir. T. H. J. J. van der Hagen,
voorzitter van het College voor Promoties,
in het openbaar te verdedigen op
vrijdag, 30 november 2018 om 15:00 uur

door

Mohit KUMAR

Master of Science in Industrial and Applied Mathematics,
Eindhoven University of Technology, The Netherlands,
geboren te Delhi, India.

Dit proefschrift is goedgekeurd door de

Promotor: Dr. H. M. Schuttelaars
Copromotor: Dr. ir. P. C. Roos

Samenstelling promotiecommissie:

Rector Magnificus	voorzitter
Dr. H. M. Schuttelaars	Technische Universiteit Delft
Dr. ir. P. C. Roos	University of Twente

Onafhankelijke leden:

Prof. dr. ir. T. De Mulder	Ghent University
Prof. dr. H. E. de Swart	Utrecht University
Prof. dr. ir. Z. B. Wang	Technische Universiteit Delft
Prof. dr. ir. J. A. Roelvink	IHE Delft Institute for Water Education
Prof. dr. ir. A. W. Heemink	Technische Universiteit Delft

Overige leden:

Dr. ir. P. C. Roos	University of Twente

Dedicated to my parents

CONTENTS

1

INTRODUCTION

1.1. OUTLINE

Estuaries are water bodies that connect the marine and riverine environments (for a precise definition, see section 1.2); they are ubiquitous features along the world's coastlines. Examples are the Ems estuary along the border of the Netherlands and Germany and the Scheldt estuary at the Dutch-Belgian border.

Estuarine regions have to fulfil many, often conflicting, functions. On the one hand, they are usually economically important regions, containing large harbours and allowing for extensive sand extraction. On the other hand, they also play an important role in our ecosystem: they act as a habitat for thousands of species by providing food, resting and nesting places. Both the economical and ecological functions of the estuaries are strongly affected by anthropogenic changes and climate change. For example, to facilitate economic growth, shipping channels are often deepened. This deepening of navigation channels strongly affects the water motion, which in turn influences the sediment dynamics and trapping of sediments. This can strongly affect the ecological value of the system, and even result in economic adverse effects because of enhanced dredging requirements.

To assess the effects of anthropogenic changes and climate change on sediment dynamics, a clear understanding of the mechanisms resulting in the trapping of sediments is important. Recent literature reveals that these trapping mechanisms show a strong three dimensional character, with a dynamic interplay between longitudinal and lateral processes. Therefore, the aim of this thesis is to develop a three-dimensional idealized model for water motion and sediment dynamics that allows for a systematic analysis of trapping of suspended sediments in tidally dominated estuaries. The trapping of suspended sediments results in an elevated concentration compared to concentrations seaward and landward of this region. Such a local maximum in the sediment concentration is called an Estuarine Turbidity Maximum (ETM).

The structure of this chapter is as follows. The definition and key properties of estuaries are presented in section 1.2, with a special focus on the Ems estuary. In section 1.3,

1

the definition of the estuarine turbidity maximum (ETM) and the motivation to study the three-dimensional profile of ETMs are explained. This section also presents a brief summary concerning the modeling of ETMs. Section 1.4 gives an outline of the thesis, first by posing the research questions to be answered and then describing the research approach being adopted.

1.2. ESTUARIES

1.2.1. INTRODUCTION AND CLASSIFICATION

The word estuary comes from the Greek word *aetus* that means "of the tide" (Jackson [1]), emphasizing that tides play an important role in estuaries. One of the earliest definitions of an estuary was given by Pritchard [2] as: "*a semi-enclosed coastal body of water having a free connection with the open sea and containing a measurable quantity of sea water*". This definition was not generally accepted and resulted in quite some debate. In 1964 (Potter *et al.* [3]), the American Society of the Advancement of Science came up with a more generally accepted definition (Pritchard [4]): "*An estuary is a semi-enclosed coastal body of water which has a free connection with the open sea and within which sea water is measurably diluted with fresh water derived from land drainage (river discharge)*".

As already indicated in the definition, an estuary is a place where the saline water from the ocean mixes with the fresh water from the river. The main sources of mixing are tides, waves and winds. The amount of saline water transported into the estuary and fresh water discharged into it varies per estuary. This results in different salinity structures that allow for a classification. Note that there are many other classifications of estuaries, see for example Valle-Levinson [5] for an overview concerning possible classifications. Here we classify the estuaries with respect to their salinity structure. Four classes of estuaries are usually identified: salt-wedge, strongly stratified, weakly stratified or partially-mixed, and well-mixed (Fig. 1.1).
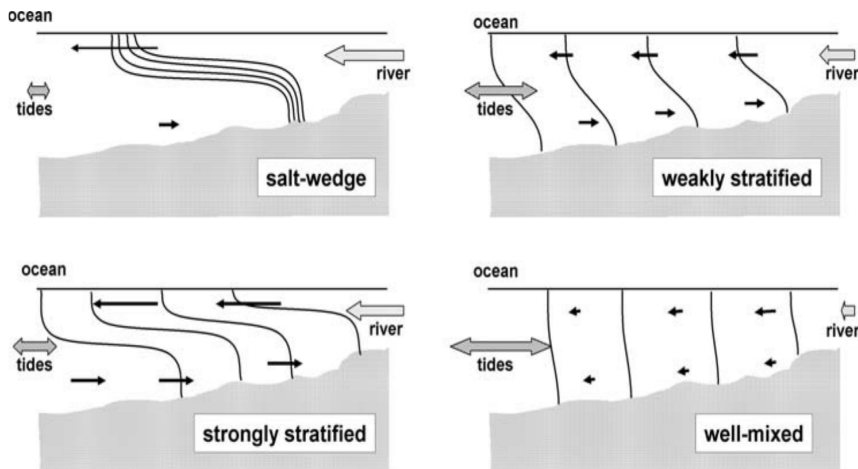
Figure 1.1: Classification of estuaries on the basis of the vertical structure of the salinity, reprinted from Valle-Levinson [5].

Salt-wedge estuary: In this type of estuaries, there is a strong river discharge and small tidal forcing (Fig. 1.1, top left). The strong river discharge pushes the fresh water seaward over the saline seawater, creating a strong pycnocline between the saline water at the bottom and the fresh water at the top. The shape and location of the salt wedge depend on local conditions. Examples of salt-wedge estuaries are the Mississippi (US), Rio de la Plata (Argentina), Vellar (India), and Ebro (Spain).

Strongly stratified estuary: This type of estuaries have moderate to large river discharge and weak to moderate tidal forcing (Fig. 1.1, bottom left). The stratification profile of these estuaries looks similar to that of salt-wedge type estuaries. Examples of strongly stratified estuaries are fjords such as those of British Columbia, Alaska, Chile, New Zealand, and Norway.

Weakly-stratified or partially-mixed estuary: These estuaries are formed by a moderate to strong tidal forcing and weak to moderate river discharge (Fig. 1.1, top right). Some examples of weakly stratified estuaries are the Ems estuary, Chesapeake Bay, and the James River.

Well-mixed or vertically-mixed estuary: The water motion in this type of estuaries is forced by a strong tidal forcing and weak river discharge (Fig. 1.1, bottom right). In these estuaries, the vertical mixing is so strong that the salinity is uniformly distributed in the vertical direction. Examples of such estuaries are the Western Scheldt, the Ems estuary and the Delaware Bay.

In this thesis, we will focus on partially-mixed to well-mixed estuaries. With the help of observational data, it will be shown in section 1.2.2 that the Ems estuary falls in the category of both partially-mixed and well-mixed estuaries.

1.2.2. AN EXAMPLE - THE EMS ESTUARY

The Ems estuary, extensively used as an example in this thesis, is situated on the border of the Netherlands and Germany (see Fig. 1.2). It was formed by the rising sea level after the last ice age that ended 10,000 years ago (Talke and De Swart [6] and references therein). The seaward boundary of the Ems estuary is near the island of Borkum in the North Sea and the landward boundary at the weir in Herbrum. The total length of the estuary is approximately 100 km. The width of the estuary is approximately 30 km at the seaward side (Borkum) and approximately 100 m at the landward side. In this thesis, we focus on the upper part of the Ems estuary, the Ems river, starting from Knock. The length of the Ems river from Knock to the weir at Herbrum is approximately 64 km (Fig. 1.2). The Ems river, the main source (approximately 90%) of the freshwater discharge, drains into the Ems estuary at Herbrum. During the period June - October, the river discharge is approximately 30 m^3 s^{-1}, while during the period November - April, it is approximately 150 m^3 s^{-1}(De Jonge *et al.* [8]).

The Ems estuary is a well-mixed to partially-mixed estuary with tidal range varying between 2 m and 4 m (Dyer *et al.* [10], Talke *et al.* [11]). Figure 1.3 shows the vertical profile of the measured salinity along the axis of the estuary during ebb and flood conditions. During the ebb phase, the salinity is well-mixed throughout the estuary except for the part between 64 km and 70 km where salinity at the bottom is lower than at the
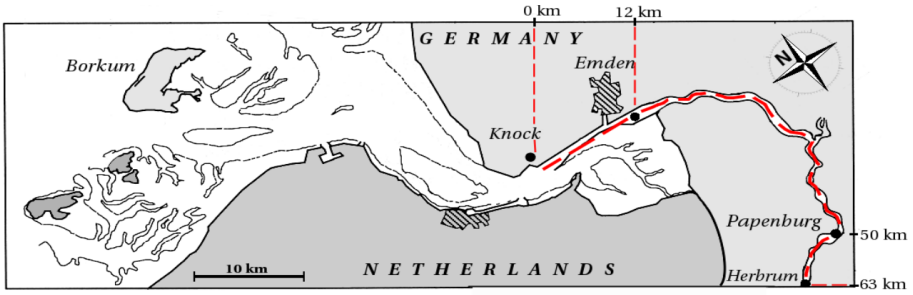
Figure 1.2: Map of the Ems estuary, reprinted from Chernetsky *et al.* [7]. The red dotted line shows the upper part of the Ems estuary considered in this thesis. The block dots show the distance from Knock of few locations in the estuary.

(a) Ebb phase
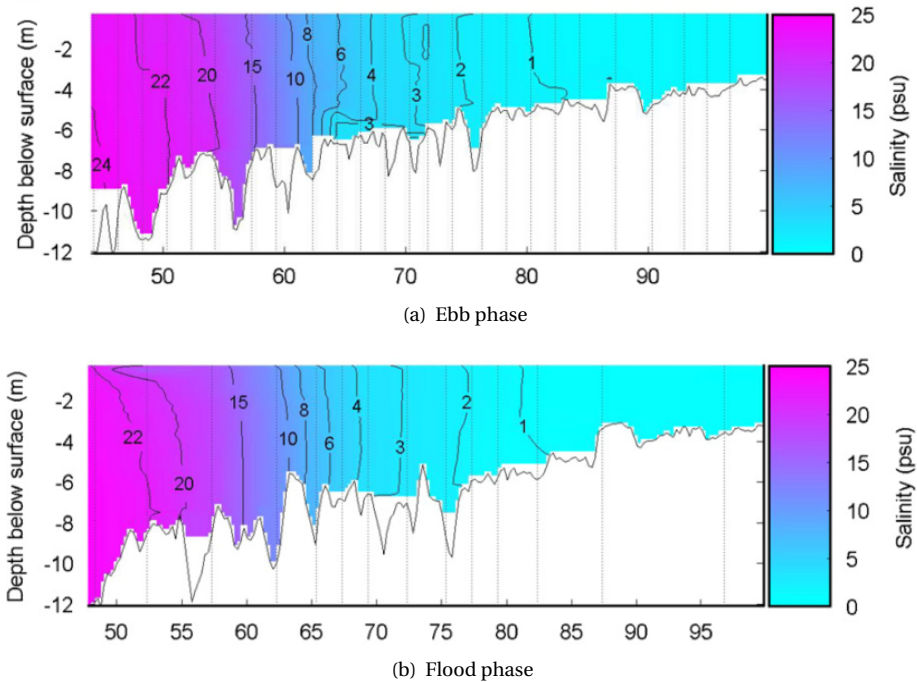
(b) Flood phase

Figure 1.3: Longitudinal distribution of salinity along the axis of the Ems estuary conducted during ebb (*upper panel*, a) and flood (*lower panel*, b) phases, reprinted from Talke *et al.* [9].

surface. During the flood phase of the tide, the salinity is well-mixed throughout the estuary. These data suggest that in the region of interest, the Ems estuary is well-mixed to partially-mixed.

The thalweg depth of the Ems river is shown in Fig. 1.4 for the years 1980 and 2005. This figure demonstrates that the maximum depth of the Ems estuary has increased in this period (1980 - 2005), mainly due to anthropogenic effects.
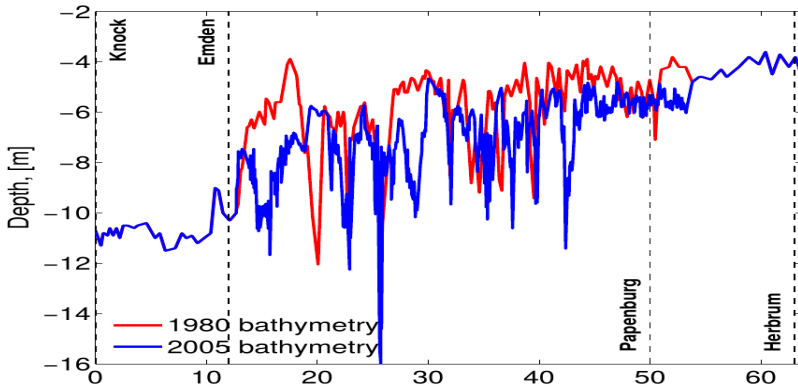
Figure 1.4: Thalweg depth of the Ems estuary for years 1980 (red line) and 2005 (blue line), Chernetsky *et al.* [7].

Anthropogenic changes are mainly triggered by the need to develop and maintain the shipping channels but also gas extraction, sand mining and power plant construction have contributed to it (Talke and De Swart [6]). As shown in Fig. 1.6, there were large channel deepening activities in the Ems river, resulting in a peak of total dredging volumes in the 1970's and 1980's (Van Maren *et al.* [12]). Due to dredging, the morphology of the system changed, which in turn influenced the water motion, sediment transport and concentration (Chernetsky *et al.* [7], Van Maren *et al.* [12], De Jonge [13]).
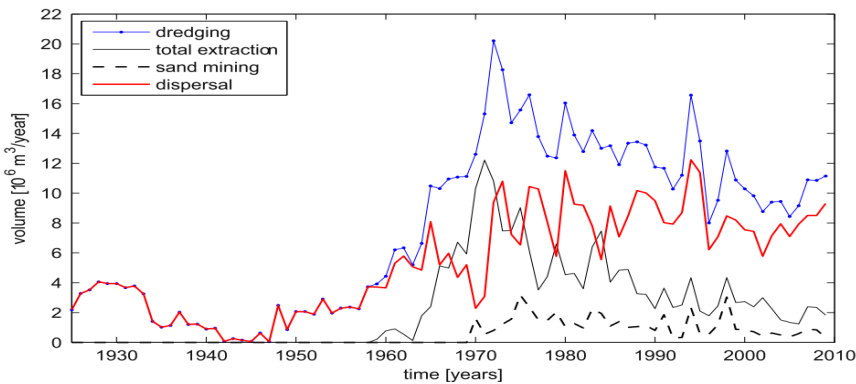
Figure 1.5: Amount of dredging for different years in the Ems estuary, reprinted from Van Maren *et al.* [12].

Apart from anthropogenic changes, there have also been natural changes to the estuarine system due to sea level rise and climate change. The global sea level in the last 100 years has risen by approximately 18 cm (IPCC, 2001). However, in the Ems estuary, the mean sea level rise has remained constant at 10-12 cm/100 years (Jensen *et al.* [15]). Jensen *et al.* [15] suggest a relation between the sea level rise due to climate changes and the increase in the tidal range but this still needs to be validated. There are several other natural factors such as wind, increased temperature, increased river discharge, and
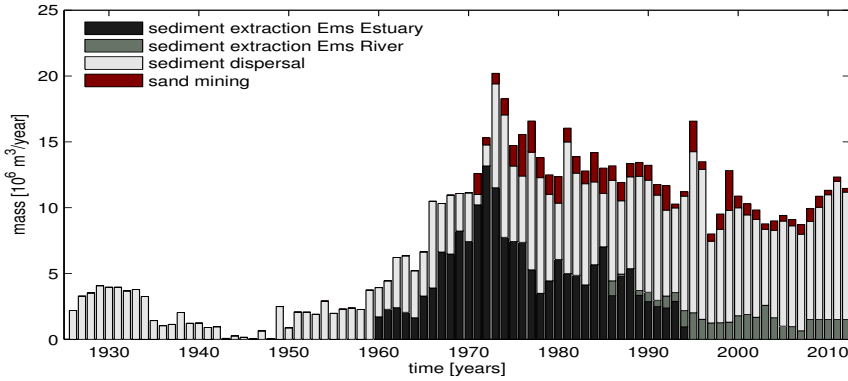
Figure 1.6: Amount of dredging for different years in the Ems estuary, reprinted from Van Maren *et al.* [14].

changes in the wave heights during the last century (Talke and De Swart [6]).

The tidal range in the Ems estuary has increased continuously (Fig. 1.7). For example, in 1980, the tidal range near Knock and Papenburg was 3.1 and 2.3 m, respectively. In 2005, these values increased to 3.2 m and 3.8 m (Chernetsky *et al.* [7]). This increase in the tidal range has resulted in an increased risk of flooding.
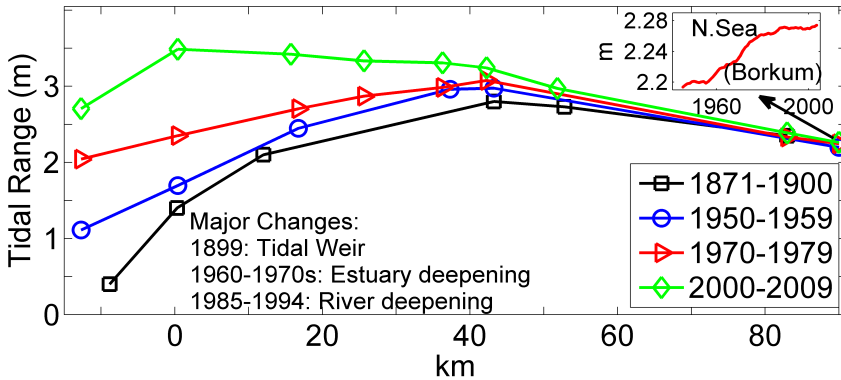
Figure 1.7: Tidal range in the Ems estuary for different years, reprinted from Talke and Jay [16]. Note that 0 km on the *x*-axis indicates the weir at Herbrum.

De Jonge *et al.* [8] compared the measurements of suspended particle matter (SPM) concentration in the Ems estuary at different locations for different years. The measurements were taken at the surface along the main axis of the channel. Figure 1.8 shows that in the lower part of the estuary (Borkum to Emden), the SPM concentration has doubled since 1954. Between Leer and Emden, there has been a strong increase in the concentration of SPM. Considering the whole estuary, the magnitude of SPM concentration has increased by a factor of ten since 1954 and factor of five since 1970. Furthermore, the location of maximum SPM concentration has consistently moved landward. In summary, in the Ems estuary, the SPM concentration has increased and the location of the
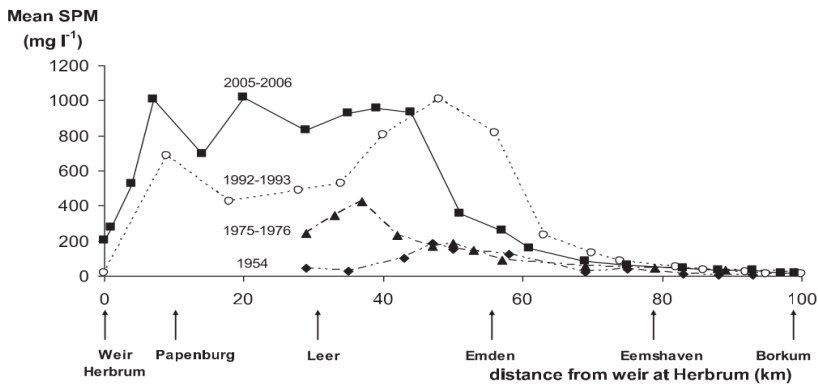
Figure 1.8: Suspended particle matter (SPM) concentration in the Ems estuary for different years, reprinted from De Jonge *et al.* [8].

maximum SPM concentration has moved landward since 1954.

1.3. Estuarine Turbidity Maxima

1.3.1. Definition and Importance

Following Jay *et al.* [17], estuarine turbidity maxima (ETMs) are defined as locations in the estuary where the concentration of suspended sediment is higher than seaward or landward of that location. ETMs are observed in almost all estuaries in the world. Examples of estuaries with ETMs are Chesapeake Bay, Ems estuary (De Jonge *et al.* [8]), Tamar estuary (Uncles and Stephens [18]), San Francisco Bay (Schoellhamer [19]), Humber estuary (Uncles *et al.* [20]), and Gironde estuary (Jalón-Rojas *et al.* [21]). Importantly, the notion of high concentration in the ETM region is estuary specific. For example, the concentration of suspended particle matter (SPM) in the ETM region is of the order 0.1 $g \, l^{-1}$ in the Kennebec estuary (Uncles *et al.* [20]), $0.15 - 1 \, g \, l^{-1}$ in the Columbia River estuary (Jay and Musiak [22]), $1 - 100 \, g \, l^{-1}$ in the Ems estuary (Talke *et al.* [9]) and $200 \, g \, l^{-1}$ in the Severn estuary (Uncles *et al.* [20]). Furthermore, an estuarine system can exhibit more than one ETMs. For example, both the Ems estuary (Chernetsky *et al.* [7]) and the Columbia river estuary (Jay *et al.* [17]) have two ETMs.

As already touched upon in the introduction of this chapter, ETMs can impact both economical and ecological values of estuaries. An ETM located close to a navigation channel makes enhanced dredging of the channel necessary. Changes to the navigation channel, e.g., deepening and/or channelizing, may in return cause the development or result in significant changes in the ETM by changing the physical properties of the system, see for example the decadal development in the Ems estuary (De Jonge *et al.* [8]).

An ETM also plays a crucial role from an ecological point of view. In turbidity maximum zones, light plays a limiting role in the growth of phytoplankton (Lancelot and Muylaert [23] and references therein). Peterson and Festa [24] showed that phytoplankton biomass and productivity is highly influenced by the suspended particle matter (SPM) concentration. Peterson and Festa [24] also suggested that phytoplankton pro-

1

ductivity reduces drastically as SPM concentration increases from 10 to 100 mg l^{-1}. In some cases, an increased phytoplankton population has been found in the region of turbidity maxima (e.g., in San Francisco Bay, Cloern *et al.* [25]). Lancelot and Muylaert [23] suggested that this is most likely caused by the convergence of phytoplankton and is not caused by physiological growth.

1.3.2. PHYSICAL MECHANISMS

The convergence of SPM transport leads to ETM formation (Jay and Musiak [22]). In an estuary, sediment transport can be divided into two categories: bed load transport and suspended load transport. In case of bed load transport, the sediment remains in contact with the bed and movement occurs by virtue of rolling, sliding, hopping or saltating. Bed load transport occurs if sediment is coarse and/or the bed shear stress is low. In case of suspended load transport, the sediment is suspended in the water column where it is transported by advective and diffusive processes. Unlike bed load transport, suspended load transport occurs if the sediment is fine and/or the bed shear stress is high. This is the most common method of sediment transport in estuaries. In this thesis, we focus on transport of fine sediments as suspended load. More information about transport processes is given in Van Rijn [26] and Fredsøe and Deigaard [27].

When considering suspended load transport, the sediment is eroded from the bed by the shear stresses exerted by the water motion on the sediments at the bed. In the water column, turbulent diffusive processes result in an upward transport of the suspended sediments, while gravitational forces transport the sediments towards the bed. This results in specific profiles of suspended sediment concentrations, such as the Rouse profile when assuming parabolic eddy viscosity and diffusivity (see for example Winterwerp and Wang [28]). Once the sediment is in the water column, the sediments are transported in the horizontal direction by diffusive and advective processes. The locations where the suspended load transport converges are often the zones with locally elevated suspended load concentrations, and hence correspond to estuarine turbidity maxima.

The mechanisms resulting in the net sediment transport cover almost the entire spectrum of the hydrodynamic process (Burchard *et al.* [29]). Below a few mechanisms are highlighted:

- An important mechanism that results in a net sediment transport is the *tidal velocity asymmetry*. Tidal velocity asymmetry refers to the phenomenon that the maximum horizontal velocity during the ebb differs from the maximum horizontal velocity during the flood. If the maximum flood velocity is higher than the maximum ebb velocity, net residual transport will be in the flood direction and vice-versa (Bolle *et al.* [30]). This results in an imbalance between the import of sediments during flood and export of sediments during ebb and ultimately in a net sediment transport. Allen *et al.* [31] showed that in some macrotidal estuaries such as the Gironde and the Aulne estuaries, the tidal velocity asymmetry alone can be responsible for creating a sediment convergence zone. Chernetsky *et al.* [7] studied the influence of tidal asymmetry on the sediment trapping in the Ems estuary.

- One of the components of estuarine circulation is related to the density gradients

and is referred to as *gravitational circulation*. Postma and Kalle [32] and Postma [33] showed that this residual circulation could result in sediment trapping at the salt intrusion limit. Using a two-dimensional numerical model, Festa and Hansen [34] verified this hypothesis by producing a convergence zone of sediment from the balance between gravitational circulation and freshwater discharge. Recently, Talke *et al.* [9] extended the model of Festa and Hansen [34] by including the impact of large sediment concentrations on the trapping of sediments.

- *Tidal mixing asymmetry* refers to the asymmetry in the vertical mixing caused by the difference in the magnitude of the ebb and flood velocities (Jay and Musiak [35], Scully and Friedrichs [36]). Winterwerp [37] inferred that in the Ems river, the up-river transport is mainly due to the asymmetry in the vertical mixing. Burchard and Baumert [38] studied the contributions of residual gravitational circulation, tidal velocity asymmetry and tidal mixing asymmetry in the formation of ETM in macrotidal estuaries.

- *Settling lag* is another mechanism that leads to the net sediment transport. Settling lag effects are of two types: temporal (Chernetsky *et al.* [7], Groen [39]) and spatial (Burchard *et al.* [29], Groen [39]). Settling lag is related to the fact that finite time is needed for the suspended particle to settle down (De Swart and Zimmerman [40]).

Apart from the above mentioned mechanisms, other factors such as wind (North *et al.* [41], Weir and McManus [42]), sediment availability (Dickhudt *et al.* [43]), and asymmetry in the size of sediments (Winterwerp [44], Scully and Friedrichs [45], Talke *et al.* [46]) may also impact the location of sediment trapping. The geometrical features of the estuary such as convergence (Talke *et al.* [46], Friedrichs *et al.* [47], Chernetsky [48]) and bathymetric features (Ganju and Schoellhamer [49], Ralston *et al.* [50]) may also play an important role in the strength and the location of the ETM.

1.3.3. Factors Affecting ETM

Due to its importance from both economical and ecological point of view, the understanding of formation and dynamics of ETM becomes essential. The location of maximum turbidity is strongly influenced by river discharge and tidal range. Uncles and Stephens [18] showed that in the Tamar estuary, the location of freshwater-saltwater interface can be captured by a power law relation, depending on the freshwater run-off. Often, for well-mixed and partially-mixed estuary, the location of freshwater-saltwater interface is associated with the location of a turbidity maximum (Uncles and Stephens [18]), implying that the location of turbidity maxima can be related to a power law relation depending on the freshwater run-off. Schoellhamer [19] discussed the influence of salinity, bottom topography and tides on the location of the ETM in San Francisco Bay, USA. In the Gironde estuary, France, the long-term decrease of the river flow resulting from the deepening of the Garonne River has been demonstrated to result in the intensification of the turbidity maximum zone (Jalón-Rojas *et al.* [51]). For Devonshire Avon estuary, UK, Uncles *et al.* [52] showed the influence on water motion and sediment transport due to the construction of an up-stream dam and reservoir. The changes in the

1

water motion were shown to be small but the results indicated an increased transport in the upper part of the estuary and convergence of sediments in the central and upper parts of the estuary. The distribution of suspended particle matter is also influenced by the long term weather, climate and climate change (Fettweis *et al.* [53]). Systematic seasonal variations can also lead to the formation of ETMs. Kessarkar *et al.* [54] showed that in the Mandovi estuary (India), the ETM occurs at the entrance (seaward side) during the two windiest period of the year, showing that wind alone can be responsible for the formation of ETMs.

It has been hypothesized by Winterwerp and Wang [28] and Winterwerp *et al.* [55] that anthropogenic changes in estuaries can result in significant changes to ETM characteristics: by continuous deepening to allow bigger ships to enter the harbors, normal European estuaries can evolve into a hyper turbid state. The authors suggest that the Ems estuary, discussed in section 2.2, has undergone such a 'regime shift', as it has seen a tenfold increase in SPM concentration since 1954. Using observations from different years, De Jonge *et al.* [8] suggested that this increase may have been caused by the deepening of dredged channels in the Ems estuary. Van Maren *et al.* [12] using a numerical model for the Ems estuary concluded that the increase in the suspended sediment concentration in the Ems estuary can be attributed to the deepening of tidal channels and discontinuing of the large-scale sediment extraction near the port of Emden may have contributed to the increased suspended sediment concentration. Contrary to the Ems estuary, Yang *et al.* [56] found that for the Yangtze River estuary, anthropogenic changes had little impact on the water motion resulting in a decrease in sediment volume and concentration.

1.3.4. MODELLING
Transverse distribution of water motion and sediment concentration significantly affects the longitudinal momentum balance and transport of material in many estuaries (Geyer *et al.* [57], Kim and Voulgaris [58]). Therefore, to understand the physical mechanisms resulting in trapping of sediment, it is not enough to study either the longitudinal or lateral processes, but the interaction between these processes has to be studied.

To study the three dimensional formation of ETMs in complex geometries, state-of-the-art complex models such as DELFT3D[1], ROMS[2], and MIKE[3], have been developed. These models solve the complete set of governing equations including all known processes and state-of-the-art parameterizations, allowing for a qualitative comparison between model results and observations. However, because of their complexity, the computation time of these models is often very high which makes this type of models not well-suited for sensitivity studies. Furthermore, it is difficult to assess the relative importance of individual processes on the ETM formation.

Another type of models, the so-called idealized models focuses on the physical processes that are essential to model the phenomenon under investigation, in this case the formation of ETMs. These models do not include all known processes or the most complex parameterizations, resulting in a system of equations that can often be solved by a

[1] https://oss.deltares.nl/web/delft3d
[2] https://www.myroms.org/
[3] https://www.mikepoweredbydhi.com/

combinations of analytical and numerical techniques. Therefore, idealized models are fast to run and thus allow for extensive parameter sensitivity analyses, e.g., influence of channel deepening and sea level rise. Winant [59, 60] developed a three-dimensional model for tidal motion (semi-diurnal and residual) by solving the shallow water equations. In this model, a narrow rectangular estuary with laterally parabolic and axially uniform bed profile was considered. Using scaling and perturbation analysis, an ordered system of linear equations were obtained that could be solved analytically. Ensing *et al.* [61] extended the model of Winant [59] to an exponentially converging domain resulting in a system of equations that could still be solved analytically.

From the above discussion, it follows that three dimensional idealized models developed so far have assumed simplified geometric (rectangular or funnel shaped) and bathymetric (one dimensional in either longitudinal or lateral directions) profiles. Furthermore, these models have only focused on the water motion. Three dimensional idealized modeling of suspended sediment transport and trapping of sediments are completely missing. Hence, the goal of this thesis is to develop a three-dimensional idealized model for trapping of fine sediments in an estuary with arbitrary geometric and bathymetric profiles.

1.4. THIS THESIS

1.4.1. AIM
From the previous section, it follows that the knowledge about formation of ETM in a three-dimensional geometry is still limited. Therefore, the main aim of this thesis is to develop a three dimensional idealized model for ETM dynamics for a partially-mixed to well-mixed estuary with arbitrary bathymetric and geometric profiles, that allows for a systematic analysis of the physical processes resulting in sediment trapping, and the sensitivity of these processes to parameters.

1.4.2. RESEARCH QUESTIONS
The specific research questions addressed in this thesis are:

- *How can the three-dimensional water motion in an estuary with complex shape and bathymetry be decomposed in contributions resulting from different forcing mechanisms*?

- *How can such a model be extended to include the three-dimensional sediment dynamics and sediment trapping, resulting in the formation of ETM*?

- *What is the sensitivity of the trapping location to anthropogenic (e.g., channel deepening) and natural changes (e.g., sea level rise) in a funnel shaped estuary?*

1.4.3. RESEARCH APPROACH
To answer the questions posed above, a three-dimensional idealized model is developed for an estuary with arbitrary geometric and bathymetric profiles. Such a three-dimensional model includes both longitudinal and lateral processes.

1

Furthermore, the idealized modeling approach allows for a decomposition of water motion and sediment dynamics into contributions from different forcing mechanisms and can be used to perform quick and extensive parameter sensitivity analyses.

In the development of this model, the following ingredients are used:

- The water motion is governed by the three-dimensional shallow water equations.

- The suspended sediment concentration follows from a three-dimensional advection-diffusion equation.

- It is assumed that averaged over a tidal time scale, there is no evolution of the bed. In other words, the tidally averaged erosion and deposition processes balance each other. This condition is also referred to as the condition of morphodynamic equilibrium (Friedrichs *et al.* [47]).

Using typical scales of the physical quantities, we begin by making the governing equations dimensionless. This leads to the identification of a small parameter ϵ which is the ratio of the mean water depth (H) and the mean surface elevation (A) at the entrance, i.e., $\epsilon = A/H$. All dimensionless numbers appearing in the dimensionless equations are related to this parameter ϵ. Next, all unknown physical variables such as the water level and the velocity vector are asymptotically expanded in ϵ. After substituting these asymptotic expansions in the system of dimensionless equations, systems of equations at different order of ϵ for both water motion and the suspended sediment concentration are obtained. To get the morphodynamic equilibrium solution, the fine sediment has to be spatially distributed in the estuary such that there are no net convergences or divergences of the suspended sediment transport. This requires a specific spatial variability of the sediment availability. The condition of morphodynamic equilibrium leads to an equation for this specific sediment availability.

To answer the first Research Question, we first focus on the leading-order (linearized) system of equations for the water motion (M_2 tidal constituent) in Chapter 2. Introducing rotating flow variables, the vertical profile of the velocity can be solved analytically while its amplitude depends on the horizontal gradients of the surface elevation. The surface elevation itself follows from a two-dimensional elliptic partial differential equation obtained after integrating the continuity equation over the water column. This equation is solved numerically using the finite element method (Gockenbach [62]). Various methods are discussed to compute the partial derivatives of the numerical solution. A detailed analysis is performed to analyse the convergence of surface elevation and its partial derivatives which are necessary to explicitly obtain the velocity. Finally, the model is applied to the Ems estuary by comparing the model results with observations and model results of a complex state-of-the-art model. The influence of channel convergence on the water motion is briefly discussed.

In Chapter 3, parts of the first and second Research Questions are answered by developing an idealized model that allows for a systematic investigation of sediment trapping. As in chapter 2, rotating flow variables are used to express the velocity in terms of the gradients of the surface elevation of the M_0 and M_4 tidal constituents. The vertical profiles of the leading- and first-order suspended sediment concentrations are expressed

in terms of the leading- and first-order horizontal velocities. The condition of morpho-dynamic equilibrium is used to obtain the availability of easily erodible sediments in the estuary. The first-order surface elevation and sediment availability follow from two-dimensional elliptic differential equations which are solved numerically using the finite element method. Finally, the model is applied to the Ems estuary using parameters representative of the years 1980 and 2005 and the influence of lateral bathymetry on the location of the ETM is studied.

To answer the third Research Question, the model developed in Chapter 2 and 3 is applied to a funnel shaped estuary in Chapter 4. The longitudinal bed profile is obtained by fitting the bathymetric data of the Ems estuary for the year 2005 with a polynomial of degree 4. For the lateral bed profile, we start with a laterally symmetric Gaussian bed profile. Next, the profile in the lateral direction is made asymmetric and the influence of this asymmetric behaviour on the location and strength of ETM is studied. In the next experiment, to understand the influence of shallowing or deepening of the channel, the maximum depth of the channel is decreased or increased. The depths on the lateral sides are kept unchanged. Next, to understand the influence of sea level rise, the overall depth of the channel is increased (including the lateral depths).

Chapter 5 concludes the thesis by summarizing the main results and discussing possible future work.

REFERENCES

[1] N. L. Jackson, *Estuaries,* in *Treatise on Geomorphology,* edited by J. F. Shroder (Academic Press, San Diego, 2013) pp. 308–327.

[2] D. W. Pritchard, *Salinity distribution and circulation in the Chesapeake Bay estuarine system,* Journal of Marine Research **11**, 106 (1952).

[3] I. C. Potter, B. M. Chuwen, S. D. Hoeksema, and M. Elliott, *The concept of an estuary: A definition that incorporates systems which can become closed to the ocean and hypersaline,* Estuarine, Coastal and Shelf Science **87**, 497 (2010).

[4] R. W. Pritchard, *What is an estuary? physical viewpoint,* in *Lauff, G.H. (Ed.), Estuaries* (American Association for the Advancement of Science, 1967) pp. 3–5.

[5] A. Valle-Levinson, ed., *Contemporary issues in estuarine physics* (Cambridge University Press, 2010).

[6] S. A. Talke and H. E. De Swart, *Hydrodynamics and Morphology in the Ems/Dollard Estuary: Review of Models, Measurements, Scientific Literature, and the Effects of Changing Conditions,* Atmospheric Research , 79 (2006).

[7] A. S. Chernetsky, H. M. Schuttelaars, and S. A. Talke, *The effect of tidal asymmetry and temporal settling lag on sediment trapping in tidal estuaries,* Ocean Dynamics **60**, 1219 (2010).

[8] V. N. De Jonge, H. M. Schuttelaars, J. E. E. Van Beusekom, S. A. Talke, and H. E. De Swart, *The influence of channel deepening on estuarine turbidity levels and dy-*

1

namics, as exemplified by the Ems estuary, Estuarine, Coastal and Shelf Science **139**, 46 (2014).

[9] S. A. Talke, H. E. De Swart, and H. M. Schuttelaars, *Feedback between residual circulations and sediment distribution in highly turbid estuaries: An analytical model,* Continental Shelf Research **29**, 119 (2009).

[10] K. R. Dyer, M. C. Christie, N. Feates, M. J. Fennessy, M. Pejrup, and W. van der Lee, *An Investigation into Processes Influencing the Morphodynamics of an Intertidal Mudflat, the Dollard Estuary, The Netherlands: I. Hydrodynamics and Suspended Sediment,* Estuarine, Coastal and Shelf Science **50**, 607 (2000).

[11] S. A. Talke, H. E. De Swart, and V. N. De Jonge, *An idealized model and systematic process study of oxygen depletion in highly turbid estuaries,* Estuaries and Coasts **32**, 602 (2009).

[12] D. Van Maren, T. Van Kessel, K. Cronin, and L. Sittoni, *The impact of channel deepening and dredging on estuarine sediment concentration,* Continental Shelf Research **95**, 1 (2015).

[13] V. N. De Jonge, *Relations Between Annual Dredging Activities, Suspended Matter Concentrations, and the Development of the Tidal Regime in the Ems Estuary,* Canadian Journal of Fisheries and Aquatic Sciences **40**, s289 (1983).

[14] D. S. Van Maren, A. P. Oost, Z. B. Wang, and P. C. Vos, *The effect of land reclamations and sediment extraction on the suspended sediment concentration in the Ems Estuary,* Marine Geology **376**, 147 (2016).

[15] J. Jensen, C. Mudersbach, and C. Blasi, *Hydrological Changes in Tidal Estuaries Due to Natural and Anthropogenic Effects,* in *6th International MEDCOAST 2003 Conference, Ravenna, Italy* (2003).

[16] S. A. Talke and D. A. Jay, *Nineteenth century North American and Pacific tidal data: Lost or just forgotten?* Journal of Coastal Research **291**, 118 (2013).

[17] D. A. Jay, S. A. Talke, A. Hudson, and M. Twardowski, *Developments in Sedimentology,* Vol. 68 (Elsevier B.V., 2015) pp. 49–109.

[18] R. J. Uncles and J. A. Stephens, *The freshwater-saltwater interface and its relationship to the turbidity maximum in the Tamar estuary, United Kingdom,* Estuaries **16**, 126 (1993).

[19] D. H. Schoellhamer, *Influence of salinity, bottom topography, and tides on locations of estuarine turbidity maxima in northern San Francisco Bay,* Coastal and Estuarine Fine Sediment Transport Processes , 343 (2001).

[20] R. J. Uncles, J. A. Stephens, and D. J. Law, *Turbidity maximum in the macrotidal, highly turbid Humber Estuary, UK: Flocs, fluid mud, stationary suspensions and tidal bores,* Estuarine Coastal and Shelf Science **67**, 30 (2006).

[21] I. Jalón-Rojas, A. Sottolichio, H. Schuttelaars, V. Hanquiez, Y. Bichot, S. Schmidt, A. Fort, and B. Villamarin, *Multidecadal evolution of tidal patterns in a highly turbidity macrotidal river and implications for sediment dynamics,* 18th Physics of Estuaries and Coastal Seas Conference, , 5 (2016).

[22] D. A. Jay and J. D. Musiak, *Particle trapping in estuarine tidal flows,* Journal of Geophysical Research **99**, 20,445 (1994).

[23] C. Lancelot and K. Muylaert, *Treatise on Estuarine and Coastal Science*, Vol. 7 (Elsevier Inc., 2012) pp. 5–15.

[24] D. H. Peterson and J. F. Festa, *Numerical Simulation of phytoplankton productivity in partially mixed estuaries,* Estuarine, Coastal and Shelf Science **19**, 563 (1984).

[25] J. E. Cloern, B. E. Cole, R. L. J. Wong, and A. E. Alpine, *Temporal dynamics of estuarine phytoplankton: A case study of San Francisco Bay,* Hydrobiologia **129**, 153 (1985).

[26] L. C. Van Rijn, *Principles of sediment transport in rivers, estuaries and coastal seas,* Aqua Publications , 690 (1993).

[27] J. Fredsøe and R. Deigaard, *Mechanics of coastal sediment transport,* (1992).

[28] J. C. Winterwerp and Z. B. Wang, *Man-induced regime shifts in small estuaries I: theory,* Ocean Dynamics **63**, 1279 (2013).

[29] H. Burchard, H. M. Schuttelaars, and D. K. Ralston, *Sediment Trapping in Estuaries,* Annual Review of Marine Science **10** (2018).

[30] A. Bolle, Z. Bing Wang, C. Amos, and J. De Ronde, *The influence of changes in tidal asymmetry on residual sediment transport in the Western Scheldt,* Continental Shelf Research **30**, 871 (2010).

[31] G. P. Allen, J. C. Salomon, P. Bassoullet, Y. Du Penhoat, and C. De Grandpre, *Effects of tides on mixing and suspended sediment transport in macrotidal estuaries,* Sedimentary Geology **26**, 69 (1980).

[32] H. Postma and K. Kalle, *Die Entstehung von Trübungszonen im Unterlauf der Flüsse, Formatiert: Deutsch (Deutschland) speziell im Hinblick auf die Verhältnisse in der Unterelbe. Dtsch.* Hydrogr. Z. **3**, 138 (1955).

[33] H. Postma, *Sediment transport and sedimentation in the estuarine environment,* (1967).

[34] J. F. Festa and D. V. Hansen, *Turbidity maxima in partially mixed estuaries: A two-dimensional numerical model,* Estuarine and Coastal Marine Science **7**, 347 (1978).

[35] D. A. Jay and J. D. Musiak, *Internal tidal asymmetry in channel flows: Origins and consequences,* in *Mixing in Estuaries and Coastal Seas* (American Geophysical Union, 1996) pp. 211–249.

1

[36] M. E. Scully and C. T. Friedrichs, *The influence of asymmetries in overlying stratification on near-bed turbulence and sediment suspension in a partially mixed estuary,* Ocean Dynamics **53**, 208 (2003).

[37] J. C. Winterwerp, *Fine sediment transport by tidal asymmetry in the high-concentrated Ems River: Indications for a regime shift in response to channel deepening,* Ocean Dynamics **61**, 203 (2011).

[38] H. Burchard and H. Baumert, *The Formation of Estuarine Turbidity Maxima Due to Density Effects in the Salt Wedge. A Hydrodynamic Process Study,* Journal of Physical Oceanography **28**, 309 (1998).

[39] P. Groen, *On the residual transport of suspended matter by an alternating tidal current,* Netherlands Journal of Sea Research **3**, 564 (1967).

[40] H. E. De Swart and J. T. F. Zimmerman, *Morphodynamics of Tidal Inlet Systems,* Annual Review of Fluid Mechanics **41**, 203 (2009).

[41] E. W. North, S. Y. Chao, L. P. Sanford, and R. Hood, *The Influence of Wind and River Pulses on an Estuarine Turbidity Maximum : Numerical Studies and Field Observations in Chesapeake Bay,* Estuaries **27**, 132 (2004).

[42] D. J. Weir and J. McManus, *The role of wind in generating turbidity maxima in the Tay Estuary,* Continental Shelf Research **7**, 1315 (1987).

[43] P. J. Dickhudt, C. T. Friedrichs, L. C. Schaffner, and L. P. Sanford, *Spatial and temporal variation in cohesive sediment erodibility in the York River estuary, eastern USA: A biologically influenced equilibrium modified by seasonal deposition,* Marine Geology **267**, 128 (2009).

[44] J. C. Winterwerp, *On the flocculation and settling velocity of estuarine mud,* Continental Shelf Research **22**, 1339 (2002).

[45] M. E. Scully and C. T. Friedrichs, *Sediment pumping by tidal asymmetry in a partially mixed estuary,* Journal of Geophysical Research: Oceans **112**, 1 (2007).

[46] S. A. Talke, H. E. De Swart, and H. M. Schuttelaars, *An analytical model of the equilibrium distribution of suspended sediment in an estuary,* River, Coastal and Estuarine Morphodynamics , 403 (2008).

[47] C. T. Friedrichs, B. D. Armbrust, and H. E. De Swart, *Hydrodynamics and equilibrium sediment dynamics of shallow, funnel shaped tidal estuaries,* In: Dronkers J, Scheffers MBAM (eds) Physics of Estuaries and Coastal Seas , 315 (1998).

[48] A. S. Chernetsky, *Trapping of sediment in tidal estuaries,* Phd thesis, Delft University of Technology (2012).

[49] N. K. Ganju and D. H. Schoellhamer, *Chapter 24 Lateral variability of the estuarine turbidity maximum in a tidal strait,* Proceedings in Marine Science **9**, 339 (2008).

[50] D. K. Ralston, W. R. Geyer, and J. C. Warner, *Bathymetric controls on sediment transport in the Hudson River estuary: Lateral asymmetry and frontal trapping,* Journal of Geophysical Research: Oceans **117**, 1 (2012).

[51] I. Jalón-Rojas, S. Schmidt, and A. Sottolichio, *Turbidity in the fluvial Gironde Estuary (southwest France) based on 10-year continuous monitoring: sensitivity to hydrological conditions,* Hydrology and Earth System Sciences **19**, 2805 (2015).

[52] R. J. Uncles, J. A. Stephens, and C. Harris, *Towards predicting the influence of freshwater abstractions on the hydrodynamics and sediment transport of a small, strongly tidal estuary: The Devonshire Avon,* Ocean and Coastal Management **79**, 83 (2013).

[53] M. Fettweis, J. Monbaliu, M. Baeye, B. Nechad, and D. Van den Eynde, *Weather and climate induced spatial variability of surface suspended particulate matter concentration in the North Sea and the English Channel,* Methods in Oceanography **3-4**, 25 (2012).

[54] P. M. Kessarkar, V. P. Rao, R. Shynu, P. Mehra, and B. E. Viegas, *The nature and distribution of particulate matter in the Mandovi estuary, central west coast of India,* Estuaries and Coasts **33**, 30 (2010).

[55] J. C. Winterwerp, Z. B. Wang, A. Braeckel, G. Holland, and F. Kösters, *Man-induced regime shifts in small estuaries II: a comparison of rivers,* Ocean Dynamics **63**, 1293 (2013).

[56] Y. Yang, Y. Li, Z. Sun, and Y. Fan, *Suspended sediment load in the turbidity maximum zone at the Yangtze River Estuary: The trends and causes,* Journal of Geographical Sciences **24**, 129 (2014).

[57] W. R. Geyer, R. P. Signell, and G. C. Kineke, *Lateral trapping of sediment in a partially mixed,* in *Physics of Estuaries and Coastal Seas,* edited by J. Dronkers and M. Scheffers, PECS 96 (Balkema, 1998) pp. 155–124.

[58] Y. H. Kim and G. Voulgaris, *Lateral circulation and suspended sediment transport in a curved estuarine channel: Winyah Bay, SC, USA,* Journal of Geophysical Research: Oceans **113**, 1 (2008).

[59] C. D. Winant, *Three-Dimensional Tidal Flow in an Elongated, Rotating Basin,* Journal of Physical Oceanography **37**, 2345 (2007).

[60] C. D. Winant, *Three-Dimensional Residual Tidal Circulation in an Elongated, Rotating Basin,* Journal of Physical Oceanography **38**, 1278 (2008).

[61] E. Ensing, H. E. De Swart, and H. M. Schuttelaars, *Sensitivity of tidal motion in well-mixed estuaries to cross-sectional shape, deepening, and sea level rise,* Ocean Dynamics , 933 (2015).

[62] M. S. Gockenbach, *Understanding and Implementing the Finite Element Method* (Society of Industrial and Applied Mathematics (SIAM), Philadelphia, 2006).

2

THREE-DIMENSIONAL SEMI-IDEALIZED MODEL FOR TIDAL MOTION IN TIDAL ESTUARIES: AN APPLICATION TO THE EMS ESTUARY

This chapter focuses on solving the systems of equations for the leading-order water motion. The vertical profiles of the velocities are obtained analytically in terms of the first-order and the second-order partial derivatives of surface elevation, which itself follows from an elliptic partial differential equation. The surface elevation is computed numerically using the finite element method and its partial derivatives are obtained using various methods. The newly developed semi-idealized model allows for a systematic investigation of the influence of geometry and bathymetry on the tidal motion which was not possible in previously developed idealized models. The new model also retains the flexibility and computational efficiency of previous idealized models, essential for sensitivity analysis.

As a first step, the accuracy of the semi-idealized model is investigated. To this end, an extensive comparison is made between the model results of the semi-idealized model and two other idealized models: a width-averaged model and a three-dimensional idealized model. Finally, the semi-idealized model is used to understand the influence of local geometrical effects on the tidal motion in the Ems estuary. The model shows that local convergence and meandering effects can have a significant influence on the tidal motion. Finally, the model is applied to the Ems estuary. The model results agree well with observations and results from a complex numerical model.

2.1. INTRODUCTION

Estuaries are regions of large economical (navigation channels, sand and gas mining, recreation, etc.) and ecological importance. Recently, various contributions (e.g., Chernetsky *et al.* [1], De Jonge *et al.* [2], Winterwerp *et al.* [3], Winterwerp and Wang [4]) have indicated that tidal characteristics can change significantly due to anthropogenic measures. These changes can endanger safety, i.e., changes in the surface elevation may cause flooding in the surrounding area, and transport (related to the changes in the three-dimensional velocity field) or accumulation of sediments and pollutants which leads to poor quality of water. It is therefore essential to accurately describe and understand the tidal water motion including its response to natural changes and anthropogenic disturbances.

Different types of process-based models can be used to gain understanding of tidal motion (Murray [5], De Vriend [6], De Vriend [7]). These models can be broadly divided into two categories: complex simulation models and idealized models. A complex simulation model aims at resolving all known physical processes, using state-of-the-art parameterizations of unresolved processes. Concerning complex model simulations of the Ems estuary, one can find the studies by Van de Kreeke and Robaczewska [8], Pein *et al.* [9] and Van Maren *et al.* [10]. An idealized model on the other hand considers only those physical processes which are dominant for the phenomenon under investigation. Idealized models use simplified geometric and bathymetric profiles. The schematizations of idealized models allow for quick solution techniques, often analytic, which makes these type of models suitable for extensive parameter sensitivity analysis.

Idealized models, used to study the tidal motion in estuaries, can be further divided into different categories. Averaging the governing equations over the cross-section results in one-dimensional models, see Lanzoni and Seminara [11] and Valle-Levinson [12] for an overview. Ianniello [13] and Chernetsky *et al.* [1] developed width-averaged (2DV) models to gain insight in the vertical flow structure in the longitudinal direction. The geometry was assumed to be exponentially converging, while the depth was assumed constant in Ianniello [13] and varying in the longitudinal direction in Chernetsky *et al.* [1]. Assuming along-estuary uniform conditions, Huijts *et al.* [14] developed an idealized model to study the water motion in an estuarine cross-section, allowing for an arbitrary bathymetry in the lateral direction. To study the interaction of lateral and longitudinal flows, Li and Valle-Levinson [15] used a depth-averaged (2DH) model that allowed for an arbitrary bathymetric and geometric profile, but ignored Coriolis effects. Winant [16] developed a three-dimensional idealized model for tidal motion on a rotating (Coriolis effects included) elongated (width is much smaller than the length) rectangular domain with a parabolic bathymetric profile in the lateral direction together with constant physical parameters and constant density. Winant's three-dimensional idealized model is limited to an estuary with elongated rectangular domain and constant physical parameters.

In light of the above, it is clear that currently there is no idealized model that allows for a systematic investigation of the influence of arbitrary geometry and bathymetry on three-dimensional water motion. Therefore, the aim of this paper is to develop a three-dimensional idealized model for tidal water motion in an estuary with arbitrary geometry and bathymetry. The physical parameters are allowed to vary in the horizontal di-

rection as well. The surface elevation is obtained from a two-dimensional elliptic partial differential equation, which is solved numerically using the finite element method. The vertical profile of the three-dimensional velocity can be explicitly calculated in terms of the first and second-order partial derivatives of the surface elevation, i.e., the three-dimensional velocity profile is analytic in the vertical direction.

This model is a first step in bridging the gap between idealized models and complex models: the model can still be systematically analyzed to gain understanding of important physical mechanisms, but allows for more complex geometries and bathymetries.

Our three-dimensional semi-idealized model is first tested by comparing its results with the results of the width-averaged model of Chernetsky *et al.* [1] and the three-dimensional idealized model of Winant [16]. Extensive error and convergence analyses are performed to evaluate the finite element method and various methods to compute its partial derivatives. Next, the model is applied to the complex geometry of the Ems estuary and the influence of local geometrical effects on the tidal motion is investigated.

The structure of the paper is as follows. The governing equations of the three-dimensional semi-idealized model are described in section 2.2. These equations are solved in section 2.3. The comparison of the three-dimensional semi-idealized model with the width-averaged model is presented in section 2.4 and with the three-dimensional idealized model in section 2.5. Using this novel three-dimensional semi-idealized model, the influence of local geometrical effects on the tidal motion of the Ems estuary are investigated in section 2.6. Finally, conclusions are presented in section 2.7.

2.2. MODEL FORMULATION

We consider a tidal estuary of arbitrary shape and bathymetry (Fig. 3.2), with x and y denoting the horizontal coordinates and z the vertical coordinate pointing upwards. The two-dimensional surface of the estuary is denoted by Ω. Note that, since the shape of the estuary is arbitrary, x (y) need not represent the along-channel (cross-channel) coordinate. The bathymetric profile is denoted by $h(x, y)$, with the mean depth at the seaward side given by H.

The water motion is governed by the three-dimensional shallow water equations, including the Coriolis effect. The estuary is assumed to be partially-mixed or well-mixed. Following Winant [16], the equations are scaled and the physical variables are asymptotically expanded in powers of a small parameter $\epsilon = \tilde{A}/H$, where $\tilde{A}$ is the mean amplitude of the semi-diurnal lunar (M_2) tidal wave at the seaward side. In leading order, i.e., at $\mathcal{O}(\epsilon^0)$, the dimensional system of equations is given by

$$u_x + v_y + w_z = 0, \tag{2.1a}$$

$$u_t - f v = -g\eta_x + (A_v u_z)_z, \tag{2.1b}$$

$$v_t + f u = -g\eta_y + (A_v v_z)_z, \tag{2.1c}$$

where $f = 2\Omega^* \sin\theta$ is the Coriolis parameter, $\Omega^* = 7.292 \times 10^{-5}$ rad s^{-1}, the angular frequency of the Earth's rotation, θ latitude, g is the gravitational acceleration and A_v (m^2 s^{-1}) is the eddy viscosity. At the seaward side (denoted by $\partial_D\Omega$), the system is forced with a prescribed M_2 tide,

$$\eta = A(x, y)\cos\omega t, \quad \forall \quad (x, y) \in \partial_D\Omega, \tag{2.2a}$$

2
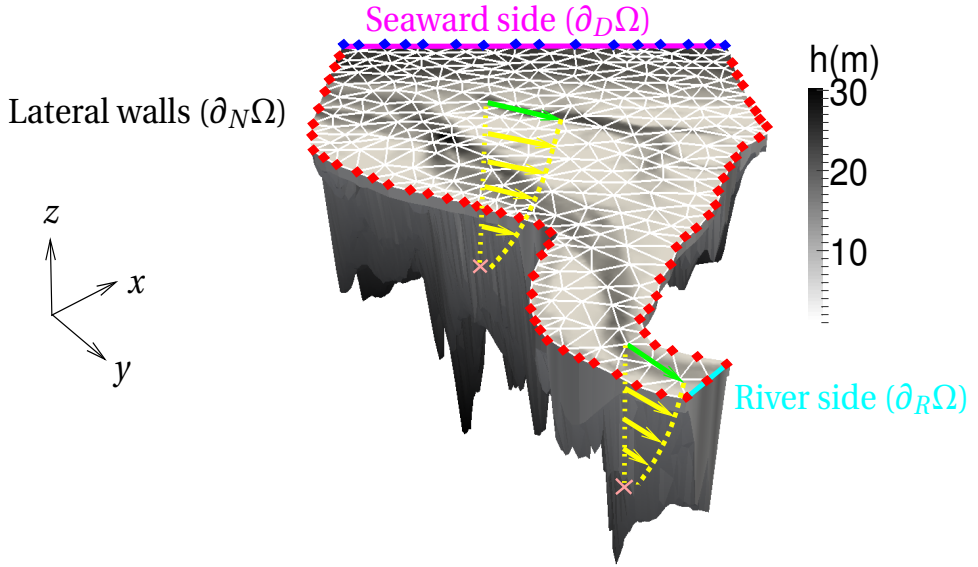
Figure 2.1: Three-dimensional sketch of an estuary with arbitrary geometric and bathymetric profiles. The bathymetric profile is shown on a grayscale. The seaward side (denoted by $\partial_D\Omega$) is shown in magenta color (━━━━━) and the river side (denoted by $\partial_R\Omega$) is shown in cyan color (━━━━━). The other boundaries (denoted by $\partial_N\Omega$) are assumed to be closed walls. The surface of the estuary is discretized using linear triangles in order to compute the surface elevation with the finite element method. The constrained nodes (nodes where the surface elevation is known) are indicated by blue diamonds (◆) and unconstrained nodes (nodes where the surface elevation has to be computed) by red diamonds (◆). All the interior nodes are by default unconstrained. At each node in the triangularization of the surface, the vertical profile of the velocity field can be computed analytically using partial derivatives of the surface elevation as shown by yellow dashed lines (▪ ▪ ▪ ▪ ▪). The velocity at the surface is depicted by green arrows (━━▶) and, in the rest of the water column, by yellow arrows (━━▶).

where $A(x, y)$ is the spatially varying elevation amplitude along this boundary and $\omega = 2\pi/T$ is the tidal frequency of the M_2 tide with tidal period T=12.42 hrs. Also "$\forall (x, y) \in \partial_D\Omega$" means for all points (x, y) on the seaward boundary ($\partial_D\Omega$). At the other boundaries either a no-flux condition (for boundaries denoted by $\partial_N\Omega$) or a river discharge (for boundaries denoted by $\partial_R\Omega$) is prescribed. Assuming that the river outflow gives a minor contribution (only occurring at first order rather than zeroth order in ϵ), the normal component of the volume transport is required to vanish at the remaining boundaries,

$$\left(\int_{-h}^{0} (u, v) \, \mathrm{d}z \right) \cdot \hat{\mathbf{n}} = 0, \quad \forall \quad (x, y) \in \partial_N\Omega \cup \partial_R\Omega, \tag{2.2b}$$

where $\hat{\mathbf{n}}$ is the local unit normal pointing outwards. As dynamic boundary conditions, a no-stress condition at the surface $z = 0$ and a partial slip condition at the bottom $z = -h$

are prescribed, i.e.,

$$A_v(u_z, v_z) = (0,0), \qquad \text{at } z = 0, \tag{2.2c}$$

$$A_v(u_z, v_z) = s(u,v), \qquad \text{at } z = -h, \tag{2.2d}$$

where s (m s^{-1}) is the stress parameter which follows from the linearization of the quadratic friction law (for details, see Schramkowski *et al.* [17] and Zimmerman [18]). In the present model, the eddy viscosity A_v and the stress parameter s are assumed to be constant in the vertical direction and in time. As kinematic boundary conditions, the linearized boundary condition is applied at $z = 0$, and the impermeability of the bottom is imposed at $z = -h$, i.e.,

$$w = \eta_t, \qquad \text{at} \quad z = 0, \tag{2.2e}$$

$$w = -uh_x - vh_y, \quad \text{at} \quad z = -h. \tag{2.2f}$$

2.3. SOLUTION METHOD

The system of equations (2.1), together with the boundary conditions (2.2), constitute a closed set of equations that can be solved for the surface elevation η and velocity components (u, v, w). Usually, this problem is solved numerically by spatial and temporal discretization. In the approach presented below, the tidal motion is solved in terms of tidal constituents, i.e., without discretizing in time. Furthermore, the vertical structure of the velocity components is obtained analytically resulting in a two-dimensional elliptic partial differential equation (section 2.3.1) for the surface elevation that, in general, has to be solved numerically (section 2.3.2).

2.3.1. ANALYTICAL PART OF THE SOLUTION METHOD

Since the water motion is forced by an oscillating water level (Eq. 2.2a) and the system of equations is linear, solutions of the system of equations are of the form

$$(\eta, u, v, w) = \Re\{(N, U, V, W)e^{i\omega t}\}, \tag{2.3}$$

where $\Re$ stands for the real part of a complex variable, and $i = \sqrt{-1}$ is the unit imaginary number. Furthermore, $N(x, y)$, $U(x, y, z)$, $V(x, y, z)$ and $W(x, y, z)$ are the complex amplitudes of the surface elevation and the three velocity components, respectively. Substituting Eq. (2.3) into Eq. (2.1) gives

$$U_x + V_y + W_z = 0, \tag{2.4a}$$

$$i\omega U - fV = -gN_x + A_v U_{zz}, \tag{2.4b}$$

$$i\omega V + fU = -gN_y + A_v V_{zz}. \tag{2.4c}$$

To solve this coupled set of equations, we introduce rotating flow variables R_1 and R_2 with

$$R_1 = U + iV \quad \text{and} \quad R_2 = U - iV, \tag{2.5}$$

such that

$$U = \frac{R_1 + R_2}{2} \quad \text{and} \quad V = \frac{R_1 - R_2}{2i}. \tag{2.6}$$

We add Eq. (2.4c) multiplied by i to Eq. (2.4b) and Eq. (2.4c) multiplied by $-i$ to Eq. (2.4b). These give differential equations for the rotating flow variables:

$$R_{j,zz} - \alpha_j^2 R_j = \frac{g}{A_v} \mathcal{L}_j N, \quad j = 1,2, \tag{2.7a}$$

with differential operators $\mathcal{L}_1 = \partial_x + i\partial_y$, $\mathcal{L}_2 = \partial_x - i\partial_y$, and coefficients $\alpha_1 = \sqrt{i\frac{\omega+f}{A_v}}$, and $\alpha_2 = \sqrt{i\frac{\omega-f}{A_v}}$. Following the same procedure for the boundary conditions, we get,

$$A_v R_{j,z} = 0, \quad \text{at} \quad z = 0, \tag{2.7b}$$
$$A_v R_{j,z} = s R_j, \quad \text{at} \quad z = -h, \tag{2.7c}$$

Here ∂_x and ∂_y are the first-order partial derivatives with respect to x and y, respectively. For each $j = 1,2$, Eq. (2.7a) is a linear, second-order ordinary differential equation in the vertical coordinate z, which can be solved analytically in terms of the unknown pressure gradients N_x and N_y. The resulting rotating flow variables read

$$R_j = c_{\alpha_j}(z) \mathcal{L}_j N, \quad j = 1,2, \tag{2.8}$$

with vertical structure c_{α_j} given by

$$c_{\alpha_j}(z) = \frac{g}{\alpha_j^2 A_v} \left[\frac{s\cosh(\alpha_j z)}{\alpha_j A_v \sinh(\alpha_j h) + s\cosh(\alpha_j h)} - 1 \right].$$

Note that through the (x, y) dependency of the depth h, the stress parameter s and the eddy viscosity A_v, the function c_{α_j} also depends on the horizontal coordinates x and y. Integrating the continuity equation (2.4a) from $z = -h$ to $z = 0$, using the kinematic boundary conditions Eqs. (2.2e) and (2.2f), we find that

$$\partial_x \int_{-h}^{0} U \, dz + \partial_y \int_{-h}^{0} V \, dz + i\omega N = 0. \tag{2.9}$$

To express the depth-integrated horizontal velocity in terms of the surface elevation, define $C_{\alpha_j}(z)$ as

$$C_{\alpha_j}(z) = \int_{-h}^{z} c_{\alpha_j}(z') \, dz'$$

$$= \frac{g}{\alpha_j^3 A_v} \left[\frac{s(\sinh(\alpha_j z) + \sinh(\alpha_j h))}{\alpha_j A_v \sinh(\alpha_j h) + s\cosh(\alpha_j h)} - \alpha_j(z + h) \right].$$

Integrating Eq. (2.8) over the water column from $z' = -h$ to $z' = z$, results in

$$\int_{-h}^{z} R_j \, dz' = C_{\alpha_j}(z) \mathscr{L}_j N, \quad j = 1, 2. \tag{2.10}$$

Combining Eqs. (2.6), (2.8) and (2.10), the depth-integrated horizontal velocities can be expressed as

$$\int_{-h}^{z} U \, dz' = \int_{-h}^{z} \frac{R_1 + R_2}{2} \, dz'$$

$$= \underbrace{\frac{C_{\alpha_1}(z) + C_{\alpha_2}(z)}{2}}_{C_1(z)} N_x + i \underbrace{\frac{C_{\alpha_1}(z) - C_{\alpha_2}(z)}{2}}_{C_2(z)} N_y$$

$$= C_1(z) N_x + C_2(z) N_y, \tag{2.11a}$$

and,

$$\int_{-h}^{z} V \, dz' = \int_{-h}^{z} \frac{R_1 - R_2}{2i} \, dz'$$

$$= -i \underbrace{\frac{C_{\alpha_1}(z) - C_{\alpha_2}(z)}{2}}_{C_2(z)} N_x + \underbrace{\frac{C_{\alpha_1}(z) + C_{\alpha_2}(z)}{2}}_{C_1(z)} N_y$$

$$= -C_2(z) N_x + C_1(z) N_y. \tag{2.11b}$$

Substituting Eqs. (2.11a) and (2.11b) in Eq. (2.9), results in an equation for the surface elevation:

$$\nabla \cdot [\mathbf{D}(0) \nabla N] + i \omega N = 0, \tag{2.12a}$$

with $\nabla = (\partial_x, \partial_y)^{\mathrm{T}}$, where the superscript T denotes the transpose operator, and

$$\mathbf{D}(z) = \begin{bmatrix} C_1(z) & C_2(z) \\ -C_2(z) & C_1(z) \end{bmatrix}. \tag{2.12b}$$

The corresponding boundary conditions read

$$N = A, \quad \text{on} \quad \partial_D \Omega, \tag{2.12c}$$

$$[\mathbf{D}(0) \nabla N] \cdot \hat{\mathbf{n}} = 0, \quad \text{on} \quad \partial_N \Omega \cup \partial_R \Omega. \tag{2.12d}$$

Equation (2.12a) is a two-dimensional linear elliptic partial differential equation with complex coefficient matrix $\mathbf{D}(0)$. This matrix depends on the bathymetric profile h, the eddy viscosity A_v, the stress parameter s, and Coriolis parameter f, all of which can be arbitrary functions of the horizontal coordinates x and y. Therefore, an analytic solution of Eq. (2.12) can not be obtained in general, and a numerical approach will be pursued. In section 2.3.2, the numerical solution procedure will be discussed in detail.

Once the surface elevation $N(x, y)$ is known, we have to calculate its gradients N_x and N_y to obtain the vertical profiles of the horizontal flow components. The vertical velocity W is obtained by integrating the continuity equation (2.4a) from $z' = -h$ to $z' = z$, together with the aid of Leibniz integral rule and the kinematic boundary conditions (Eqs. (2.2e) and (2.2f)), resulting in

$$W = -\partial_x \int_{-h}^{z} U(x, y, z') \, \mathrm{d}z' - \partial_y \int_{-h}^{z} V(x, y, z') \, \mathrm{d}z'$$

$$= -\nabla \cdot [\mathbf{D}(z)\nabla N], \tag{2.13}$$

with $\mathbf{D}(z)$ given by Eq. (2.12b). This completes the derivation of the three-dimensional flow profile expressed in terms of the first-order partial derivatives (for horizontal velocities) and the second-order partial derivatives (for vertical velocity) of the surface elevation.

2.3.2. NUMERICAL PART OF THE SOLUTION METHOD
In general, for an arbitrary domain, bathymetry and spatially varying parameters, Eq. (2.12) cannot be solved analytically. Therefore, a numerical approach, the finite element method (Gockenbach [19]), is adopted. As a first step, Eq. (2.12) is written in its weak form,

$$-\iint_{\Omega} [\mathbf{D}(0)\nabla \tilde{N}] \cdot \nabla \phi \, \mathrm{d}\Omega + i\omega \iint_{\Omega} \tilde{N}\phi \, \mathrm{d}\Omega$$

$$= \iint_{\Omega} [\mathbf{D}(0)\nabla N_D] \cdot \nabla \phi \, \mathrm{d}\Omega - i\omega \iint_{\Omega} N_D \phi \, \mathrm{d}\Omega \quad \forall \, \phi \in \Sigma, \tag{2.14}$$

where $N = \tilde{N} + N_D$, $N_D = A$ on $\partial_D \Omega$ and ϕ is a test function belonging to the space of test functions Σ. Equation (2.14) implies that since N_D is known, the problem of finding N now reduces to finding $\tilde{N}$. Details concerning the derivation of the weak form can be found in Appendix B.2.

Next, the software package `Triangle` (Shewchuk [20]) is used to discretize the domain Ω using triangles (Fig. 3.2). The discretized domain is denoted by $\Omega_{\tilde{h}}$, where $\tilde{h}$ is the mean step size (defined as the mean of the length of all the edges in the discretization of the domain). The total number of nodes equals $n + m$ with the first n nodes located in the interior or on the no-flux boundary (unconstrained or free nodes, denoted by red diamonds in Fig. 3.2 together with all the interior nodes) and the last m nodes located on the seaward boundary (constrained nodes, denoted by blue diamonds in Fig. 3.2). Next, the unknown complex surface elevation amplitude $\tilde{N}$ is approximated by

$$\tilde{N}_{\tilde{h}}(x, y) = \sum_{l=1}^{n} N_l \phi_l(x, y), \tag{2.15}$$

where ϕ_l's are so-called Lagrange basis functions that equal one at node l and zero at all other nodes. The coefficients N_l, $l = 1, \ldots, n$ are unknown complex amplitudes. In this study, we will consider linear and quadratic polynomials as basis functions.

Next, we substitute the finite element approximation of $\tilde{N}_{\tilde{h}}$ (Eq. 2.15) in the weak form (Eq. 2.14) and choose test functions ϕ equal to basis functions ϕ_k, $k = 1, \ldots, n$. This results in a linear system of equations for the unknown N_l's that can be solved numerically (see Appendix B.2 for a detailed explanation). Once $\tilde{N}_{\tilde{h}}$ is known, we can write down the finite element approximation $N_{\tilde{h}}$ of N over the whole domain as,

$$N_{\tilde{h}}(x, y) = \tilde{N}_{\tilde{h}}(x, y) + N_D(x, y)$$

$$= \sum_{l=1}^{n} N_l \phi_l(x, y) + \sum_{l=n+1}^{n+m} A(x_l, y_l) \phi_l(x, y). \tag{2.16}$$

Once we have computed the numerical solution $N_{\tilde{h}}$, its accuracy is assessed by performing error and convergence analyses. Denoting the exact solution of Eq. (2.12a) by N, the error function $E_{\tilde{h}}$ is defined as

$$E_{\tilde{h}} = N - N_{\triangle x}.$$

The numerical solution $N_{\triangle x}$ converges to the exact solution N if

$$||E_{\tilde{h}}||_2 \to 0 \quad \text{as } \tilde{h} \to 0,$$

where $||\cdot||_2$ is the L^2 norm defined in Appendix B.2. To make our error measure independent of the size of the domain and the range of the solution, we define the relative error as

$$r(\tilde{h}) = \frac{||E_{\tilde{h}}||_2}{||N||_2}. \tag{2.17}$$

The order of convergence p is the rate at which the numerical solution $N_{\triangle x}$ converges to the exact solution N, given by

$$p = \frac{\log(||E_{\tilde{h}_1}||_2 / ||E_{\tilde{h}_2}||_2)}{\log(\tilde{h}_1 / \tilde{h}_2)}. \tag{2.18}$$

In general, if polynomial basis functions of order q are used, the numerical solution $N_{\triangle x}$ converges to the exact solution N with rate $q + 1$, provided numerical integrals are computed accurately enough (Gockenbach [19]). For linear (quadratic) basis functions, we thus expect second (third) order convergence of the numerical solution.

To compute the three-dimensional flow components, the first-order and the second-order partial derivatives of N have to be computed. Since the surface elevation itself is obtained numerically using the finite element method, its partial derivatives have to be obtained numerically as well. It is therefore essential to determine these derivatives as accurately as possible to get accurate velocity fields.

The most straightforward way to compute the partial derivatives is the direct derivative method (from now on denoted by DD-method) in which the numerical approximation given by Eq. (2.16) is differentiated directly, i.e.,

$$\frac{\partial^{a+b} N_{\tilde{h}}}{\partial x^a \partial y^b} = \sum_{l=1}^{n} N_l \frac{\partial^{a+b} \phi_l}{\partial x^a \partial y^b} + \sum_{l=n+1}^{n+m} A(x_l, y_l) \frac{\partial^{a+b} \phi_l}{\partial x^a \partial y^b},$$

where a and b are the order of differentiation in the x and y directions, respectively. When linear basis functions are used, it is only possible to calculate the first-order partial derivatives. Hence, the vertical velocity W can not be reconstructed. For this reason, we use quadratic basis functions. The quadratic basis functions allow both the first-order and the second-order partial derivatives to be computed at minimum computational cost. Hence, the three components of the velocity can be computed.

A main drawback of the DD-method is that for each order of differentiation, the order of convergence of the resulting derivative decreases by one. For quadratic basis functions, the numerical solution for N is expected to converge with rate three. The first-order and the second-order partial derivatives calculated using the DD-method are then expected to converge with rates two and one, respectively.

In the literature, various methods (Carey [21], Zienkiewicz and Zhu [22], Zienkiewicz and Zhu [23], Ilinca and Pelletier [24]) are proposed to recover partial derivatives more accurately than with the DD-method. For the problem under consideration, the method proposed by Carey [21] only resulted in superconverging (converging faster than expected) partial derivatives on a structured grid. For unstructured grids, the method failed to converge. The method proposed by Ilinca and Pelletier [24] did not produce superconverging results even for a structured grid.

The method proposed by Zienkiewicz and Zhu [22] (from now on denoted by ZZ-method) was shown to produce superconverging results for the first-order partial derivatives of a numerical solution calculated using linear basis functions. Here, we will apply the ZZ-method twice to compute the first-order and the second-order partial derivatives of a numerical solution calculated using quadratic basis functions. In the literature, no proof exists that using the ZZ-method recursively gives accurate results.

Apart from the two approaches discussed above, the DD-method and the ZZ-method, we combine these two methods to compute the second-order partial derivatives of the numerical solution obtained using quadratic basis functions. This new method works as follows. First, the DD-method is used to calculate the first-order partial derivatives. The ZZ-method is then used on these first-order partial derivatives to obtain the second-order partial derivatives. By doing so, the recursive use of the ZZ-method is avoided. We refer to this method as the mixed-method.

In summary, the surface elevation in our model is computed using either linear or quadratic basis functions. When linear basis functions are used, it is only possible to compute the first-order partial derivatives either by the DD-method or the ZZ-method. For quadratic basis functions, it is possible to compute both the first-order and the second-order partial derivatives. The first-order partial derivatives can be computed either by the DD-method or the ZZ-method. For the second-order partial derivatives, either of the DD-method, the ZZ-method or the mixed-method can be used. The order of convergence of the surface elevation and its partial derivatives calculated using various methods will be assessed in section 2.4.

2.4. Comparison with a width-averaged model

2.4.1. Introduction and geometry

Chernetsky *et al.* [1] developed a width-averaged (2DV) model for an exponentially con-

verging estuary (Fig. 2.2). The width is given by $B(x) = B_0 e^{-x/L_b}$, with $2B_0$ the width at the entrance and L_b the e-folding length scale. The along-channel coordinate x varies from $x = 0$ at the seaward side to $x = L$ at the landward side, with L being the length of the estuary. The lateral boundaries are located at $y = -B(x)$ and $y = B(x)$. If $L_b \to \infty$, the exponentially converging domain becomes a rectangular domain with a constant width of $2B_0$. The governing equations for the 2DV model are obtained by averaging the three-
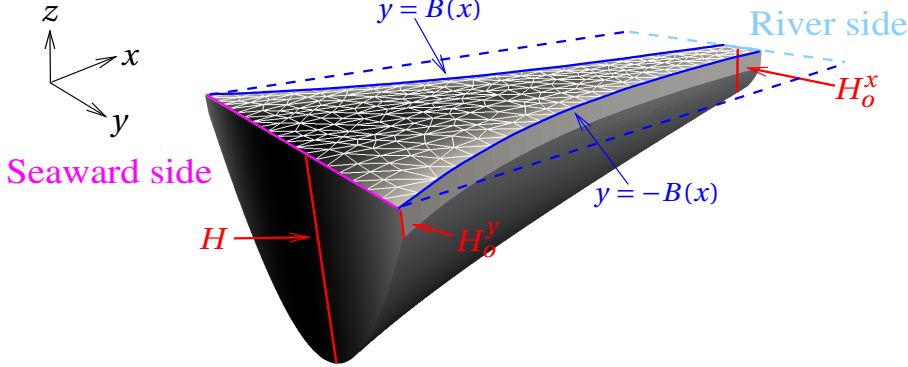
Figure 2.2: Sketch of the idealized geometry used by Chernetsky *et al.* [1]. The width B varies exponentially as $B(x) = B_0 e^{-x/L_b}$, where $2B_0$ the total width at the entrance and L_b the e-folding length (blue solid line, ▬▬▬). If $L_b \to \infty$, the exponential domain becomes a rectangular domain (blue dashed line, ■ ■ ■ ■ ■). The bed profile varies parabolically in the transverse direction (maintaining a constant lateral depths of H_o^y at $y = \pm B$) and linearly in the longitudinal direction, with a depth of H at the entrance ($x = 0, y = 0$) and H_o^x at the end ($x = L, y = 0$).

dimensional continuity and momentum equations (given by Eq. 2.1) over the width, using the appropriate boundary conditions. Similar to the approach in section 2.3.1, the vertical profile of the velocities is calculated analytically. The velocities themselves are proportional to the first and second order derivatives of the surface elevation.

If the bed profile h and physical parameters are allowed to vary in the along-channel direction, the surface elevation has to be obtained numerically (which is done using standard numerical techniques). For a uniform bed profile and spatially uniform physical parameters, an analytical solution of the 2DV model can be obtained.

To reproduce the results of a 2DV model by our 3D semi-idealized model, the Coriolis parameter f in our model is set to zero. In addition to that, the bathymetry and physical parameters are only allowed to vary in the along-channel direction. The results of the 3D semi-idealized model are averaged over the width for a fixed longitudinal coordinate to allow for a comparison of the results obtained with the 2DV model. The one-dimensional width-averaged surface elevation is calculated from the two-dimensional surface elevation $N(x, y)$ obtained from the 3D semi-idealized model as

$$\bar{N}(x) = \frac{1}{2B(x)} \int_{-B(x)}^{B(x)} N(x, y) \, \mathrm{d}y, \tag{2.19}$$

with $\bar{N}$ the one-dimensional width-averaged surface elevation.

2

2.4.2. VALIDATION AND CONVERGENCE ANALYSIS

In this section, the results of the 2DV and 3D semi-idealized models are compared. The convergence properties of the numerical scheme are also investigated. A channel of uniform width ($L_b \to \infty$ limit of exponentially converging domain) of length $L = 50$ km and total width $2B = 1000$ m, together with a uniform bed profile of constant depth of 10 m, is considered. The eddy viscosity A_v is set to 0.01 m^2 s^{-1}.

SURFACE ELEVATION

In Fig. 2.3, the surface elevation is compared for different values of the stress parameter s ranging from a no-slip condition ($s \gg 1$), to a moderate value ($s = 0.01$ m s^{-1}), to a free-slip condition ($s = 0$ m s^{-1}). The domain is discretized using right-angled triangles with 24 nodal points in the along-channel direction and 20 nodal points in the cross-channel direction. For all three values of the stress parameter, the results obtained with the 3D semi-idealized model for both the amplitude and the phase of the surface elevation agree well with those obtained with the 2DV model.
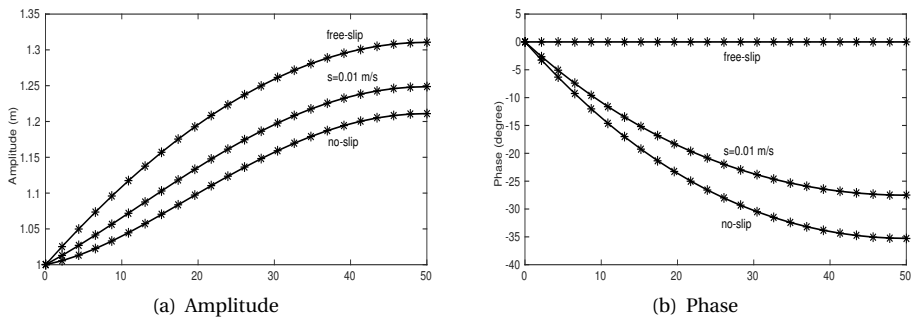
(a) Amplitude   (b) Phase

Figure 2.3: Comparison of 3D semi-idealized and 2DV model results for the amplitude (*left panel*) and the phase (*right panel*) of the surface elevation for different values of the stress parameter. The 3D semi-idealized model result is shown using black asterisks (*) and the 2DV model result is denoted by the solid black line (-).

To investigate the convergence properties of the numerical solution, we systematically increase the number of nodes using an unstructured grid, i.e., the triangles need not be right-angled. Results are compared for $s = 0.01$ m s^{-1}. With both linear and quadratic basis functions, the relative error defined in Eq. (2.17) decreases for an increasing number of nodes (Fig. 2.4(a)). For approximately $10^{4.2}$ nodes, using quadratic basis functions, the relative error approaches computer accuracy and decreases only slowly afterwards. Note that for the same number of nodes, the relative error using quadratic basis functions is at least 100 times smaller than the relative error found with linear basis functions. The order of convergence for linear basis functions converges to 2 (Fig. 2.4(b), red line), and for quadratic basis functions, the order of convergence converges to 3 (Fig. 2.4(b), blue line). For the number of nodes larger than $10^{4.2}$, the order of convergence for quadratic basis functions decreases due to the slow decrease in the relative error related to computer accuracy. To conclude, the numerical solution for the surface elevation converges with the expected order of convergence for both linear and quadratic basis functions.

(a) Relative error   (b) Order of convergence
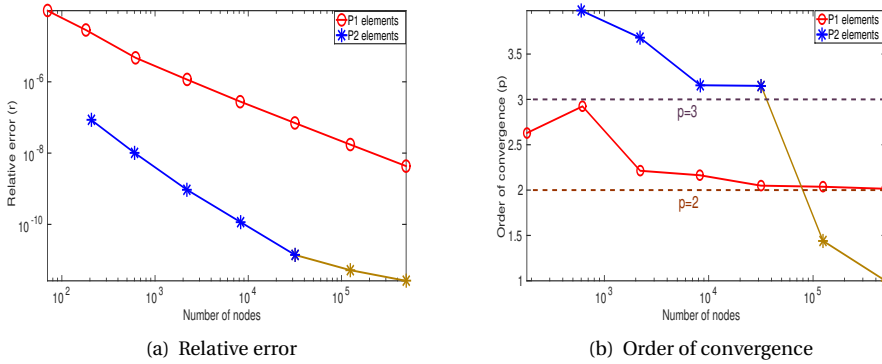
Figure 2.4: Relative error (*left panel*) and order of convergence (*right panel*) for the surface elevation of the 3D semi-idealized model. The red line shows the results for linear basis functions (P1 elements) and blue line for quadratic basis functions (P2 elements). The golden line over the blue line for P2 elements depicts the behavior of relative error and order of convergence after the solution has reached the computer accuracy. The values $p = 2$ and $p = 3$ (*right panel*) indicate the order of convergence of the finite element method for linear and quadratic basis functions, respectively.

FLOW FIELD

In Fig. 2.5, the absolute values of the horizontal and vertical velocities from the 2DV and 3D semi-idealized models are plotted. The domain is discretized using right-angled triangles with 2000 nodes in the along-channel direction and 40 nodes in the cross-channel direction. Quadratic basis functions together with the mixed-method are used to calculate the surface elevation and its first-order and second-order partial derivatives. Figure 2.5 shows that the 3D semi-idealized model is able to reproduce the amplitudes of the horizontal and vertical velocities of the 2DV model.

To assess the accuracy of these velocities, the convergence properties of the first-order and the second-order partial derivatives will be examined. As explained in section 2.3.2, only the first-order partial derivatives of the surface elevation can be obtained when linear basis functions are used. With quadratic basis functions, both the first-order and the second-order partial derivatives can be computed.

We first consider linear basis functions to compute the surface elevation. Both the DD-method and the ZZ-method are used to compute the first-order partial derivative of the surface elevation in the along-channel direction. Figure 2.6(a) shows that the relative error for the first-order partial derivative of the surface elevation decreases with increasing number of nodes for both the DD-method and the ZZ-method. The relative error for the ZZ-method is approximately 10 times smaller than that of the DD-method. Concerning the order of convergence, the ZZ-method converges at a faster rate than the DD-method. Increasing the number of nodes shows that the order of convergence for both methods approaches 1 (Fig. 2.6(b)). There is a loss of one order of accuracy compared to the second order convergence of the surface elevation for linear basis functions. Clearly, the ZZ-method is more accurate than the DD-method both in terms of the relative error and the order of convergence of the first-order partial derivatives of the surface

(a) $|U|$ (2DV model)

(b) $|W|$ (2DV model)

(c) $|U|$ (3D semi-idealized model)

(d) $|W|$ (3D semi-idealized model)
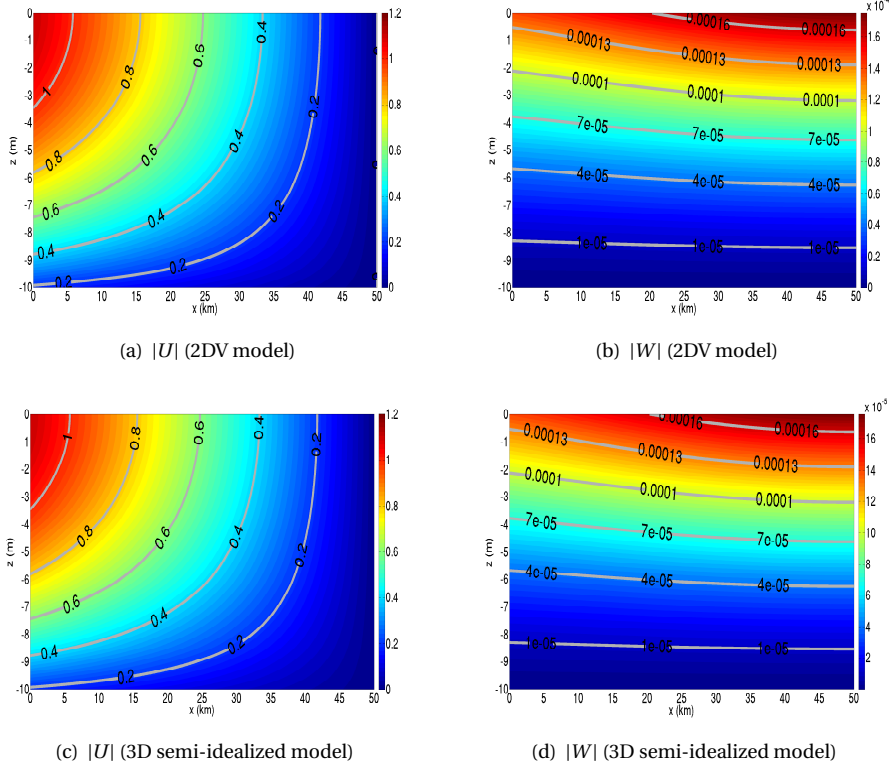
Figure 2.5: Amplitudes of the horizontal (*left panel*) and vertical velocities (*right panel*) computed using 3D semi-idealized (*lower panel*) and 2DV (*upper panel*) models. The units for the colorbars are m s^{-1}.

elevation.

Considering the quadratic basis functions, the convergence of both the first-order and the second-order partial derivatives can be assessed. The ZZ-method and DD-method are applied to compute the relative error for the first-order partial derivatives of the surface elevation. Figure 2.7(a) shows that the relative error for the DD-method decreases with an increasing number of nodes. However, when using the ZZ-method, the relative error decreases up to approximately $10^{4.2}$ nodes and then starts to increase. Ignoring the last two entries of the ZZ-method, both methods converge with order 2 (Fig. 2.7(b)). Unlike linear basis functions (Fig. 2.6), there is only a small gain in using the ZZ-method over the DD-method for calculating the first-order partial derivatives with quadratic basis functions.

As discussed in section 2.3.2, the second-order partial derivatives can be computed in three ways: 1) DD-method, 2) ZZ-method and 3) mixed-method. Figure 2.7(c) shows that the relative error for the DD-method and the mixed-method decrease monotonically with increasing number of nodes. The relative error for the mixed-method is approximately a factor 10 smaller than the relative error found with the DD-method. Fur-

(a) Relative error

(b) Order of convergence
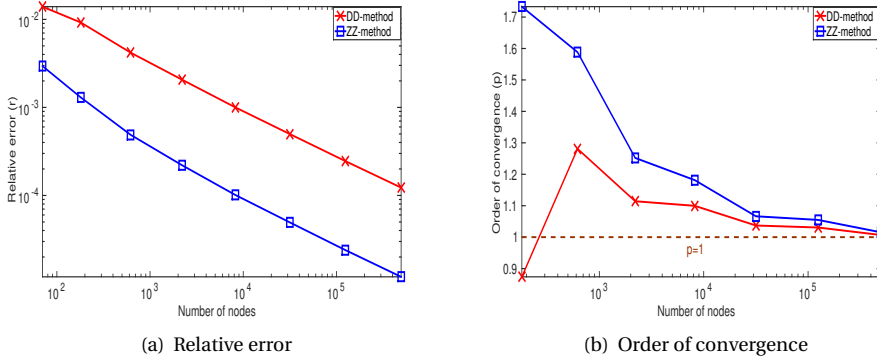
Figure 2.6: Relative error (*left panel*) and order of convergence (*right panel*) for the first-order partial derivative of the surface elevation in the along-channel direction for linear basis functions. The red line shows the results for the DD-method and blue line for the ZZ-method. The middle brown line in the right panel shows that both the methods converge to $p = 1$.

(a) Relative error

(b) Order of convergence

(c) Relative error

(d) Order of convergence
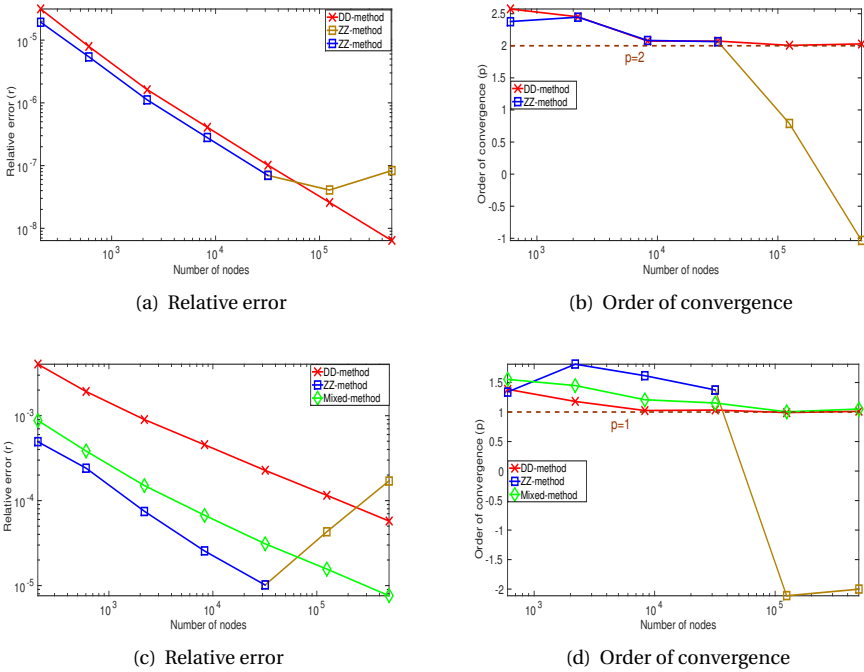
Figure 2.7: Relative error (*left panel*) and order of convergence (*right panel*) for the first-order (*upper panel*) and the second-order (*lower panel*) partial derivatives of the surface elevation in the along-channel direction for quadratic basis functions. The red line shows the results for the DD-method, blue line for the ZZ-method and green line for the mixed-method (only for second-order partial derivatives).

thermore, the mixed-method converges faster than the DD-method. Up to $10^{4.2}$ nodes, i.e., as long as the relative error of the ZZ-method decreases, the ZZ-method gives the most accurate results both in terms of the relative error and the order of convergence. However, the relative error of the ZZ-method starts to increase when further increasing the number of nodes, which makes it unreliable for use. All three methods ultimately appear to converge with order 1.

At this point, it is important to mention that for quadratic basis functions, the unreliable behavior of the ZZ-method for computing the first-order and the second-order partial derivatives with sufficiently large number of nodes is independent of the choice of the bed profile. Similar convergence tests for the ZZ-method were carried out using non-uniform bathymetric profiles with quadratic basis functions, resulting in a similar behavior of the ZZ-method.

To conclude, when using the linear basis functions, the ZZ-method is recommended to compute the first-order partial derivatives. For quadratic basis functions, the DD-method for the first-order partial derivatives and the mixed-method for the second-order partial derivatives are recommended.

2.4.3. PARAMETER SENSITIVITY

To investigate the influence of the geometry, the width at the entrance B_0 will be varied in section 2.4.3, keeping the e-folding length L_b constant. The influence of the variations in the bathymetry will be studied in section 2.4.3. To compute the numerical solution of the 3D semi-idealized model, the domain under consideration is discretized using an unstructured triangular mesh with approximately 400,000 nodal points. Choosing such a fine mesh minimizes the numerical error in the 3D semi-idealized model. The eddy viscosity A_v and stress parameter s are set to 0.01 m^2 s^{-1} and 0.01 m s^{-1}, respectively.

INFLUENCE OF WIDTH AT THE ENTRANCE

To study the influence of the width at the entrance B_0 on the surface elevation in isolation, an exponential domain of length $L = 50$ km and an e-folding length $L_b = 10$ km together with a flat bed profile of 10 m depth is considered. The width at the entrance B_0 is varied and the width-averaged surface elevations obtained with the 2DV and 3D semi-idealized models are compared.

In Fig. 2.8(a), the width-averaged surface elevation (given by Eq. 2.19) is shown for different values of the width B_0 at the entrance. For $B_0 = 2.5$ km, both the 2DV and 3D semi-idealized models produce similar results for the amplitude of the surface elevation. It is important to note that the one dimensional surface elevation from the 2DV model is independent of the width at the entrance (B_0). Because of this, the amplitude of the surface elevation for any value of B_0 will be the same for a 2DV model. As B_0 increases, the width-averaged amplitude of the surface elevation obtained with the 3D semi-idealized model starts to deviate from the results obtained from the 2DV model. This deviation increases with increasing value of B_0. For a width $B_0 = 40$ km, a deviation of approximately 10% is observed.

To understand the cause of this deviation, the amplitude of the surface elevation obtained with the 3D semi-idealized model is plotted in the horizontal space for different values of B_0. It is clear from Figs. 2.8(b), 2.8(c), and 2.8(d) that the solution is radially

(a) Width averaged amplitude

(b) 3D semi-idealized model, B_0=2.5 km

(c) 3D semi-idealized model, B_0=10 km

(d) 3D semi-idealized model, B_0=40 km
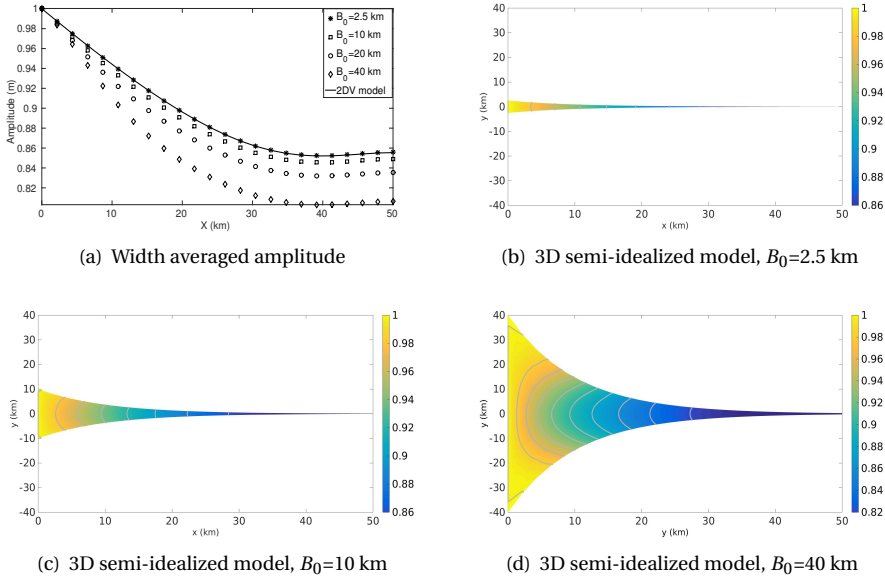
Figure 2.8: (*Top left panel*) Amplitude of the width-averaged surface elevation for different values of B_0. The solid black line shows the results for the 2DV model. The lines with markers show the width-averaged results for the 3D semi-idealized model for different values of B_0. (*Top right and bottom panel*) Two-dimensional amplitude of the surface elevation plotted in the horizontal space for different values of B_0. The unit in the colorbar is m.

constant away from the entrance. At the entrance, a constant surface elevation has been prescribed, which as it breaches the radial symmetry, results in the non-uniformity close to the entrance.

INFLUENCE OF VARYING BATHYMETRY

A rectangular channel of length L = 50 km and width $2B_0$ = 1000 m is considered. A parabolic bed profile is adopted,

$$h = H_o^y + (H - H_o^y)(1 - y^2/B^2), \tag{2.20}$$

where H_o^y is the constant depth at the lateral sides ($y = \pm B$) and H is the maximum depth which is attained at the center line ($y = 0$) of the channel. To use the 2DV model, this bathymetric profile is averaged over the width, resulting in

$$\bar{h} = \frac{1}{2B} \int_{-B}^{B} h \, \mathrm{d}y = \frac{1}{3} \left[H_o^y + 2H \right]. \tag{2.21}$$

In Fig. 2.9, the water depth at the sides is varied from 1 m to 10 m (which is a channel with uniform bed again), and the difference between the amplitude of the width aver-aged surface elevation obtained with the 2DV and 3D semi-idealized models is shown.
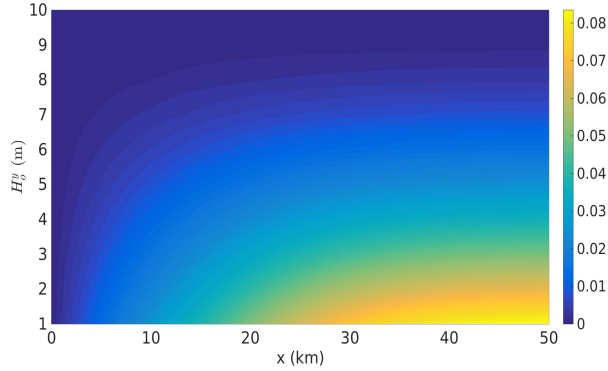
Figure 2.9: Difference in the amplitude of the surface elevation between the 3D semi-idealized and 2DV models. The unit in the colorbar is m.

For $H_o^y = 1$ m, a difference of approximately 8 cm in amplitude of the surface elevation towards the landward side is found. For each value of H_o^y, the difference in the amplitude increases along the channel. As H_o^y increases, the difference in the amplitude decreases. The positive value for the difference of amplitudes shows that the amplitude of the surface elevation from the 3D semi-idealized model is always larger than that of the 2DV model.

2.5. COMPARISON WITH THREE-DIMENSIONAL ASYMPTOTIC MODEL

2.5.1. INTRODUCTION AND GEOMETRY

Winant [16] developed a three-dimensional idealized model for an *elongated* rectangular basin of length L and width $2B$. The along-channel coordinate x varies from $x = 0$ at the seaward side to $x = L$ at the landward side. The cross-channel coordinate y varies from $y = -B$ at the lower boundary to $y = B$ at the upper boundary. The term elongated implies that the horizontal aspect ratio $\alpha = B/L$ has to be small. A no-slip condition is imposed at the bottom $z = -h$. This limit is found by taking $s \to \infty$ in our 3D semi-idealized model. The eddy viscosity A_v is assumed to be spatially uniform. The bed profile given by Eq. (2.20) is used (see Fig. 2.2).

The surface elevation N follows from Eq. (2.12), but Winant [16] uses a different solution method. Assuming that $\alpha \ll 1$, an asymptotic expansion of N in α is made;

$$N = N_0 + \alpha N_1 + \mathcal{O}(\alpha^2), \tag{2.22}$$

and substituted in Eq. (2.12). This results in a system of equations for various orders of α, such that the leading order (N_0) and the first order (N_1) solutions can be calculated analytically. The surface elevation is approximated by

$$N \approx N_0 + \alpha N_1 = N_{\text{Winant}}. \tag{2.23}$$

It is important to realize that the solution N_{Winant} given in Eq. (2.23) is not an exact solution of system (2.12) as $\mathcal{O}(\alpha^2)$ and higher order terms are ignored. Therefore, in this paper, we refer to this model as the *3D asymptotic model*.

Parameter	Value
L	50 km
B	100 m
H	10 m
H_o^y	2 m
f	$\Omega^*/2$
A_v	10^{-3} m^2 s^{-1}

Table 2.1: Default parameter values used for the comparison of the 3D asymptotic model and 3D semi-idealized model. A no slip condition ($s \to \infty$) is imposed at the bottom.

2.5.2. VALIDATION

In this section, the 3D asymptotic and 3D semi-idealized model results for the surface elevation (section 2.5.2) and the velocity (section 2.5.2) are compared. An elongated rectangular basin of length $L = 50$ km and total width $2B = 200$ m such that α (= 0.002) $\ll$ 1, is considered. The default parameter values from table 2.1 are used.

SURFACE ELEVATION

First the surface elevations for different values of the eddy viscosities are compared, $A_v=10^{-3}$, 10^{-2} and 10^{-1} m^2 s^{-1}. The rectangular basin is discretized using right-angled triangles with 24 nodes in the along-channel direction and 20 nodes in the cross-channel direction. Figure 2.10 shows that the amplitudes of the width-averaged surface elevations obtained from the 3D asymptotic model and 3D semi-idealized model appear to agree well.

Note that for the parameter settings considered here, the Coriolis effects only influence the amplitude of the surface elevation marginally. This is because the width of the channel $2B = 200$ m is much smaller than the Rossby radius of deformation $R^* = \sqrt{gH}/f \approx 71$ km, which is the length scale of the cross-channel variations for the surface elevation.

FLOW FIELD

The rectangular domain is discretized using right-angled triangles with 200 nodes each in both the along-channel and cross-channel directions. This relatively large number of nodes is used to avoid numerical inaccuracies in the computation of the velocity components. Quadratic basis functions together with the mixed-method are used to compute the surface elevation and its first-order and second-order partial derivatives. Three velocity components are compared in the cross-channel direction at a distance $x = 25$ km from the entrance. It is evident from Fig. 2.11 that our 3D semi-idealized model is able to reproduce all three velocity profiles of the 3D asymptotic model, even small details in the vertical velocity W have been reproduced accurately. It is important to mention that the comparison of the velocity field at other locations is as good as at $x = 25$ km.
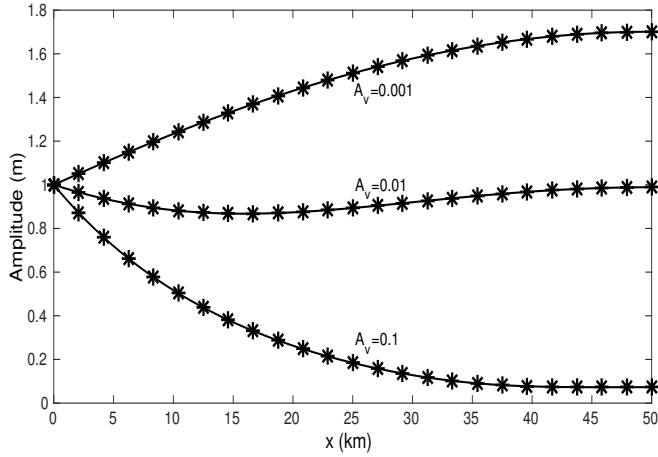
Figure 2.10: Width averaged amplitude of the surface elevation for $f = \Omega^*/2$ and different values of the eddy viscosity. The black solid line (–) depicts the 3D asymptotic model solution and black asterisk (*) depict the 3D semi-idealized model solution.
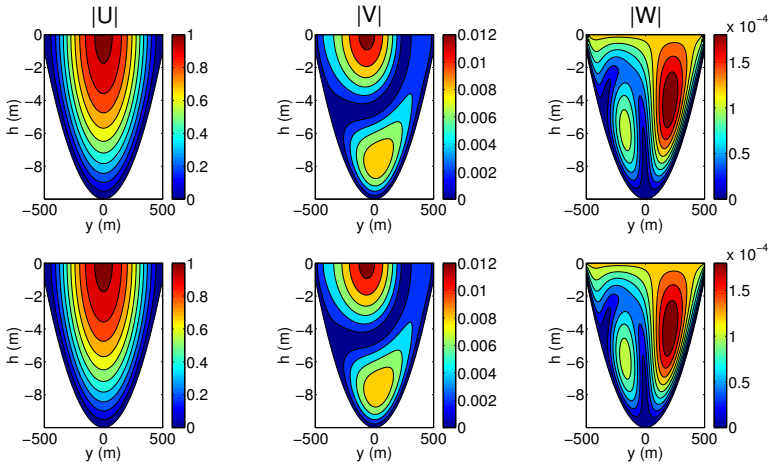
Figure 2.11: Comparison of the amplitude of three flow components (in m s^{-1}). The velocities have been plotted in the cross-section at a distance 25 km from the entrance. The upper panel shows the velocities from the 3D asymptotic model and the lower panel from the 3D semi-idealized model. Left, central and right panels show the along-channel, cross-channel and vertical velocities, respectively.

2.5.3. PARAMETER SENSITIVITY

In section 2.5.2, the results for the surface elevation and three flow components from 3D asymptotic and 3D semi-idealized models were compared for a rectangular channel whose horizontal aspect ratio α was small (2.0×10^{-3}). In this section, α will be systematically increased and the difference between the two models will be discussed. From

equations (2.22) and (2.23), it follows that

$$|N - N_{\text{Winant}}| = \mathscr{O}(\alpha^2).$$

Assuming that the solution of the 3D semi-idealized model $N_{\bar{h}}$ converges to the exact solution N, it follows that

$$|N_{\bar{h}} - N_{\text{Winant}}| \approx \mathscr{O}(\alpha^2), \tag{2.24}$$

which implies that for a channel geometry with horizontal aspect ratio α, an error of $\mathscr{O}(\alpha^2)$ is expected provided the 3D semi-idealized solution has been calculated with high enough accuracy.

To verify Eq. (2.24), a rectangular channel of length $L = 50$ km with different widths at the entrance is considered, $B = [250, 500, 1000, 2000, 4000, 8000, 16000]$, all in meters. For each value of B, the rectangular domain is discretized by refining a coarse grid with approximately 10^2 nodes to the finest grid with approximately 10^6 nodes. Linear basis functions are used to compute the finite element approximation of the surface elevation. For each value of B (hence α), the relative error of the surface elevation between the 3D asymptotic and 3D semi-idealized models is computed for different numbers of nodes.
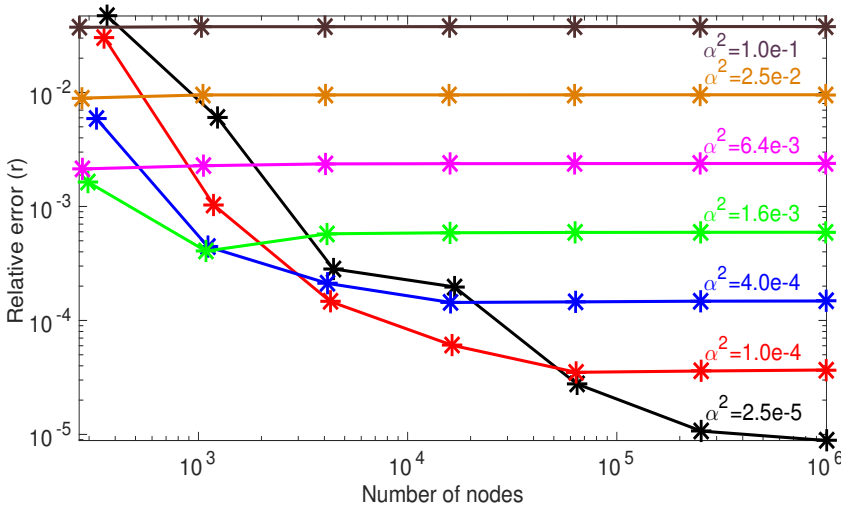
Figure 2.12: Relative error for the surface elevation as a function of the number of nodes for different values of the horizontal aspect ratio α plotted on log-log scale.

Figure 2.12 shows the influence of α on the accuracy of the 3D asymptotic model. For each α, the relative error becomes constant after a large enough number of nodes. This constant relative error is proportional to $\mathscr{O}(\alpha^2)$, thus suggesting that Eq. (2.24) is indeed correct. As α increases, the relative error between the 3D semi-idealized and 3D asymptotic models increases. For the largest number of nodal points used in the experiments, the relative error for different values of α appear to be equispaced. More

precisely, there is approximately a difference of a factor 4 between the error for each α, coinciding with the fact that the size of the domain is doubled each time. This clearly demonstrates the sensitivity of the 3D asymptotic model to the horizontal aspect ratio.

2.6. APPLICATION TO THE EMS ESTUARY

Our 3D semi-idealized model allows us to study the tidal motion in an estuary with arbitrary shape and bathymetry. As an example, we apply this model to the Ems estuary, situated on the border of the Netherlands and Germany (Fig. 2.13). In section 2.6.1, the surface elevation of the M_2 tide obtained with the 3D semi-idealized model will be calibrated for the Ems estuary. The results for the amplitude and the phase of the surface elevation are compared with the results of a complex numerical model (Delft3D) setup by Van Maren *et al.* [10]. Next, the influence of the local width convergence on the tidal motion will be investigated in section 2.6.2.
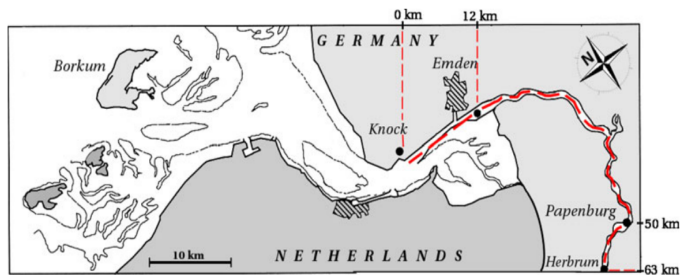
Figure 2.13: Map of the Ems estuary (from Chernetsky *et al.* [1])

2.6.1. CALIBRATION

The observational data for the water level in the Ems estuary for the year 2005 are used from six locations in the estuary, namely Emden, Pogum, Terborg, Leerort, Weener, and Papenburg (shown in magenta color in Fig. 2.14). The objective is to find the parameter values for the 3D semi-idealized model such that the model results fit the observations for the water level at these locations best. To this end, the geometric and bathymetric profiles of the year 2005 of the Ems estuary is used in the 3D semi-idealized model (Fig. 2.14). The Coriolis parameter f is assumed to be constant throughout the estuary i.e., $f = 1.166 \times 10^{-4}$ rad s^{-1} (latitude = 53.32 degree). The physical parameters such as the eddy viscosity A_v and the stress parameter s are also assumed to be constant in space. The 3D semi-idealized model is forced with a semi-diurnal (M_2) tide of constant amplitude at the seaward side (North sea side, see Fig. 2.14). The domain is discretized with approximately 200,000 nodes using an unstructured grid. The amplitude and the phase of the surface elevation obtained with the 3D semi-idealized model is then scaled in such a way that they match the observations at Emden. Next, the optimal values of A_v and s are found such that the mean squared error between the model results and the
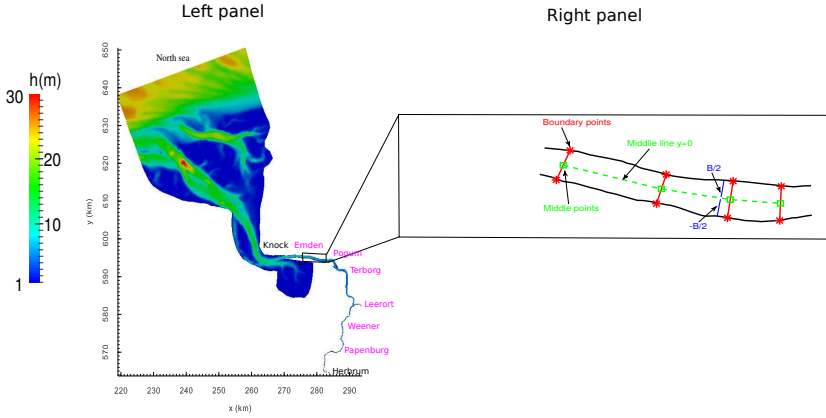
Figure 2.14: The geometry and bathymetry of the Ems estuary for the year 2005 (*left panel*). The data for the surface elevation of the M_2 tide is available at six locations (shown in the magenta color). The *right panel* describes how the realistic domain is transformed into a symmetric domain. Red asterisks ($*$) show the boundary points of the transects. The green dashed line (■ ■ ■ ■ ■) passes through the mid points of these transects shown by green squares (□). The width B of each transect is divided into $-B/2$ and $B/2$ with respect to the middle green line as shown by blue lines (———).

observations is minimum, i.e.,

$$\min_{A_v, s} \left\{ \frac{1}{2} \sum_i \left\{ (N_{o,i} - N_{m,i})^2 + 2N_{o,i} N_{m,i} \right. \right.$$

$$\left. \left. [1 - \cos(\phi_{o,i} - \phi_{m,i})] \right\} \right\},$$

where $N_{o,i}$ and $\phi_{o,i}$ are the amplitude and the phase of the surface elevation observed at location i, whereas $N_{m,i}$ and $\phi_{m,i}$ are the amplitude and the phase of the surface elevation obtained with the 3D semi-idealized model. The optimal values of A_v and s are 0.0036 m^2 s^{-1} and 0.0588 m s^{-1}, respectively.

Van Maren *et al.* [10] set up a Delft3D model to understand the role of deepening of the channel on the sediment concentration in the Ems estuary. The authors calibrated their model using the same data as used in this paper. Figure 2.15 shows the observations, results from the 3D semi-idealized model and results from the Delft3D model of van Maren. It is evident from Fig. 2.15 that the 3D semi-idealized model is able to reproduce the amplitude and the phase of the surface elevation at six different locations fairly well. It is interesting to see that for the amplitude of the surface elevation, the 3D semi-idealized model fits the observations at least as accurately as the Delft3D model at all locations except Pogum. For the phase of the surface elevation, both the 3D semi-idealized and the Delft3D models fit the observations equally well.

2.6.2. INFLUENCE OF LOCAL CONVERGENCE

We focus on the upper part of the Ems estuary, starting from Knock up to the weir at Herbrum. This part of the estuary consists of a narrow, meandering channel with decreasing

2
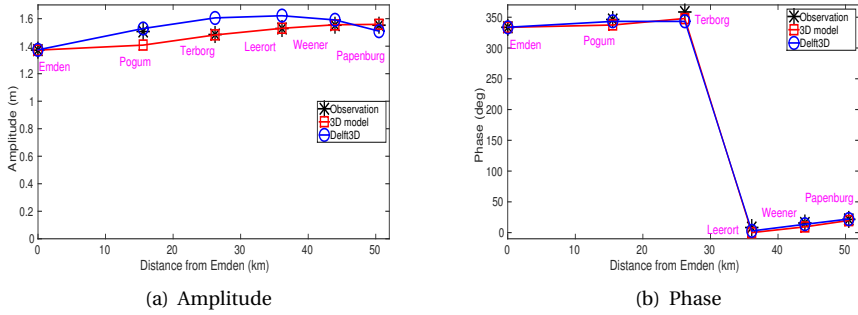
(a) Amplitude   (b) Phase

Figure 2.15: Amplitude (*left panel*) and phase (*right panel*) of the surface elevation from observations, 3D semi-idealized model and Delft3D model. The observations are shown in black asterisks (∗), results from 3D semi-idealized model in red squares (□) and results from Delft3D model in blue circles (○).

width towards the landward side. In this section, the effects of channel convergence and meandering are investigated.

To study the influence of the local convergence on the water motion, the channel from Knock to Herbrum is transformed into a symmetric domain bounded by $y = -B(x)/2$ at the lower boundary to $y = B(x)/2$ at the upper boundary. For this, the widths B along many transects in the channel (red asterisks, Fig. 2.14, right panel) are mapped to a new domain bounded by $y = -B/2$ to $y = B/2$ (blue lines, Fig. 2.14, right panel), with the central line $y = 0$ passing through the middle of the channel (green dashed line, Fig. 2.14, right panel). The resulting data set is shown in Fig. 2.16 (red asterisks). We call this domain the scattered domain. It is important to note that the scattered domain is similar to the realistic domain except that the meandering effects in the scattered domain have been ignored.

First, this data set is fit with an exponential function given by

$$B = B_0 \exp(-x/L_b),$$

where B_0 is the total width at the entrance and L_b is the e-folding length.

The optimal values of B_0 and L_b fitting the data are calculated using the least square method and are given as $B_0 = 543.9$ m, $L_b = 24.5$ km. The corresponding domain is shown in Fig. 2.16. It is also possible to fit the data with a polynomial function. From Fig. 2.16, it is evident that a 9th degree polynomial function fits the width data more accurately than the exponential function.

The values of the eddy viscosity A_v and the stress parameter s, found during the calibration process in the previous section, are used. To understand the influence of geometrical effects in isolation, a uniform bed profile is considered. Water depth of 15 m is chosen such that the amplitude of the surface elevation exhibits a similar trend as shown in Fig. 2.15(a). The system is forced with a semi-diurnal (M_2) tide with an amplitude of 1.42 m at Knock. The domain is discretized using an unstructured grid with approximately 200,000 nodes. Linear basis functions together with the ZZ-method are used to compute the surface elevation and the horizontal velocities.
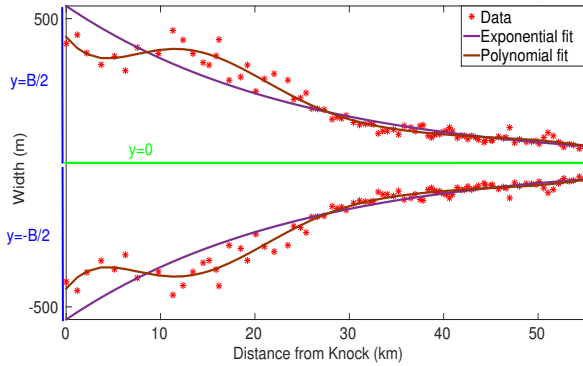
Figure 2.16: Approximation of the geometry of the Ems estuary. See Fig. 2.14 (right panel) for meaning of various colors.

Figure 2.17(a) shows the amplitude of the surface elevation along the middle line (shown in green color in Figs. 2.16 and 2.14) for different schematizations of the domain. It is evident that with the exponential domain, the amplitude of the surface elevation throughout the domain is underestimated. Using the polynomial function of 9th degree to approximate the width compares well in the first 30 km, further upstream, the amplitude is slightly underestimated. The results with the scattered domain shows the same behavior. This deviation between the realistic and scattered domains is probably due to the meandering effects. Similar behavior is observed for the phase of the surface elevation.

(a) Surface elevation

(b) Horizontal velocity
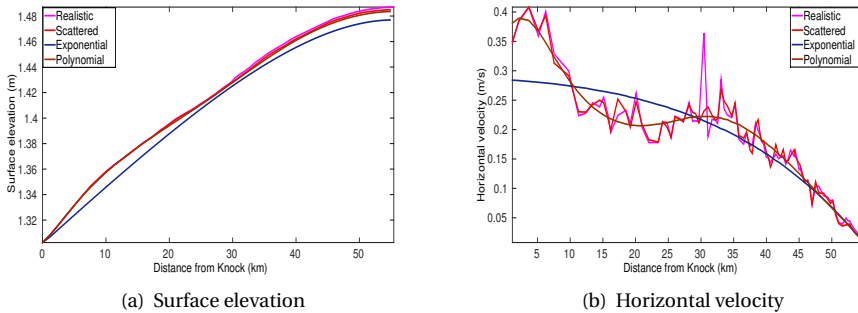
Figure 2.17: *Left panel* shows the amplitude of the surface elevation and *right panel* the depth-averaged horizontal velocity along the middle of the channel for different types of channel domains.

Next we look at the amplitude of the depth-averaged horizontal velocity which is defined as $\sqrt{|\bar{U}|^2 + |\bar{V}|^2}$, where $\bar{U}$ and $\bar{V}$ are the depth-averaged along-channel and cross-channel velocities, respectively and $|\cdot|$ denotes the absolute value. Figure 2.17(b) shows that the results for the depth-averaged horizontal velocity with exponential domain de-

2
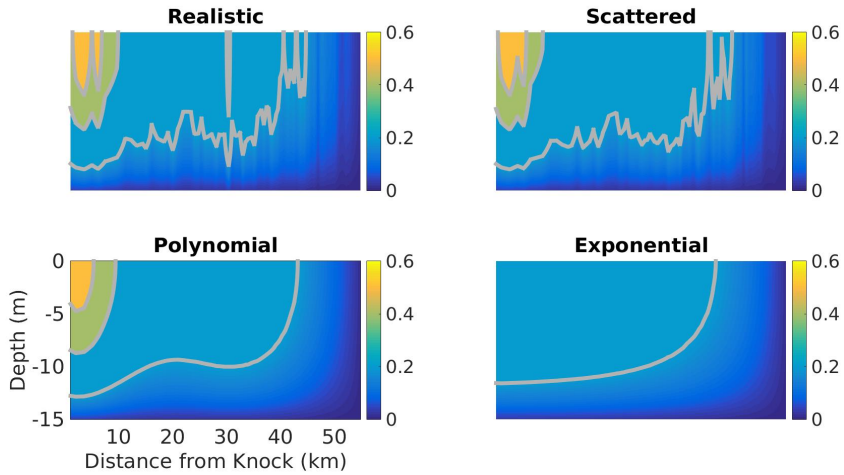
Figure 2.18: Absolute value of the horizontal velocity along the middle of the channel for different types of channel domains. The axes are same in all the plots. The units in the colorbars are m s^{-1}.

viates significantly from the results with the realistic domain. The domain constructed with a 9th degree polynomial captures the overall behavior of the depth-averaged horizontal velocity profile throughout the domain. It is interesting to see the agreement between the results obtained with the scattered domain and the realistic domain. The scattered domain is able to accurately reproduce the depth-averaged horizontal velocity at the entrance and the end of the channel.

To understand the influence of different channel domains on the vertical structure of the flow, the absolute value of the horizontal velocity, which is defined as $\sqrt{|U|^2 + |V|^2}$, where U and V are the along-channel and cross-channel velocities, respectively, is plotted along the middle of the channel. Figure 2.18 shows that the scattered and polynomial domains are able to reproduce the overall behavior of the horizontal velocity of the realistic domain. It is interesting to see that smoothing the scattered domain with a polynomial function also smoothes the contour lines of the velocity in the vertical direction, capturing the main features. The exponential domain on the other hand, clearly seems to miss the information throughout the domain, especially at the entrance. This is also observed in Fig. 2.17(b).

2.7. CONCLUSIONS

A three-dimensional semi-idealized model for the tidal motion in an estuary with arbitrary geometric and bathymetric profiles has been developed. This model is intended to bridge the gap between idealized and complex simulation models by retaining the advantages of the idealized models (developed to obtain insight in physical mechanisms, well suited to perform quick sensitivity analysis), but removing one of its weak points (namely the requirement of idealized geometry and bathymetry). In this model, the three-dimensional velocity field is expressed in terms of the first and second-order

partial derivatives of the surface elevation. The surface elevation itself follows from a two-dimensional linear elliptic partial differential equation which is solved numerically using the finite element method. Linear and quadratic polynomials are considered as basis functions for the finite element approximation of the surface elevation. Concerning the accuracy and convergence properties of the newly developed model, we found a second order convergence with linear basis functions and a third order convergence with quadratic basis functions. With linear basis functions, ZZ-method proposed by Zienkiewicz and Zhu [22] gives the most accurate results for the first-order partial derivatives of the surface elevation. With quadratic basis functions, direct differentiation (DD-method) of the finite element approximation of the surface elevation is recommended for the first-order partial derivatives. For the second-order partial derivatives, a new method known as the mixed-method, which is a combination of DD-method and ZZ-method, is shown to work the best.

To investigate the influence of geometry and bathymetry on the tidal characteristics, the results obtained with the three-dimensional semi-idealized model are compared to those obtained with a width-averaged model developed by Chernetsky *et al.* [1]. For an exponentially converging estuary with a flat bed, the deviation for the surface elevation between the width-averaged model and the three-dimensional semi-idealized model increases with increasing width at the entrance. For an estuary with constant width and parabolic bed profile in the lateral direction, the width-averaged model underestimates the amplitude of the surface elevation for all values of the lateral water depths. The comparison between the three-dimensional semi-idealized model and the three-dimensional asymptotic model developed by Winant [16] for an elongated rectangular channel shows that the absolute difference in the surface elevation obtained with these two models increases for increasing horizontal aspect ratio, and is proportional to the square of the horizontal aspect ratio.

To assess the influence of a more complex geometry on tidal propagation, the Ems estuary is considered. First, the three-dimensional semi-idealized model is calibrated using the observed geometry and bathymetry of the Ems estuary for the year 2005. Concerning the amplitude and the phase of the surface elevation of the M_2 tide, a good agreement is found between the observations, the model results of three-dimensional semi-idealized model and the model results of a complex numerical model (Delft3D) setup by Van Maren *et al.* [10]. The model suggests that approximating the geometry of the Ems estuary with an exponential function gives unsatisfactory results for the surface elevation and the horizontal velocity compared to the results with the realistic geometric profile. When approximated with a function that captures the local convergence effects (in this case, a 9th degree polynomial) of the Ems estuary, a good agreement with the results obtained with realistic geometry was found. It is therefore recommended to consider local geometrical effects when using simplified geometry to model tidal motion.

REFERENCES

[1] A. S. Chernetsky, H. M. Schuttelaars, and S. A. Talke, *The effect of tidal asymmetry and temporal settling lag on sediment trapping in tidal estuaries,* Ocean Dynamics **60**, 1219 (2010).

[2] V. N. De Jonge, R. Pinto, and R. K. Turner, *Integrating ecological, economic and social aspects to generate useful management information under the EU Directives 'ecosystem approach',* Ocean and Coastal Management **68**, 169 (2012).

[3] J. C. Winterwerp, Z. B. Wang, A. Braeckel, G. Holland, and F. Kösters, *Man-induced regime shifts in small estuaries II: a comparison of rivers,* Ocean Dynamics **63**, 1293 (2013).

[4] J. C. Winterwerp and Z. B. Wang, *Man-induced regime shifts in small estuaries I: theory,* Ocean Dynamics **63**, 1279 (2013).

[5] A. B. Murray, *Contrasting the goals, strategies, and predictions associated with simplified numerical models and detailed simulations,* Prediction in geomorphology , 1 (2003).

[6] H. J. De Vriend, *Mathematical modelling and large-scale coastal behaviour. Part 2 - Predictive models,* Journal of Hydraulic Research **29**, 741 (1992).

[7] H. J. De Vriend, *Mathematical modelling and large-scale coastal behaviour. Part 1 - Physical processes,* Journal of Hydraulic Research **29**, 727 (1991).

[8] J. Van de Kreeke and K. Robaczewska, *Tide-induced residual transport of coarse sediment: Application to the Ems estuary,* Netherlands Journal of Sea Research **31**, 209 (1993).

[9] J. U. Pein, E. V. Stanev, and Y. J. Zhang, *The tidal asymmetries and residual flows in Ems Estuary,* Ocean Dynamics (2014).

[10] D. S. Van Maren, J. C. Winterwerp, and J. Vroom, *Fine sediment transport into the hyper-turbid lower Ems River: the role of channel deepening and sediment-induced drag reduction,* Ocean Dynamics **65**, 589 (2015).

[11] S. Lanzoni and G. Seminara, *On tide propagation in convergent estuaries,* Journal of Geophysical Research **103**, 793 (1998).

[12] A. Valle-Levinson, ed., *Contemporary issues in estuarine physics* (Cambridge University Press, 2010).

[13] J. P. Ianniello, *Tidally induced residual currents in estuaries of constant breadth and depth,* Journal of Marine Research **35**, 755 (1977).

[14] K. M. H. Huijts, H. M. Schuttelaars, H. De Swart, and C. T. Friedrichs, *Analytical study of the transverse distribution of along-channel and transverse residual flows in tidal estuaries,* Continental Shelf Research **29**, 89 (2009).

[15] C. Li and A. Valle-Levinson, *A two-dimensional analytic tidal model for a narrow estuary of arbitrary lateral depth variation: The intratidal motion,* Journal of Geophysical Research **104**, 23,525 (1999).

[16] C. D. Winant, *Three-Dimensional Tidal Flow in an Elongated, Rotating Basin,* Journal of Physical Oceanography **37**, 2345 (2007).

[17] G. P. Schramkowski, H. M. Schuttelaars, and H. E. De Swart, *The effect of geometry and bottom friction on local bed forms in a tidal embayment,* Continental Shelf Research **22**, 1821 (2002).

[18] J. T. F. Zimmerman, *On the Lorentz linearization of a nonlinearly damped tidal Helmholtz oscillator,* Proceedings of the Koninklijke Nederlandse Akademi **95**, 127 (1992).

[19] M. S. Gockenbach, *Understanding and Implementing the Finite Element Method* (Society of Industrial and Applied Mathematics (SIAM), Philadelphia, 2006).

[20] J. R. Shewchuk, *Triangle: Engineering a 2D Quality Mesh Generator and Delaunay Triangulator,* in *Applied Computational Geometry: Towards Geometric Engineering,* Lecture Notes in Computer Science, Vol. 1148, edited by M. C. Lin and D. Manocha (Springer-Verlag, 1996) pp. 203–222, from the First ACM Workshop on Applied Computational Geometry.

[21] G. F. Carey, *Derivative calculation from finite element solutions,* Computer Methods in Applied Mechanics and Engineering **35**, 1 (1982).

[22] O. C. Zienkiewicz and J. Z. Zhu, *The superconvergent patch recovery and a posteriori error estimates . Part 1 : The recovery technique,* International Journal for Numerical Methods in Engineering **33**, 1331 (1992).

[23] O. C. Zienkiewicz and J. Z. Zhu, *The superconvergent patch recovery and a posteriori error estimates. Part 2: Error estimates and adaptivity,* International Journal for Numerical Methods in Engineering **33**, 1365 (1992).

[24] F. Ilinca and D. Pelletier, *Computation of accurate nodal derivatives of finite element solutions : The finite node displacement method,* International Journal for Numerical Methods in Engineering **71**, 1181 (2007).

2

3

THREE-DIMENSIONAL SEMI-IDEALIZED MODEL FOR ESTUARINE TURBIDITY MAXIMA IN TIDALLY DOMINATED ESTUARIES

We develop a three-dimensional idealized model that is specifically aimed at gaining insight in the physical mechanisms resulting in the formation of estuarine turbidity maxima in tidally dominated estuaries. First, the three-dimensional equations for water motion and suspended sediment concentration together with the so-called morphodynamic equilibrium condition, are scaled. Next, surface elevation, velocity and sediment concentration are expanded in a small parameter $\epsilon = \bar{A}_{M_2}/H$, where $\bar{A}_{M_2}$ is the mean amplitude of the M_2 tide and H is the mean water depth at the seaward side. This results in a system of equations at each order in this small parameter. This ordering allows solving for the vertical structure of the velocity and suspended sediment concentration, independently of the horizontal dimension. After obtaining these vertical structures, the horizontal dependencies of the physical variables follow from solving a two-dimensional elliptic partial differential equation for the surface elevation. The availability of fine sediments in the estuary follows from a two-dimensional elliptic partial differential equation which results from requiring the system to be in morphodynamic equilibrium, and prescribing the total amount of easily erodible sediments available in the estuary. These elliptic equations for the surface elevation and sediment availability are solved numerically using the finite element method with cubic polynomials as basis functions. As a first application, the model is applied to the Ems estuary using a simplified geometry and bathymetric profiles characteristic for the years 1980 and 2005. The availability of fine sediments and location of maximum concentration are investigated for different lateral depth profiles. In the first experiment, a uniform lateral depth is considered. In this case, both the sediment availability and suspended sediment concentration are, as expected, uniform in the lat-

eral direction. In 1980, the sediment is mainly trapped near the entrance, while in 2005, the sediment is mostly trapped in the freshwater zone. In the next experiment, the lateral bathymetry is varied parabolically while keeping the mean depth unchanged. In this case, the fine sediment is mainly found at the shallow sides, but the maximum sediment concentration is found in the deeper channel where the bed shear stress is much larger than on the shoals. As a final experiment, a more realistic (but smoothed) geometry and bathymetry for the Ems estuary are considered, showing the possibilities of applying the newly developed model to complex geometries and bathymetries.

In most estuaries, regions are observed with elevated suspended sediment concentration compared with the adjacent landward and seaward regions. These regions are called *estuarine turbidity maxima* (ETM). A good understanding of the ETM dynamics is important for many reasons (for a detailed discussion, see Jay *et al.* [1] and Burchard *et al.* [2]). First, the presence of an ETM can have a strong influence on the ecological functioning of an estuary, as it can result in limited light conditions or anoxia (Talke *et al.* [3]). Furthermore, at the location of the ETM, there is often a considerable deposition of fine sediments, which results in enhanced dredging efforts to keep the estuary accessible and the navigation lanes at their regular depths. Finally, ETM dynamics is shown to be sensitive to changes in bathymetry, geometry and external forcing conditions (De Jonge *et al.* [4]), which (if not well understood) can result in a deterioration of the system as a whole.

To better understand and assess the effects of natural or anthropogenic changes on ETM dynamics, different types of models are being applied (Murray [5]). For example, state-of-the-art three dimensional process-based models are applied to simulate ETM dynamics (Weilbeer [6], Van Maren *et al.* [7]) and changes in ETM dynamics due to human interventions. However, these models are computationally expensive and the mechanisms resulting in the observed dynamics are difficult to analyze (Schuttelaars *et al.* [8]).

Alternatively, process-based idealized models are specifically designed to and aimed towards studying the mechanisms resulting in the formation of ETMs and assessing their sensitivity to parameters. Since these models focus on a specific phenomenon, some processes are not or only parametrically taken into account. Furthermore, geometry and bathymetry are often simplified. Huijts *et al.* [9] used an idealized modeling approach to study the trapping of fine sediments in the lateral direction. Talke *et al.* [10] and Chernetsky *et al.* [11] focused on the sediment transport in the longitudinal direction, using a width-averaged model. However, Geyer *et al.* [12] and Kim and Voulgaris [13] pointed out that the lateral water motion and suspended sediment dynamics affect the processes in the longitudinal direction and vice-versa. Therefore, to understand the ETM dynamics and the underlying dominant trapping mechanisms (see for example Jay *et al.* [1] for an overview of possible mechanisms), it is necessary to study both the lateral and longitudinal processes simultaneously. Clearly, this requires a three-dimensional modelling approach.

For the water motion, three-dimensional idealized models have been developed and analyzed in detail (Winant [14], Winant [15], Ensing *et al.* [16] and Kumar *et al.* [17]), but for the sediment transport and trapping of fine sediments, three-dimensional idealized models are still missing. Therefore, the aim of this paper is to develop a three-dimensional idealized model for water motion and sediment dynamics in an estuary of arbitrary shape and bathymetry, including the Coriolis effect. This allows for a systematic study of the sediment trapping mechanisms in tidally-dominated estuaries. The physical parameters are allowed to vary in the horizontal plane. The three-dimensional model is solved using an asymptotic expansion technique. This results in analytical solutions of the vertical profiles of the velocity and suspended sediment concentration. These solutions still depend on the (gradients of the) surface elevation. The surface elevation itself follows from a two-dimensional elliptic partial differential equation which is solved numerically using the finite element method. The condition of morphodynamic equilibrium is prescribed to govern the availability of fine sediments in the estuary.

As a first example, the new model is applied to the Ems estuary using simplified geometric and bathymetric profiles characteristic for 1980 and 2005. The location of maximum trapping of sediments for both years is investigated. The influence of lateral bathymetry is investigated by first keeping the depth in the lateral direction uniform. Next, the lateral bathymetric profile is varied parabolically while keeping the width-averaged depth unchanged. The results are qualitatively compared with observations and the influence of lateral depth variations is discussed. As a final example, we use the (smoothed) observed bathymetry and geometry of the Ems in 2005 to obtain the trapping location of the fine sediments.

The structure of the paper is as follows. The philosophy of idealized modeling and step by step overview of model development are presented in section 3.1. The model equations of water motion and suspended sediment concentration and the condition of morphodynamic equilibrium are presented in section 3.2. This section also presents the scaling and perturbation analyses which results in a system of equations at each order for the water motion and the suspended sediment concentration. The leading-order system for the water motion is solved in section 3.3, the first-order system in section 3.4. Similarly, the leading-order and first-order systems for suspended sediment concentrations are solved in sections 3.5 and 3.6, respectively. The equation for sediment availability governing the distribution of fine sediments in the estuary is solved in section 3.7. Section 3.8 gives a short description of the numerical solution procedure for the two-dimensional elliptic partial differential equations obtained for both the surface elevation and sediment availability with a special discussion on the accuracy of the resulting solutions. Next, this model is applied to the Ems estuary in section 3.9. Finally, conclusions are presented in section 3.10.

3.1. IDEALIZED MODEL - MODEL PHILOSOPHY

The main research question will be answered by developing a so-called *idealized, process-based model*. Idealized models focus on specific phenomena (here ETM formation), neglecting or simplifying processes that are not essential for the phenomenon under study. In this chapter, we focus on developing such a model for a tidally dominated, well-mixed estuary. It is assumed that the suspended sediment concentrations do not

influence the water motion significantly, and that the water motion is mainly driven by a prescribed M_2 tide at the seaward side.

In constructing this idealized model, ten steps can be identified. These steps are visualized in Fig. (3.1); the precise sections where the individual steps are discussed in detail, are indicated in this figure as well. Below, the main steps are summarized:

1. Derive the model equations, and define the geometry and bathymetry of interest.

2. Make the physical variables (such as surface elevation, water depth, etc.) dimensionless by introducing typical scales; subsequently use these to make the governing equations dimensionless. Since all dimensionless physical variables are order one, the relative importance of each term in any of the equations is measured by the magnitude of the dimensionless number, multiplying the dimensionless group of physical variables. These magnitudes can be calculated explicitly after choosing scales that are representative for the estuary/class of estuaries under consideration.

3. Verify that one of the dimensionless numbers is the ratio of the M_2 surface elevation averaged over the entrance (A_{M_2}) and the mean water depth H at the seaward boundary. This ratio, denoted by ϵ, is much smaller than one. Next, all other dimensionless numbers are related to ϵ.

4. Expand the physical variables in the small parameter ϵ. These asymptotic expansions are introduced in the dimensionless equations, and terms of equal order in ϵ are collected. Since only terms of equal order in ϵ can balance, this results in a system of equations at each order in ϵ.

5. Construct the solutions for the leading-order water motion, i.e., at order ϵ^0. Since the leading-order water motion is only driven by the M_2 tidal signal at the seaward boundary, it only consists of an M_2 constituent.

6. Derive the first-order water motion using the leading-order water motion, i.e., ϵ^1. It is found that the temporal variations of the first order water motion consist of a residual and an M_4 contribution.

7. Calculate the leading-order concentration using the leading-order water motion. Concerning its temporal behaviour, a residual contribution and contributions with multiples of the M_4 tidal frequency are obtained.

8. The first-order suspended sediment concentration is obtained using information of both the leading- and first-order velocity fields, and the leading-order concentration. The temporal variations of the first-order concentration consist of a residual contribution and contributions with multiples of the M_2 tidal frequency.

9. Calculate the leading-order, tidally averaged suspended sediment transport. It consists of three contributions:
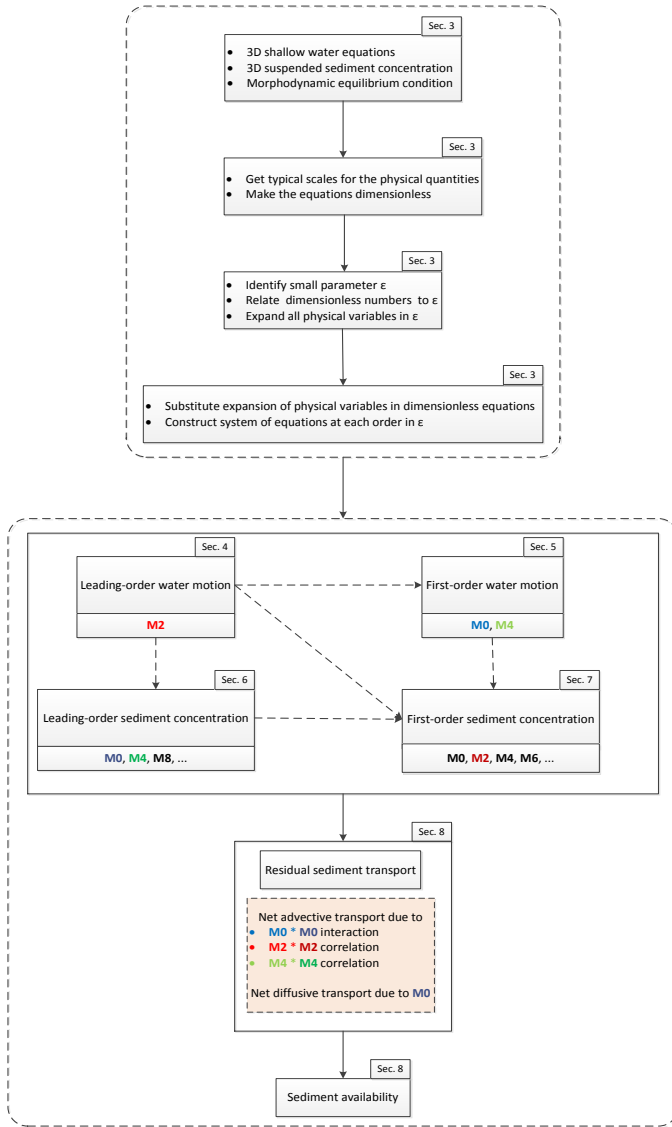
Figure 3.1: Flow chart showing the steps involved in the development of the idealized model.

- advective transport due to correlations between the leading-order velocity and first-order concentration. Only the correlation between the leading-order velocity and the M_2 component of the first-order concentration results

in a net transport.

- advective transport due to correlations between the first-order velocity and leading-order concentration. Both the residual concentration, advected by the residual velocity, and the correlation between the first-order M_4 velocity and the M_4 component of the leading-order concentration result in a net transport.

- diffusive transport due to spatial gradients in the residual concentration field.

10. Impose the condition of morphodynamic equilibrium to obtain the spatial distribution of easily erodible sediments.

In the following sections (see Fig. 3.1), these steps will be executed to develop a model for sediment trapping in a tidally-dominated estuary.

3.2. MODEL FORMULATION

3.2.1. MODEL DOMAIN

An estuary of arbitrary shape (geometry) and depth profile (bathymetry) is considered (Fig. 3.2). A Cartesian coordinate system is used, with x, y denoting the horizontal coordinates, and z the vertical coordinate, pointing in the upward direction. Importantly, x or y need not represent the along-channel or cross-channel coordinate. The undisturbed water level is denoted by $z = 0$ and the surface elevation by $z = \eta(x, y, t)$, where t is time. The undisturbed bed level denoted by $z = -h(x, y)$, is assumed to be prescribed and independent of time on the time scale under consideration. Boundaries where the surface elevation is prescribed are called seaward boundaries (denoted by $\partial_S \Omega$), if river discharge is prescribed, they are called river boundaries (denoted by $\partial_R \Omega$). The closed boundaries are denoted by $\partial_C \Omega$.

3.2.2. WATER MOTION

The water motion is governed by the three-dimensional shallow water equations, including the Coriolis effect. Conservation of mass and momentum (using the Boussinesq approximation and hydrostatic balance) is expressed as (Cushman-Roisin and Beckers [18] and Vreugdenhil [19])

$$\frac{\partial u}{\partial x} + \frac{\partial v}{\partial y} + \frac{\partial w}{\partial z} = 0, \tag{3.1a}$$

$$\frac{\partial u}{\partial t} + u\frac{\partial u}{\partial x} + v\frac{\partial u}{\partial y} + w\frac{\partial u}{\partial z} - fv = -g\frac{\partial \eta}{\partial x} - \frac{g}{\rho_0}\int_z^\eta \frac{\partial \rho}{\partial x}dz' + \frac{\partial}{\partial z}(A_v\frac{\partial u}{\partial z}), \tag{3.1b}$$

$$\frac{\partial v}{\partial t} + u\frac{\partial v}{\partial x} + v\frac{\partial v}{\partial y} + w\frac{\partial v}{\partial z} + fu = -g\frac{\partial \eta}{\partial y} - \frac{g}{\rho_0}\int_z^\eta \frac{\partial \rho}{\partial y}dz' + \frac{\partial}{\partial z}(A_v\frac{\partial v}{\partial z}). \tag{3.1c}$$

The unknown variable $\boldsymbol{u} = (u, v, w)$ denotes the components of the velocity field in x, y and z directions, respectively. The mean density is denoted by ρ_0 and the dynamic density by $\rho(x, y)$ which is assumed to be a prescribed function of the horizontal coordinates x and y only, i.e., the estuary is assumed to be well-mixed. Furthermore, time variations
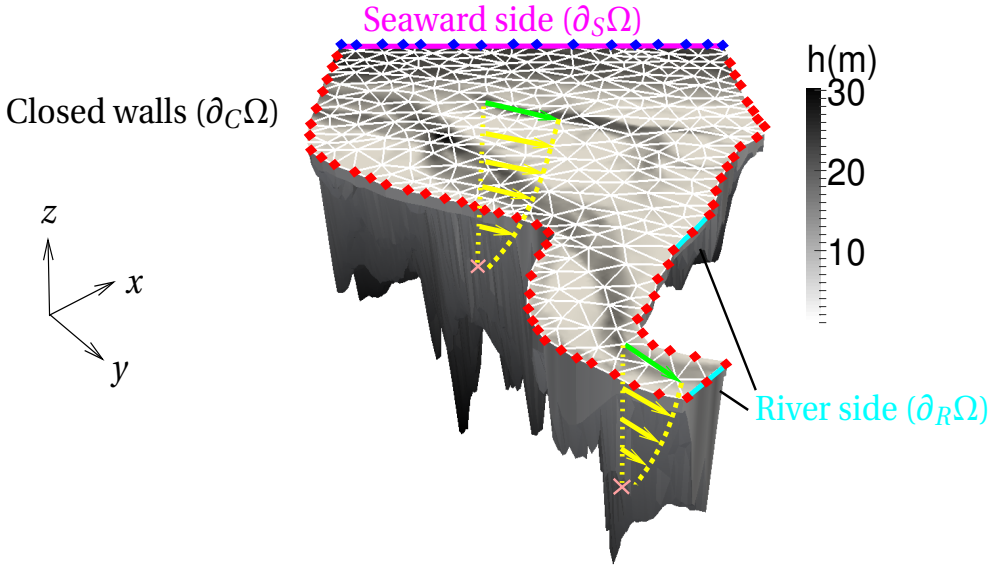
Figure 3.2: Three-dimensional sketch of an estuary with arbitrary geometric and bathymetric profiles. The bathymetric profile is shown on a grayscale. The seaward side (denoted by $\partial_S\Omega$) is shown in magenta color (━━━) and the river boundary (denoted by $\partial_R\Omega$) in cyan color (━━━). The other boundaries (denoted by $\partial_C\Omega$) are assumed to be closed walls. The surface of the estuary is discretized using linear triangles in order to compute the surface elevation with the finite element method. The nodes on the seaward boundary (where elevation amplitude is prescribed) are indicated by blue diamonds (◆) and on rest of the boundaries (nodes where the surface elevation has to be computed) by red diamonds (◆). At each node in the triangulization of the surface, the vertical profile of the velocity field can be computed analytically using partial derivatives of the surface elevation as shown by yellow dashed lines (▪ ▪ ▪ ▪ ▪). The velocity at the surface is depicted by green arrows (━▶) and, in the rest of the water column, by yellow arrows (━▶). This figure has been taken from Kumar *et al.* [17].

in ρ are neglected. The vertical eddy viscosity coefficient is denoted by $A_v(x, y)$ and is assumed to be a prescribed function of x and y only, thus uniform in z and time-invariant. Note that horizontal viscous effects are neglected in Eq. (3.1), see Winant [14] for a detailed discussion. The parameter f is the Coriolis parameter, given by $f = 2\tilde{\Omega}\sin\theta$, where $\tilde{\Omega} = 7.292 \times 10^{-5}$ rad s^{-1} is the angular frequency of the Earth's rotation, and θ the latitude which is assumed to be uniform over the domain (f-plane approximation).

To obtain a well-posed problem for the water motion, appropriate boundary conditions have to be prescribed. At the seaward boundary ($\partial_S\Omega$), the system is forced with a combination of a prescribed semi-diurnal lunar (M_2) tide and its first overtide (M_4),

$$\eta = A_{M_2}\cos(\omega t - \phi_{M_2}) + A_{M_4}(2\omega t - \phi_{M_4}), \quad \text{for all} \ (x, y) \text{ in } \partial_S\Omega, \tag{3.2a}$$

where $A_{M_2}(x, y)$ and $A_{M_4}(x, y)$ are the (possibly) spatially varying amplitudes of the surface elevation of the M_2 and M_4 tidal constituents at the seaward boundary. The phases of the M_2 and M_4 tides at the seaward side are denoted by $\phi_{M_2}(x, y)$ and $\phi_{M_4}(x, y)$, respectively. The M_2 tidal constituent is assumed to be the dominant one, i.e., $A_{M_4} < A_{M_2}$. The parameter $\omega = 2\pi/T$ denotes the angular frequency of the M_2 tide with period $T =$

12.42 hrs. At the river boundary ($\partial_R\Omega$), a time-independent river discharge Q ($\mathrm{m^3\,s^{-1}}$) is prescribed,

$$\int_{\partial_R\Omega}\left(\int_{-h}^{\eta}\boldsymbol{u}_{\mathrm{h}}\cdot\hat{\mathbf{n}}\,\mathrm{d}z\right)\mathrm{d}s=-Q,\tag{3.2b}$$

where $\boldsymbol{u}_{\mathrm{h}}=(u,v)$ denotes the horizontal velocity and $\hat{\mathbf{n}}$, the horizontal unit normal vector pointing outwards. The outer integral in Eq. (3.2b) denotes the line integral over the river boundary. Importantly, $-Q$ is the total inflow of fresh water over one river boundary. If there is more than one river inlet (shown in cyan color ———— in Fig. 3.2), appropriate river discharges Q are assigned to each one. Since we are focussing on tidally dominated systems, the river discharge is assumed to be small compared with the tidal discharge (see section 3.2.5). At the closed boundaries ($\partial_C\Omega$), a no-transport condition is imposed,

$$\int_{-h}^{\eta}\boldsymbol{u}_{\mathrm{h}}\cdot\hat{\mathbf{n}}\,\mathrm{d}z=0,\quad\text{for all}\;\;(x,y)\;\text{in}\;\partial_C\Omega.\tag{3.2c}$$

It is not possible to require the flux to vanish at each point in the vertical at the boundary. This is a consequence of neglecting the horizontal viscous effects, by which the horizontal viscous boundary layer is not resolved. Following Winant [14], this is acceptable since the thickness of this boundary layer is negligible compared with the horizontal length scale we are focusing on (length scale of the order of the length of the estuary).

At the free surface $z=\eta$, kinematic and dynamic boundary conditions are imposed,

$$w=\frac{\partial\eta}{\partial t}+u\frac{\partial\eta}{\partial x}+v\frac{\partial\eta}{\partial y},\;\;\text{at}\;\;z=\eta,\tag{3.2d}$$

$$A_{\mathrm{v}}\frac{\partial\boldsymbol{u}_{\mathrm{h}}}{\partial z}=\mathbf{0}_{\mathrm{h}},\qquad\qquad\text{at}\;\;z=\eta,\tag{3.2e}$$

where $\mathbf{0}_{\mathrm{h}}=(0,0)$ is the two-dimensional horizontal null vector. At the bottom $z=-h$, the non-permeability condition (kinematic) and the dynamic boundary condition are prescribed,

$$w=-u\frac{\partial h}{\partial x}-v\frac{\partial h}{\partial y},\;\;\text{at}\;\;z=-h,\tag{3.2f}$$

$$A_{\mathrm{v}}\frac{\partial\boldsymbol{u}_{\mathrm{h}}}{\partial z}=\frac{\boldsymbol{\tau}_b}{\rho_0}=s\boldsymbol{u}_{\mathrm{h}},\;\;\text{at}\;\;z=-h,\tag{3.2g}$$

where $s(x,y)$ is the so-called stress parameter which follows from the linearization of the bed shear stress (see Zimmerman [20]). If $s\to 0$, this formulation reduces to the free-slip condition, for $s\to\infty$ to the no-slip condition. It is important to point out that by adopting this simplification, the constant stress layer near the bed where the viscosity goes to zero, is neglected, see Schramkowski *et al.* [21] for details. Here, we have assumed that both the bottom slopes and the surface elevation slopes are much smaller than 1, i.e., $|\nabla h|,|\nabla\eta|\ll 1$.

3.2.3. SUSPENDED SEDIMENT CONCENTRATION

The suspended sediment concentration is modeled by a three-dimensional advection-diffusion equation

$$\frac{\partial c}{\partial t} + \nabla \cdot \mathbf{F} = 0, \tag{3.3}$$

with $\mathbf{F} = \mathbf{F}_a + \mathbf{F}_s + \mathbf{F}_d$, the sediment flux that consists of three different contributions: the advective flux $\mathbf{F}_a$, the settling flux $\mathbf{F}_s$ and the diffusive flux $\mathbf{F}_d$. These fluxes are given by

$$\mathbf{F}_a = c\boldsymbol{u},$$
$$\mathbf{F}_s = -(0, 0, c w_s),$$
$$\mathbf{F}_d = -(K_h \frac{\partial c}{\partial x}, K_h \frac{\partial c}{\partial y}, K_v \frac{\partial c}{\partial z}),$$

where w_s denotes the settling velocity, and $K_h(x, y)$ and $K_v(x, y)$ the horizontal and vertical diffusivities, respectively. The vertical diffusivity K_v is assumed to be equal to the vertical eddy viscosity A_v. Using these expressions, Eq. (3.3) becomes

$$\frac{\partial c}{\partial t} + \frac{\partial}{\partial x}\left(cu - K_h \frac{\partial c}{\partial x}\right) + \frac{\partial}{\partial y}\left(cv - K_h \frac{\partial c}{\partial y}\right) + \frac{\partial}{\partial z}\left(c(w - w_s) - K_v \frac{\partial c}{\partial z}\right) = 0. \tag{3.4}$$

At the free surface $z = \eta$ and the bottom $z = -h$, the outward normal component of the sum of the settling and diffusive fluxes is required to be equal to a specified erosion-deposition flux of volume concentration S_*, i.e.,

$$-(\mathbf{F}_s + \mathbf{F}_d) \cdot \hat{\mathbf{n}} = S_*, \tag{3.5}$$

where $\hat{\mathbf{n}}$ is the unit normal vector pointing outwards.

At the free surface, using $|\nabla \eta| \ll 1$, $\hat{\mathbf{n}} = (-\eta_x, -\eta_y, 1)$, and $S_* = 0$ results in

$$-K_h c_x \eta_x - K_h c_y \eta_y + w_s c + K_v c_z = 0 \quad \text{at} \quad z = \eta. \tag{3.6a}$$

At the bottom, using $|\nabla h| \ll 1$, $\hat{\mathbf{n}} = (-h_x, -h_y, -1)$, and $S_* = E - D$, where $E = w_s c_{\text{ref}}$ is the erosion and $D = w_s c_0$, the deposition. Here c_{ref} is a reference concentration and c_0 is the actual concentration at the bottom, i.e., $c_0 = c|_{z=-h}$. The bottom boundary condition thus becomes

$$-K_h c_x h_x - K_h c_y h_y - K_v c_z = w_s c_{\text{ref}}, \quad \text{at} \quad z = -h, \tag{3.6b}$$

with the reference concentration c_{ref} given as

$$c_{\text{ref}} = \frac{\rho_s a |\boldsymbol{\tau}_b|}{\rho_0 g' d_s}. \tag{3.6c}$$

Here $|\boldsymbol{\tau}_b|$ denotes the absolute value of the bed shear stress and $a(x, y)$ represents the availability of fine sediments at location (x, y). Note that $a(x, y)$ is a spatially varying coefficient parameterizing the ease with which fine sediments can be eroded and the amount of easily erodible fine sediments available at location (x, y) (Friedrichs *et al.* [22],

Chernetsky *et al.* [11] and Huijts *et al.* [9]). The sediment density is denoted by ρ_s, $g' = g(\rho_s - \rho)/\rho_0$ is the reduced gravity, and $d_s(x, y)$ is the grain size of the sediments.

It should be noted that in Eq. (3.4) the horizontal diffusivities are retained. However, to be consistent with the solution procedure for the hydrodynamic equations, the boundary layers for the suspended sediments will also not be resolved and the horizontal diffusivities will only play a role in the morphodynamic equilibrium condition (see section 3.2.4) . Hence Eq. (3.4), together with the boundary conditions given by Eq. (3.6) complete the system of equations governing the suspended sediment concentration in the estuary for given availability $a(x, y)$.

3.2.4. Condition of Morphodynamic Equilibrium

We consider a state of the system in which tidally averaged erosion and deposition balance each other:

$$\langle D - E \rangle = 0, \tag{3.7}$$

where $\langle \cdot \rangle$ denotes a tidally-averaged quantity (see Van Rijn [23] for more details). This condition is termed as the morphodynamic equilibrium condition (Chernetsky *et al.* [11], Huijts *et al.* [9] and Friedrichs *et al.* [22]).

Integrating the sediment concentration equation over the water column (from $z = -h$ to $z = \eta$) and using the boundary conditions for water motion and suspended sediment concentration at the free surface and at the bottom results in

$$\frac{\partial}{\partial t} \int_{-h}^{\eta} c \, dz + \frac{\partial}{\partial x} \int_{-h}^{\eta} \left(cu - K_h \frac{\partial c}{\partial x} \right) dz + \frac{\partial}{\partial y} \int_{-h}^{\eta} \left(cv - K_h \frac{\partial c}{\partial y} \right) dz + D - E = 0.$$

Averaging the above equation over the tidal period, using Eq. (3.7), we find that the condition of morphodynamic equilibrium requires that

$$\langle \frac{\partial}{\partial x} \int_{-h}^{\eta} \left(cu - K_h \frac{\partial c}{\partial x} \right) dz + \frac{\partial}{\partial y} \int_{-h}^{\eta} \left(cv - K_h \frac{\partial c}{\partial y} \right) dz \rangle = 0. \tag{3.8}$$

This condition together with the requirement that there is no tidally averaged sediment transport through the boundaries, can only be satisfied if the easily erodible fine sediment has a specific spatial distribution, i.e., Eq. (3.8) is effectively a condition for $a(x, y)$.

3.2.5. Scaling and Perturbation Analyses

Next, the equations for the water motion, suspended sediment concentration and morphodynamic equilibrium are scaled by introducing dimensionless variables. This results in the identification of a small parameter ϵ defined as

$$\epsilon = \bar{A}_{M_2}/H \ll 1.$$

Here, $\bar{A}_{M_2}$ is the mean elevation amplitude of the M_2 tide at the seaward boundary and H the mean depth at the seaward boundary. The order of magnitude of all other dimensionless numbers is related to this parameter ϵ, thus indicating the relative importance of each contribution. Next, the unknown physical variables are expanded in this small

parameter (see Nayfeh [24] for details about perturbation methods). These asymptotic expansions are inserted in the dimensionless system of equations and terms of equal order in ϵ are collected. This results in systems of equations at each order in ϵ (see A for a detailed description of the scaling and perturbation analyses).

In the following sections, we present the systems of equations in their dimensional form and the solution procedure used to solve the leading-order (ϵ^0) and first-order (ϵ^1) system of equations for the water motion (sections 3.3 and 3.4) and the suspended sediment concentration (sections 3.5 and 3.6). Finally, the sediment availability $a(x, y)$ is obtained by solving the condition of morphodynamic equilibrium which is encountered only at second order (ϵ^2).

For clarification, let us now introduce the notation convention. In ϕ^{mn}, where ϕ is any of the unknown physical variables, i.e., $\phi = \{\eta, \boldsymbol{u}, c\}$, the first superscript m denotes the order in ϵ of that contribution and the second superscript n its tidal frequency. For example, η^{02} denotes the leading-order (ϵ^0) M_2 surface elevation and $\boldsymbol{u}^{14}$ denotes the first-order (ϵ^1) M_4 velocity vector.

3.3. Leading-Order Water Motion

The leading-order system of equations for the water motion reads

$$u_x^0 + v_y^0 + w_z^0 = 0, \tag{3.9a}$$
$$u_t^0 - f v^0 = -g\eta_x^0 + (A_v u_z^0)_z, \tag{3.9b}$$
$$v_t^0 + f u^0 = -g\eta_y^0 + (A_v v_z^0)_z, \tag{3.9c}$$

with boundary conditions at the free surface

$$\rho_0 A_v (\boldsymbol{u}_h^0)_z = \mathbf{0}_h, \quad \text{and} \quad w^0 = \eta_t^0, \quad \text{at} \ \ z = 0.$$

Note that, as a result of the scaling procedure, this boundary condition is prescribed at $z = 0$ (see A for details). At the bottom $z = -h$, we require that

$$A_v(\boldsymbol{u}_h^0)_z = s\boldsymbol{u}_h^0, \quad \text{and} \quad w^0 = -u^0 h_x - v^0 h_y, \quad \text{at} \ \ z = -h.$$

The water motion at leading-order is only forced by the M_2 tidal constituent at the seaward boundary,

$$\eta^0 = A_{M_2} \cos(\omega t - \phi_{M_2}) \ \ \text{for all} \ \ (x, y) \ \text{in} \ \partial_S \Omega,$$

while the transport through the other boundaries vanishes

$$\int_{-h}^{0} \boldsymbol{u}_h^0 \cdot \hat{\mathbf{n}} \, dz = 0, \ \ \text{for all} \ \ (x, y) \ \text{in} \ \partial_R \Omega \ \text{or} \ \partial_C \Omega.$$

As already pointed out in section 3.2.2, it is assumed that the river inflow gives a contribution only at $\mathcal{O}(\epsilon)$ and hence does not appear in the leading order system of equations. The solution of this system of equations describes the propagation of a tidal wave in a homogeneous fluid (no density effects) in an estuary with an arbitrary geometry and bathymetry. Here, only a brief outline of the solution method is presented.

To solve the leading-order water motion (see Kumar *et al.* [17] for details), we write

$$(\eta^0, \boldsymbol{u}^0) = \Re\{(N^{02}, \boldsymbol{U}^{02})e^{i\omega t}\}, \tag{3.10}$$

where $\Re$ stands for the real part of a complex variable, and N^{02} and $\boldsymbol{U}^{02} = (U^{02}, V^{02}, W^{02})$ are spatially varying complex amplitudes of the surface elevation and the velocity field, respectively. The vertical structure of the leading-order velocity field can be obtained analytically using Eqs. (3.9b) and (3.9c); it is proportional to the first- and second-order partial derivatives of the leading-order surface elevation.

The surface elevation N^{02} and its partial derivatives are obtained by integrating the leading-order continuity equation (Eq. 3.9a) over the water column. Using the appropriate boundary conditions, a two-dimensional elliptic partial differential equation for the leading-order surface elevation N^{02} is obtained. This equation is solved numerically using the finite element method (see section 3.8 for details).

3.4. FIRST-ORDER WATER MOTION

The first-order system of equations for the water motion reads

$$u^1_x + v^1_y + w^1_z = 0, \tag{3.11a}$$

$$u^1_t + F^x_{AC} - f v^1 = -g\eta^1_x + F^x_{GC} + (A_v u^1_z)_z, \tag{3.11b}$$

$$v^1_t + F^y_{AC} + f u^1 = -g\eta^1_y + F^y_{GC} + (A_v v^1_z)_z, \tag{3.11c}$$

where $\{F^x_{AC}, F^y_{AC}\}$ denote the advective terms and $\{F^x_{GC}, F^y_{GC}\}$, the forcing due to density gradients. The different forcing terms are defined in Table 3.1. At the seaward boundary, an external M_4 tide (F_{EF}) is prescribed

$$\eta^1 = F_{EF}, \quad \text{for all} \ (x, y) \ \text{in} \ \partial_S\Omega. \tag{3.11d}$$

At the river boundary, a river discharge density Q' is prescribed, $F_{RD} = -Q'$,

$$\int_{-h}^{0} \boldsymbol{u}^1_h \cdot \hat{\boldsymbol{n}} \, dz + F^{\partial\Omega}_{TRF} = F_{RD}, \quad \text{for all} \ (x, y) \ \text{in} \ \partial_R\Omega. \tag{3.11e}$$

The total river discharge Q is distributed over the river boundary by requiring that

$$\int_{\partial_R\Omega} Q' \, ds = Q. \tag{3.11f}$$

The contribution $F^{\partial\Omega}_{TRF}$ is the transport through the boundary due to the correlation between the leading-order surface elevation and the velocity. At the closed boundary $\partial_C\Omega$, the total transport must vanish which implies that the first-order transport must balance the transport due to the correlation between the leading-order surface elevation and the velocity,

$$\int_{-h}^{0} \boldsymbol{u}^1_h \cdot \hat{\boldsymbol{n}} \, dz + F^{\partial\Omega}_{TRF} = 0, \quad \text{for all} \ (x, y) \ \text{in} \ \partial_C\Omega. \tag{3.11g}$$

At the free surface, the first-order stress must balance the stress due to the leading-order solution, denoted by F_{NS}, evaluated at $z = 0$.

$$\rho_0 A_v(\boldsymbol{u}_h^1)_z = -F_{NS}, \quad \text{at} \ \ z = 0. \tag{3.11h}$$

The forcing in the interior due to the correlation between the leading-order surface elevation and velocity, denoted by F_{TRF}^{Ω}, appears in the kinematic boundary condition as

$$w^1 = \eta_t^1 + F_{TRF}^{\Omega}, \quad \text{at} \ \ z = 0. \tag{3.11i}$$

For the boundary conditions at the bottom, no new forcing terms are obtained, i.e.,

$$A_v(\boldsymbol{u}_h^1)_z = s\boldsymbol{u}_h^1, \quad \text{and} \ \ w^1 = -u^1 h_x - v^1 h_y, \quad \text{at} \ \ z = -h. \tag{3.11j}$$

Since the leading-order flow is known, the system of equations for the first-order water

Name	Mathematical expression	Abbreviation	n
Externally prescribed			
Gravitational circulation	$\frac{g}{\rho_0} z(\rho_x, \rho_y)$	(F_{GC}^x, F_{GC}^y)	0
External M_4	$A_{M_4} \cos(2\omega t - \phi_{M_4})$	F_{EF}	4
River discharge	$-Q'$	F_{RD}	0
Internally generated			
Advection	$u^{02}(\boldsymbol{u}_h^{02})_x + v^{02}(\boldsymbol{u}_h^{02})_y + w^{02}(\boldsymbol{u}_h^{02})_z$	(F_{AC}^x, F_{AC}^y)	0,4
No-stress	$\rho_0 A_v \eta^{02} u_{zz}^{02}\vert_{z=0}$	F_{NS}	0,4
Tidal return flow	$\nabla \cdot (\eta^0 \boldsymbol{u}_h^{02})\vert_{z=0}$ $(\eta^{02} \boldsymbol{u}_h^{02}) \cdot \hat{\mathbf{n}}\vert_{\partial_R \Omega \cup \partial_C \Omega}$	F_{TRF}^{Ω} $F_{TRF}^{\partial\Omega}$	0,4

Table 3.1: Various forcing terms appearing in the first-order system of equations for the water motion (Eq. 3.11). The value of n denotes the frequency M_n of the forcing terms.

motion and its boundary conditions are linear in the unknown surface elevation η^1 and velocity field $\boldsymbol{u}^1 = (u^1, v^1, w^1)$. As a result, this equation can be solved for each forcing term F individually.

The forcing terms F can be divided into two categories: *externally prescribed* and *internally generated*. Table 3.1 gives a full list of all forcing terms for the first-order water motion. The externally prescribed forcing terms are those prescribed explicitly, e.g., the external M_4 tide, time-independent river discharge and density gradients. The internally generated forcing terms are generated by the non-linear interaction of the leading-order flow variables (advection, no-stress and tidal return flow). It is important to note that the forcing terms due to the non-linear interactions of leading-order water motion are either time-independent or are forcing terms with an M_4 periodicity. Therefore, both externally prescribed and internally generated forcing terms can be written as

$$F = \Re\{F^{1n} e^{\frac{ni\omega t}{2}}\}, \tag{3.12}$$

where $n = 0$ or 4 depending on the forcing term (see Table 3.1 for values of n). This allows us to write the solution of the first-order water motion as

$$(\eta^{1n}, \boldsymbol{u}^{1n}) = \Re\{(N^{1n}, \boldsymbol{U}^{1n})e^{\frac{ni\omega t}{2}}\},$$

where the terms with the superscript 10 ($n = 0$) denote first-order M_0 components and those with a superscript 14 ($n = 4$), first-order M_4 components. Here N^{1n} and $\boldsymbol{U}^{1n} = (U^{1n}, V^{1n}, W^{1n})$ are the spatially varying complex amplitudes of the first-order surface elevation and velocity field, respectively. The first-order system for n-th tidal frequency thus becomes

$$U_x^{1n} + V_y^{1n} + W_z^{1n} = 0, \tag{3.13a}$$

$$\frac{ni\omega}{2}U^{1n} + F_{AC}^{x,1n} - fV^{1n} = -gN_x^{1n} + F_{GC}^{x,10} + (A_v U_z^{1n})_z, \tag{3.13b}$$

$$\frac{ni\omega}{2}V^{1n} + F_{AC}^{y,1n} + fU^{1n} = -gN_y^{1n} + F_{GC}^{y,10} + (A_v V_z^{1n})_z. \tag{3.13c}$$

In a similar way, the boundary conditions can be expressed in terms of the complex amplitudes. This introduces new terms $F_{TRF}^{\Omega,1n}$ and $F_{TRF}^{\partial\Omega,1n}$ which denote the n-th frequency component of F_{TRF}^{Ω} and $F_{TRF}^{\partial\Omega}$, respectively.

To solve for the complex amplitudes N^{1n} and $\boldsymbol{U}^{1n}$, rotating flow variables are introduced:

$$r_1^{1n} = U^{1n} + iV^{1n}, \quad \text{and} \quad r_2^{1n} = U^{1n} - iV^{1n}. \tag{3.14}$$

Combining Eqs. (3.13b) and (3.13c), the equations for the rotating flow variables r_1^{1n} and r_2^{2n} are obtained:

$$r_{j,zz}^{1n} - (\alpha_j^n)^2 r_j^{1n} = \frac{g}{A_v}\mathcal{L}_j N^{1n} + F_{AC,j}^{1n} + F_{GC,j}^{10}, \quad \text{for } j = 1,2, \tag{3.15a}$$

together with the boundary conditions

$$\rho_0 A_v r_{j,z}^{1n} = F_{NS,j}^{1n}, \quad \text{at } z = 0, \tag{3.15b}$$

$$\rho_0 A_v r_{j,z}^{1n} = \rho_0 s r_j^{1n}, \quad \text{at } z = -h. \tag{3.15c}$$

In Eq. (3.15a), the operators $\mathcal{L}_j$ are defined by $\mathcal{L}_1 = \partial_x + i\partial_y$, and $\mathcal{L}_2 = \partial_x - i\partial_y$, and α_j^n by

$$\alpha_1^n = \sqrt{i\frac{n\omega + 2f}{2A_v}}, \quad \text{and} \quad \alpha_2^n = \sqrt{i\frac{n\omega - 2f}{2A_v}}, \quad n = 0,4.$$

For $n = 4$, α_1^n and α_2^n are related to the cyclonic and anticyclonic boundary layer thickness $\delta_\pm = \sqrt{\frac{2A_v}{n\omega/2\pm f}}$ associated with the M_4 tidal constituent (Soulsby [25], Souza [26]). Similarly, for $n = 0$, the parameters are related to the time-independent boundary layer thickness. The forcing terms in the equations for rotating variables are linear combinations of the forcing terms in the original equations; see Table 3.2.

Notation	Definition
$(F_{GC,1}^{10}, F_{GC,2}^{10})$	$-\frac{1}{A_v}(F_{GC}^{x,10} \pm iF_{GC}^{y,10})$
$(F_{AC,1}^{1n}, F_{AC,2}^{1n})$	$\frac{1}{A_v}(F_{AC}^{x,1n} \pm iF_{AC}^{y,1n})$
$(F_{NS,1}^{1n}, F_{NS,2}^{1n})$	$F_{NS}^{x,1n} \pm iF_{NS}^{y,1n}$

Table 3.2: Forcing terms appearing in the equations for rotating variables.

The equations for the rotating flow variables allow for analytical solutions,

$$r_j^{1n}(x, y, z) = c_{\alpha_j^n}(x, y, z)\mathscr{L}_j N^{1n} + f_{\alpha_j^n}(x, y, z), \quad j = 1, 2,$$

with

$$c_{\alpha_j^n}(x, y, z) = \frac{g}{(\alpha_j^n)^2 A_v}\left[\frac{s\cosh(\alpha_j^n z)}{\alpha_j^n A_v \sinh(\alpha_j^n h) + s\cosh(\alpha_j^n h)} - 1\right].$$

Expressions for $f_{\alpha_j^n}$ depend on the forcing term under consideration. Integrating these expressions over the depth gives

$$\int_{-h}^{0} r_j^n(x, y, z')\, dz' = C_{\alpha_j^n}(x, y)\mathscr{L}_j N^{1n} + F_{\alpha_j^n}(x, y), \quad j = 1, 2,$$

where

$$C_{\alpha_j^n}(x, y) = \frac{g}{(\alpha_j^n)^3 A_v}\left[\frac{s\sinh(\alpha_j^n h)}{\alpha_j^n A_v \sinh(\alpha_j^n h) + s\cosh(\alpha_j^n h)} - \alpha_j^n h\right].$$

Using Eq. (3.14), the depth-dependent and depth-integrated horizontal velocities are obtained in terms of the gradients of the surface elevation and known forcing terms as

$$(U^{1n}, V^{1n}) = (d_1, -d_2)N_x^{1n} + (d_2, d_1)N_y^{1n} + (f_1^{1n}, f_2^{1n}), \qquad (3.16)$$

$$\int_{-h}^{0}(U^{1n}, V^{1n})\, dz = (D_1, -D_2)N_x^{1n} + (D_2, D_1)N_y^{1n} + (F_1^{1n}, F_2^{1n}), \qquad (3.17)$$

where

$$(d_1^{1n}, f_1^{1n}, D_1^{1n}, F_1^{1n}) = \frac{1}{2}\left[(c_{\alpha_1^n}, f_{\alpha_1^n}, C_{\alpha_1^n}, F_{\alpha_1^n}) + (c_{\alpha_2^n}, f_{\alpha_2^n}, C_{\alpha_2^n}, F_{\alpha_2^n})\right],$$

$$(d_2^{1n}, f_2^{1n}, D_2^{1n}, F_2^{1n}) = \frac{i}{2}\left[(c_{\alpha_1^n}, -f_{\alpha_1^n}, C_{\alpha_1^n}, -F_{\alpha_1^n}) - (c_{\alpha_2^n}, -f_{\alpha_2^n}, C_{\alpha_2^n}, -F_{\alpha_2^n})\right].$$

To obtain the surface elevation, the first-order continuity equation is integrated over the water column (from $z = -h$ to $z = 0$). Together with the boundary conditions at $z = -h$ and $z = 0$, this gives

$$\frac{\partial}{\partial x}\int_{-h}^{0} U^{1n}\, dz + \frac{\partial}{\partial y}\int_{-h}^{0} V^{1n}\, dz + \frac{ni\omega}{2}N^{1n} + F_{TRF}^{\Omega,1n} = 0.$$

Inserting the expressions for depth-integrated horizontal velocity given by Eq. (3.16) in the above equation gives a second-order elliptic partial differential equation for the surface elevation N^{1n}

$$\nabla \cdot \left(\mathbf{D}^{1n}\nabla N^{1n} + \mathbf{F}^{1n}\right) + \frac{ni\omega}{2} N^{1n} + F_{TRF}^{\Omega,1n} = 0, \tag{3.18a}$$

where

$$\mathbf{D}^{1n} = \begin{pmatrix} D_1^{1n} & D_2^{1n} \\ -D_2^{1n} & D_1^{1n} \end{pmatrix}, \quad \text{and} \quad \mathbf{F}^{1n} = \begin{pmatrix} F_1^{1n} \\ F_2^{1n} \end{pmatrix}.$$

The associated horizontal boundary conditions read:

$$N^{1n} = F_{EF}^{14}, \quad \text{for all} \quad (x,y) \text{ in } \partial_S\Omega, \tag{3.18b}$$

$$(\mathbf{D}^{1n}\nabla N^{1n} + \mathbf{F}^{1n}) \cdot \hat{\mathbf{n}} + F_{TRF}^{\partial\Omega,1n} = F_{RD}^{10}, \quad \text{for all} \quad (x,y) \text{ in } \partial_R\Omega, \tag{3.18c}$$

$$(\mathbf{D}^{1n}\nabla N^{1n} + \mathbf{F}^{1n}) \cdot \hat{\mathbf{n}} + F_{TRF}^{\partial\Omega,1n} = 0, \quad \text{for all} \quad (x,y) \text{ in } \partial_C\Omega. \tag{3.18d}$$

Since this equation for the surface elevation is linear, it can be solved for each forcing term separately (i.e., each forcing term is studied individually by putting all other forcing terms to zero), thus resulting in explicit expressions for the first-order velocity due to each forcing term separately. The elliptic equation for N^{1n} has to be solved numerically, for details see section 3.8.

The first-order horizontal velocity $\boldsymbol{u}_h^1$ consists of a sum of M_0 and M_4 tidal constituents,

$$\boldsymbol{u}_h^1 = \boldsymbol{u}_h^{10} + \boldsymbol{u}_h^{14}, \tag{3.19a}$$

which can be further expressed as a sum of various constituents of the first-order water motion, i.e.,

$$\boldsymbol{u}_h^{10} = \boldsymbol{u}_{h,GC}^{10} + \boldsymbol{u}_{h,RD}^{10} + \boldsymbol{u}_{h,AC}^{10} + \boldsymbol{u}_{h,NS}^{10} + \boldsymbol{u}_{h,TRF}^{10}, \tag{3.19b}$$

$$\boldsymbol{u}_h^{14} = \boldsymbol{u}_{h,EF}^{14} + \boldsymbol{u}_{h,AC}^{14} + \boldsymbol{u}_{h,NS}^{14} + \boldsymbol{u}_{h,TRF}^{14}. \tag{3.19c}$$

Table 3.1 presents an explanation of abbreviations used in Eq. (3.19). The first-order vertical velocity W^{1n} are obtained by integrating the first-order continuity equation in the vertical direction from $z' = -h$ to $z' = z$ (see Kumar *et al.* [17] for a detailed explanation).

3.5. LEADING-ORDER SUSPENDED SEDIMENT CONCENTRA-TION

The leading-order equation for the suspended sediment concentration is given by

$$c_t^0 - (K_v c_z^0)_z - (w_s c^0)_z = 0. \tag{3.20a}$$

The boundary condition at the free surface reads

$$K_v c_z^0 + w_s c^0 = 0, \quad \text{at} \quad z = 0, \tag{3.20b}$$

and at the bottom

$$K_v c_z^0 + a \frac{w_s \rho_s}{\rho_0 g' d_s} |\boldsymbol{\tau}_b|^0 = 0, \quad \text{at} \ z = -h. \tag{3.20c}$$

Here $|\boldsymbol{\tau}_b|^0$ denotes the leading-order component of the absolute value of the bed shear stress. From Eq. (3.20), it follows that the leading-order suspended sediment concentration is solely driven by $|\boldsymbol{\tau}_b|^0$. Since the bed shear stress is written as the sum of a residual component and components with frequencies that are even multiples of the M_2 frequency, the leading-order suspended sediment concentration is also written as

$$c^0 = c^{00} + c^{04} + \dots$$

Even though Eq. (3.20) can be solved for any tidal constituent, only c^{00} and c^{04} are required to compute the leading-order residual transport (see Appendix C). To stress that the suspended sediment concentrations are linear in the unknown sediment availability $a(x, y)$, we can write

$$c^0 = a \tilde{c}^{0a} = a \tilde{c}^{00a} + a \tilde{c}^{04a} + \dots \tag{3.21}$$

Here, $\tilde{c}^{00a}$, $\tilde{c}^{04a}$ and $\tilde{c}^{0a}$ are the M_0, M_4 and total leading-order suspended sediment concentrations obtained with $a = 1$. The superscript a indicates that these concentrations are proportional to a.

3.6. FIRST-ORDER SUSPENDED SEDIMENT CONCENTRATION

The equation for the first-order suspended sediment concentration c^1 is given by

$$c_t^1 + F_{AC}^c - (K_v c_z^1)_z - (w_s c^1)_z = 0, \tag{3.22a}$$

where $F_{AC}^c = u^0 c_x^0 + v^0 c_y^0 + w^0 c_z^0$ expresses advection of the leading-order concentration by the leading-order velocity. At the surface, the first-order boundary condition reads

$$w_s c^1 + K_v c_z^1 = F_S^c, \quad \text{at} \ z = 0, \tag{3.22b}$$

where $F_S^c = -\eta_0 \left[w_s c_z^0 + K_v c_{zz}^0 \right]$ is the first-order correction to the balance between the leading-order settling and deposition fluxes (due to the fact that this flux is calculated at $z = 0$, instead of $z = \eta$, see also Appendix A). At the bottom, the boundary condition reads

$$K_v c_z^1 + a \frac{w_s \rho_s}{\rho_0 g' d_s} |\boldsymbol{\tau}_b|^1 = 0, \quad \text{at} \ z = -h. \tag{3.22c}$$

Here $|\boldsymbol{\tau}_b|^1$ denotes the first-order component of the absolute value of the bed shear stress.

The first-order suspended sediment concentration is the result of three different forcing terms, the advection of the leading-order concentration by the leading-order velocity (F_{AC}^c), the surface contribution (F_S^c) and the first-order bed shear stress (F_{BS}^c). Since the equation is linear, the resulting first-order concentration is solved for each forcing individually.

At this point, it is important to remember that our aim is to get the main contributions to the first-order residual sediment transport (see section 3.1). The only first-order residual sediment transport that depends on the first-order suspended sediment concentration c^1, is due to the tidally-averaged advection of c^1 by the leading-order velocities $\mathbf{u}^0$. Since the leading-order velocity only consists of an M_2 tidal constituent, only the M_2 constituent of the first-order suspended sediment concentration c^1 has to be calculated to get the residual suspended sediment transport due to the first-order suspended sediment concentrations. (see sections 3.1 and 3.7). Therefore, in the following only the construction of the M_2 first order concentration will be discussed in detail.

3.6.1. CONTRIBUTION DUE TO ADVECTION

The equation governing the first-order suspended sediment concentration, resulting from the interaction of leading-order velocity and concentration, is given by

$$c^1_{AC,t} + F^c_{AC} - (K_v c^1_{AC,z})_z - (w_s c^1_{AC})_z = 0, \tag{3.23a}$$

with homogeneous boundary conditions

$$w_s c^1_{AC} + K_v c^1_{AC,z} = 0, \quad \text{at } z = 0, \tag{3.23b}$$

$$K_v c^1_{AC,z} = 0, \quad \text{at } z = -h. \tag{3.23c}$$

Since F^c_{AC} contains the gradients of the leading-order suspended sediment concentration, using Eq. (3.21), F^c_{AC} can be written as a sum of contributions proportional to a, a_x and a_y, i.e.,

$$F^c_{AC} = a F^a_{AC} + a_x F^{a_x}_{AC} + a_y F^{a_y}_{AC}, \tag{3.24}$$

where $F^a_{AC} = \tilde{c}^{0a}_x u^0 + \tilde{c}^{0a}_y v^0 + \tilde{c}^{0a}_z w^0$, $F^{a_x}_{AC} = \tilde{c}^{0a} u^0$, and $F^{a_y}_{AC} = \tilde{c}^{0a} v^0$. Since the leading-order flow consists only of an M_2 tidal constituent, we only need the M_0 and M_4 tidal constituents of the leading-order concentration c^0 to get the M_2 tidal component of F^c_{AC}.

Denoting the M_2 solution of c^1_{AC} as c^{12}_{AC}, we find that (see Appendix C for details)

$$c^{12}_{AC} = a \tilde{c}^{12a}_{AC} + a_x \tilde{c}^{12a_x}_{AC} + a_y \tilde{c}^{12a_y}_{AC}, \tag{3.25}$$

where $\tilde{c}^{12a}_{AC}, \tilde{c}^{12a_x}_{AC}$, and $\tilde{c}^{12a_y}_{AC}$ are the solutions proportional to a, a_x and a_y, respectively.

3.6.2. CONTRIBUTION DUE TO FIRST-ORDER BED SHEAR STRESS

Analogous to the case of leading-order suspended sediment concentration, the first-order component of the absolute value of the bed sear stress $|\boldsymbol{\tau}_b|^1$ is decomposed in a Fourier series using frequencies that are multiples of the M_2 tidal frequency. To get the dominant residual transport component, we are only interested in the M_2 component $|\boldsymbol{\tau}_b|^{12}$ of the first-order component of the absolute value of the bed shear stress $|\boldsymbol{\tau}_b|^1$.

The resulting suspended sediment concentration c^{12}_{BS} follows from the equation,

$$c^{12}_{BS,t} - (K_v c^{12}_{BS,z})_z - (w_s c^{12}_{BS})_z = 0,$$

with the boundary conditions,

$$w_{\mathrm{s}} c_{BS}^{12} + K_{\mathrm{v}} c_{BS,z}^{12} = 0, \quad \text{at} \ \ z = 0,$$

$$K_{\mathrm{v}} c_{BS,z}^{12} + a \frac{w_{\mathrm{s}} \rho_{\mathrm{s}}}{\rho_0 g' d_{\mathrm{s}}} |\boldsymbol{\tau}_b|^{12} = 0, \quad \text{at} \ \ z = -h,$$

where $|\boldsymbol{\tau}_b|^{12}$ denotes the M_2 component of $|\boldsymbol{\tau}_b|^1$. Similar to the leading-order suspended sediment concentration, we can define

$$c_{BS}^{12} = a \tilde{c}_{BS}^{12a}.$$

Note that $|\boldsymbol{\tau}_b|^{12}$ depends on the first-order velocity which itself is a sum of various contributions, for each of which we can compute the resulting suspended sediment concentration c_{BS}^{12}. In Table 3.3, a list of all these components is given.

$\boldsymbol{u}_{\mathrm{h}}^1$	$\boldsymbol{u}_{\mathrm{h}}^1$ components	c_{BS}^{12} components
	$\boldsymbol{u}_{\mathrm{h,GC}}^{10}$	$c_{BS,GC}^{12}$
	$\boldsymbol{u}_{\mathrm{h,RD}}^{10}$	$c_{BS,RD}^{12}$
$\boldsymbol{u}_{\mathrm{h}}^{10}$	$\boldsymbol{u}_{\mathrm{h,AC}}^{10}$	$c_{BS,AC10}^{12}$
	$\boldsymbol{u}_{\mathrm{h,NS}}^{10}$	$c_{BS,NS10}^{12}$
	$\boldsymbol{u}_{\mathrm{h,TRF}}^{10}$	$c_{BS,TRF10}^{12}$
	$\boldsymbol{u}_{\mathrm{h,EF}}^{10}$	$c_{BS,EF}^{12}$
$\boldsymbol{u}_{\mathrm{h}}^{14}$	$\boldsymbol{u}_{\mathrm{h,AC}}^{14}$	$c_{BS,AC14}^{12}$
	$\boldsymbol{u}_{\mathrm{h,NS}}^{14}$	$c_{BS,NS14}^{12}$
	$\boldsymbol{u}_{\mathrm{h,TRF}}^{14}$	$c_{BS,TRF14}^{12}$

Table 3.3: Various components of the first-order velocity (*first column*) and (corresponding) first-order concentration due to the bed shear stress (*second column*).

3.6.3. Contribution due to forcing at the surface
The last contribution is the result of the inhomogeneous contribution in the boundary condition at the surface (Eq. 3.22b). Using the leading-order concentration equation, we can rewrite this surface boundary condition as

$$F_S^c = -\eta^0 \left[w_{\mathrm{s}} c_z^0 + K_{\mathrm{v}} c_{zz}^0 \right] = -\eta^0 c_t^0,$$
$$= -\eta^{02} c_t^{04},$$
$$= -a \eta^{02} \tilde{c}_t^{04a}.$$

This inhomogeneous term $\eta^0 c^{04}$ results in both M_2 and M_6 contributions. The resulting solution for the M_2 component of the first-order suspended sediment concentration due to the surface forcing is written as,

$$c_S^{12} = a \tilde{c}_S^{12a}.$$

3.6.4. SUMMARY OF THE FIRST-ORDER CONCENTRATION

The M_2 constituent of the first-order suspended sediment concentration is a sum of three components,

$$
\begin{aligned}
c^{12} &= c_{AC}^{12} + c_{BS}^{12} + c_S^{12} \\
&= a \underbrace{(\tilde{c}_{AC}^{12a} + \tilde{c}_{BS}^{12a} + \tilde{c}_S^{12a})}_{\tilde{c}^{12a}} + a_x \underbrace{\tilde{c}_{AC}^{12a_x}}_{\tilde{c}^{12a_x}} + a_y \underbrace{\tilde{c}_{AC}^{12a_y}}_{\tilde{c}^{12a_y}} \\
&= a\tilde{c}^{12a} + a_x\tilde{c}^{12a_x} + a_y\tilde{c}^{12a_y}.
\end{aligned}
$$

It means that the first-order suspended sediment concentration consists of parts proportional to a, a_x and a_y. It is important to note that proportionality of the suspended sediment concentration to a_x and a_y is solely due to the advective component.

3.7. CONDITION OF MORPHODYNAMIC EQUILIBRIUM

The leading-order morphodynamic equilibrium follows from inserting the asymptotic expansions of the horizontal velocities and concentrations in Eq. (3.8) and reads

$$
\nabla \cdot (\mathbf{D}^a \nabla a + a\mathbf{T}) = 0, \tag{3.26a}
$$

where

$$
\mathbf{D}^a = \begin{pmatrix} D_{K_h} + T_{M_2}^{xa_x} & T_{M_2}^{xa_y} \\ T_{M_2}^{ya_x} & D_{K_h} + T_{M_2}^{ya_y} \end{pmatrix}, \text{ and } \mathbf{T} = \begin{pmatrix} T^{xa} \\ T^{ya} \end{pmatrix}.
$$

Here, D_{K_h} is the contribution due to the horizontal diffusivity and the terms $T_{M_2}^{xa_x}$, $T_{M_2}^{xa_y}$, $T_{M_2}^{ya_x}$, and $T_{M_2}^{ya_y}$ are generated by the interaction of M_2 velocity and M_2 advective concentration.

The terms T^{xa} and T^{ya} denote the leading-order tidally-averaged sediment transport in the x and y directions, respectively. The transport T^{xa} is a sum of various terms (see D for detailed expressions)

$$
T^{xa} = T_{M_0}^{xa} + T_{M_2}^{xa} + T_{M_4}^{xa} + T_{\text{surface}}^{xa} + T_{\text{diff}}^{xa}, \tag{3.26b}
$$

where $T_{M_0}^{xa}$ denotes the transport due to the interaction of the M_0 velocity and M_0 concentration. Remember that the M_0 velocity itself consists of various contributions (Table 3.3), for each of which we can compute $T_{M_0}^{xa}$ (see Table 3.4 for a full list of all subcomponents). $T_{M_2}^{xa}$ is the transport due to the correlation between the M_2 velocity and M_2 concentration. Again, the M_2 concentration consists of various contributions (Table 3.3), implying that $T_{M_2}^{xa}$ can be computed for each contribution. Similarly, $T_{M_4}^{xa}$ is generated by the interaction of M_4 velocity and M_4 concentration. Once again, the M_4 velocity is a sum of various components as listed in Table 3.4 which allows us to decompose it into further subcomponents. Table 3.4 lists all the subcomponents of $T_{M_0}^{xa}$, $T_{M_2}^{xa}$, and $T_{M_4}^{xa}$. The component T_{surface}^{xa} is the transport due to the interaction of M_2 surface elevation, M_2 velocity and the leading-order concentration at the surface and T_{diff}^{xa} is the diffusive transport (see D for expressions). A similar decomposition can be made for the transport in the y-direction T^{ya}.

Velocity		Concentration	Transport
$T_{M_0}^{xa}$			
u^{10}	u_{GC}^{10}	$\tilde{c}^{00}$	$T_{M_0,GC}^{xa}$
	u_{RD}^{10}		$T_{M_0,RD}^{xa}$
	u_{AC}^{10}		$T_{M_0,AC}^{xa}$
	u_{NS}^{10}		$T_{M_0,NS}^{xa}$
	u_{TRF}^{10}		$T_{M_0,TRF}^{xa}$
$T_{M_2}^{xa}$			
u^{02}		$\tilde{c}_{AC}^{12}$	$T_{M_2,AC}^{xa}$
		$\tilde{c}_{S}^{12}$	$T_{M_2,S}^{xa}$
		$\tilde{c}_{BS}^{12}$ $\tilde{c}_{BS,GC}^{12}$	$T_{M_2,BS,GC}^{xa}$
		$\tilde{c}_{BS,RD}^{12}$	$T_{M_2,BS,RD}^{xa}$
		$\tilde{c}_{BS,AC10}^{12}$	$T_{M_2,BS,AC10}^{xa}$
		$\tilde{c}_{BS,NS10}^{12}$	$T_{M_2,BS,NS10}^{xa}$
		$\tilde{c}_{BS,TRF10}^{12}$	$T_{M_2,BS,TRF10}^{xa}$
		$\tilde{c}_{BS,EF}^{12}$	$T_{M_2,BS,EF}^{xa}$
		$\tilde{c}_{BS,AC14}^{12}$	$T_{M_2,BS,AC14}^{xa}$
		$\tilde{c}_{BS,NS14}^{12}$	$T_{M_2,BS,NS14}^{xa}$
		$\tilde{c}_{BS,TRF14}^{12}$	$T_{M_2,BS,TRF14}^{xa}$
$T_{M_4}^{xa}$			
u^{14}	u_{EF}^{14}	$\tilde{c}^{04}$	$T_{M_4,EF}^{xa}$
	u_{AC}^{14}		$T_{M_4,AC}^{xa}$
	u_{NS}^{14}		$T_{M_4,NS}^{xa}$
	u_{TRF}^{14}		$T_{M_4,TRF}^{xa}$

Table 3.4: Decomposition of various transport terms $T_{M_0}^{xa}$, $T_{M_2}^{xa}$, and $T_{M_4}^{xa}$ into subcomponents. A similar decomposition can be made for the transport terms in the lateral direction.

To solve Eq. (3.26a) for the sediment availability, we require that the transport vanishes at the boundary,

$$(\mathbf{D}^a \nabla a + a\mathbf{T}) \cdot \hat{\mathbf{n}} = 0, \text{ on } \partial_S\Omega \cup \partial_R\Omega \cup \partial_C\Omega. \qquad (3.26c)$$

The equation for sediment availability a together with the no-transport condition (Neumann type boundary condition) above does not give a unique solution for the sediment availability a. Therefore, an extra condition is imposed, namely the total amount of sed-

iment available for erosion a_{total} in the estuary is prescribed,

$$\iint_{\Omega} a \, d\Omega = a_{\text{total}}. \tag{3.26d}$$

Equation (4.11) has to be solved numerically for general domains. Here, we use the finite element method which is described in the next section.

3.8. NUMERICAL SOLUTION

In sections 3.3 and 3.4, it was shown that the leading-order and first-order water motion could be expressed in terms of the gradients of the surface elevation. The surface elevation itself follows from a two-dimensional elliptic partial differential equation. Similarly, the sediment availability (section 3.7) follows from an elliptic differential equation (Eq. 3.26a). Since the geometry and the bathymetry of the estuary are arbitrary and the parameters can be arbitrary functions of the horizontal coordinates, these equations have to be solved numerically. Here, we discuss the solution method used, the finite element method (FEM) approach, and the accuracy of the numerical solution.

To solve the equations using the FEM approach, the domain Ω is discretized using linear triangles. The discretized domain is denoted as $\Omega_{\tilde{h}}$, with $\tilde{h}$ the mean of the length of all the element edges in the discretized domain. The solution N is approximated as

$$N(x, y) \approx N_{\tilde{h}}(x, y) = \sum_{j=1}^{n} N_j \phi_j(x, y), \tag{3.27}$$

where $N_{\tilde{h}}$ is the finite element approximation of N. The total number of grid points (also called nodal points) is denoted by n, N_j are the amplitudes at nodal points j, and ϕ_j are the basis functions such that ϕ_j is zero at all nodal points except node j. Here, polynomials functions are chosen as basis functions. Inserting the approximation of N given by Eq. (3.27) in the weak formulation of the partial differential equation for the surface elevation gives a linear system of equations which can be solved for the unknown amplitudes N_j (see Kumar *et al.* [17] for details).

In Kumar *et al.* [17], three methods namely; DD-method, ZZ-method and mixed-method, were discussed to compute the first- and second-order partial derivatives of the surface elevation. It was shown that for the leading-order flow, the mixed-method which is a hybrid of DD-method and ZZ-method, works best. However, partial derivatives of the leading-order flow are needed to compute the first-order water motion and the sediment availability, which is not possible with the mixed method. Therefore, we adopt the DD-method throughout the model to compute the partial derivatives of any order. Using the DD-method, the partial derivatives of N can be approximated by directly differentiating $N_{\tilde{h}}$ as

$$\frac{\partial^{a+b} N}{\partial x^a \partial y^b} \approx \frac{\partial^{a+b} N_{\tilde{h}}}{\partial x^a \partial y^b} = \sum_{j=1}^{n} N_j \frac{\partial^{a+b} \phi_j}{\partial x^a \partial y^b},$$

where a and b are the orders of differentiation in the x and y directions, respectively.

The accuracy of the finite element approximation $N_{\tilde{h}}$ and its partial derivatives depends on the degree of basis polynomials. In general, if polynomials of degree q are

Component		Accuracy
η^0		$q+1$
$\boldsymbol{u}^0$	$\boldsymbol{u}_h^0$	q
	w^0	$q-1$
η^1		$q-1$
$\boldsymbol{u}_h^1$		$q-2$
c^0		q
c^1		$q-2$
a		$q-2$

Table 3.5: The accuracy of the various components of the model when polynomials of degree q for the leading-order water motion and polynomials of degree at least $q-1$ for the first-order water motion and sediment availability, are used as basis functions.

used, the numerical solution converges with rate $q+1$, the first-order partial derivatives with rate q and the second order partial derivatives with rate $q-1$ (see Gockenbach [27]). Indeed, for the leading-order water motion, Kumar *et al.* [17] has shown that using basis functions of order q_0, the surface elevation converges with rate q_0+1, the first-order partial derivatives with q_0 and second-order partial derivatives with rate q_0-1. Hence, the leading-order horizontal velocity (proportional to the first-order partial derivatives of the leading-order water motion) and vertical velocity (proportional to the second-order partial derivatives of the leading-order surface elevation) converge with rate q_0 and q_0-1, respectively.

In sections 3.4, 3.5 and 3.6, it was shown that to compute the first-order water motion and suspended sediment concentration, not only the leading-order flow components but also their partial derivatives are required. This is because these partial derivatives appear in the forcing terms for the first-order flow and first-order sediment concentration. For the first-order horizontal water motion to be q_1 accurate, the forcing terms must at least be q_1 accurate as well. Hence, it follows that q_0 must be at least equal to or larger than q_1+1, i.e., the degree of basis polynomials used to solve the leading-order water motion must be at least one higher than those used in the first-order water motion.

Table 3.5 lists the accuracy of different components of the model if polynomials of degree q are used as basis functions for the leading-order water motion and polynomials of degree $q-1$ are used as basis functions for the other components (i.e., first-order water surface elevation and sediment availability). If we take $q=3$, i.e., third degree polynomials as basis functions for the leading-order water motion and quadratic polynomials as basis functions for rest of the components, it follows from Table 3.5 that the sediment availability converges with rate 1.

3.9. APPLICATION TO THE EMS ESTUARY

In this section, the new three-dimensional semi-idealized model is applied to investigate the spatial distribution of concentration and sediment availability in the Ems estuary under the condition of morphodynamic equilibrium. The Ems estuary is situated on the border of the Netherlands and Germany and has gone through various anthropogenic

changes in the last few decades. Due to these interventions, the water motion and the sediment dynamics have changed significantly (De Jonge *et al.* [4]).

The Ems estuary is located between the island of Borkum in the North Sea and the weir at Herbrum and has a total length of approximately 100 km. In this chapter, we only focus on the upper part of the Ems estuary, starting from Knock (Fig. 3.3). The length L of the estuary from Knock to Herbrum is approximately 63.7 km. Following Chernetsky
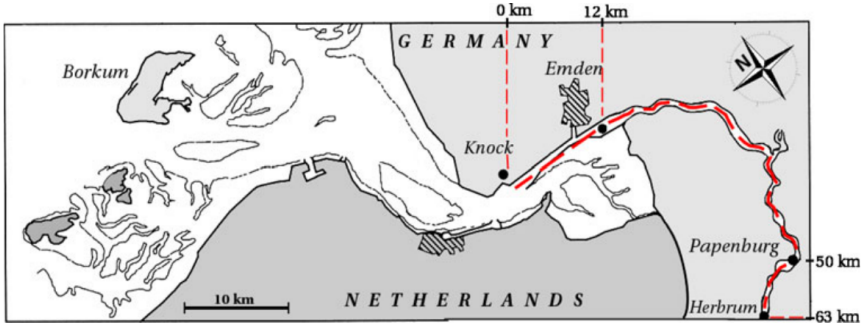
Figure 3.3: The map of the Ems estuary (Chernetsky *et al.* [11]).

et al. [11], the geometry of the Ems estuary can be approximated as funnel-shaped with x and y denoting the along-channel and cross-channel coordinates, respectively. The along-channel coordinate varies from $x = 0$ at the seaward side to $x = L$ at the river side. The lateral coordinate y varies between $y = -B(x)$ and $y = B(x)$, with $B(x)$ given by

$$B(x) = B_0 e^{-x/L_b}.$$

Here, $2B_0$ is the total width at the seaward side and L_b is the *e*-folding length scale. The estuary is assumed to be well-mixed and the dynamic density ρ is assumed to vary as

$$\rho = \rho_0 \left[1 + \beta \, \tilde{s}(x) \right],$$

where $\tilde{s}(x)$ is the prescribed tidally- and depth-averaged salinity distribution obtained from Talke *et al.* [3] and $\beta = 7.6 \times 10^{-4}$ psu^{-1} is a coefficient that relates salinity to density.

In this chapter, two years (1980 and 2005) are studied. Following De Jonge *et al.* [4], the bathymetric profiles for the years 1980 and 2005 are fitted with a fourth degree polynomial in the along-channel direction using observational data. Following Friedrichs and Hamrick [28] and Schramkowski *et al.* [21], the coefficient of vertical mixing A_v and the stress parameter s are parameterized as

$$(s, A_v) = (s_0, A_{v0}) \frac{h}{H}.$$

Here A_{v0} and s_0 are the reference eddy viscosity and stress parameter, and H is the mean depth at the seaward side. The system is forced with a combination of M_2 and M_4 tides at the seaward side ($x = 0$),

$$\eta = A_{M_2} \cos(\omega t) + A_{M_4} \cos(2\omega t - \phi),$$

where A_{M_2} and A_{M_4} are the elevation amplitudes defined in section 3.2.2 and $\phi = \phi_{M_4} - 2\phi_{M_2}$ is the relative phase between the M_2 and M_4 tidal constituents. In 1980, the mean tidal range at Knock was approximately 3.1 m with a relative phase of -171.9 degree. The tidal range in 2005 was 3.2 m with a relative phase of -174.6 degree (see Chernetsky *et al.* [11] for details). A constant river discharge of $Q = 80$ m^3 s^{-1} is prescribed at the river boundary ($x = L$). A river discharge density Q' satisfying Eq. (3.11f) is defined as

$$Q' = \frac{Q}{2B|_{x=L}}.$$

Table 3.6 gives a list of all parameters used for the years 1980 and 2005 such that the observed M_2 water motion is well-reproduced by the model (see Kumar *et al.* [17] for a discussion). Using these parameters, Table 3.7 lists the order of magnitude of various dimensionless parameters for the Ems estuary. Table 3.7 shows that the Ems estuary is tidally-dominated and river discharge gives a first-order contribution.

Parameter	1980-value	2005-value
L	63.7 km	
L_b	30 km	
B_0	335 m	
H	10 m	
g	9.8 m s^{-2}	
f	1.34×10^{-4} s^{-1}	
ω	1.4×10^{-4} s^{-1}	
ρ_0	1020 kg m^{-3}	
ρ_s	2650 kg m^{-3}	
β	7.6×10^{-4} psu^{-1}	
A_{M_2}	1.43 m	1.35 m
A_{M_4}	0.25 m	0.19 m
ϕ	-170.9°	-174.6°
A_{v_0}	0.0184 m^2 s^{-1}	0.0135 m^2 s^{-1}
s_0	0.1421 m s^{-1}	0.0108 m s^{-1}
Q	80 m^3 s^{-1}	
w_s	1.0×10^{-3} m s^{-1}	
K_h	100 m^2 s^{-1}	
a_{total}	582 m^2	2710.8 m^2

Table 3.6: Parameters for the years 1980 and 2005 for the Ems estuary (De Jonge *et al.* [4]).

3.9.1. LATERALLY UNIFORM BATHYMETRY
The width-averaged bed profile of the Ems estuary for the years 1980 and 2005, used in De Jonge *et al.* [4], are extended uniformly in the lateral direction (Fig. 3.4) to be used in the 3D semi-idealized model. The domain is discretized using approximately 100,000 nodes. A realistic value of the Coriolis parameter $f = 1.34 \times 10^{-4}$ s^{-1}, corresponding to the Ems estuary, is used. The total amount of easily erodible sediment in the estuary

Dimensionless parameter	1980	2005	Order
$\bar{A}_{M_2}/H = \epsilon$	0.14	0.13	$\mathcal{O}(\epsilon)$
$U/\omega L$	0.1		$\mathcal{O}(\epsilon)$
$\bar{A}_{M_4}/\bar{A}_{M_2}$	0.17	0.14	$\mathcal{O}(\epsilon)$
$gH/\omega^2 L^2$	1.22		$\mathcal{O}(1)$
U_d/U	0.1		$\mathcal{O}(\epsilon)$
$A_{v0}/\omega H^2$	1.31	0.96	$\mathcal{O}(1)$
$Q/\bar{Q}$	0.1		$\mathcal{O}(\epsilon)$
$w_s/\omega H$	0.71		$\mathcal{O}(1)$

Table 3.7: Order of magnitude of dimensionless parameters for the Ems estuary.

a_{total} is chosen in such a way that the maximum concentration at the surface for 1980 and 2005 matches the observations, i.e., 400 mg L^{-1} for 1980 and 1000 mg L^{-1} for 2005 (from De Jonge *et al.* [4]).
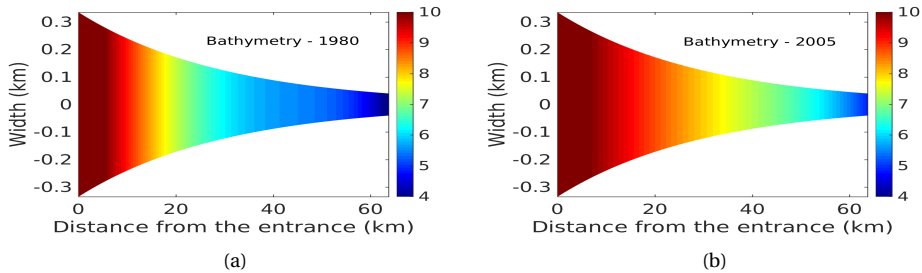
Figure 3.4: Bathymetry of the Ems estuary for the years 1980 and 2005 assuming laterally uniform conditions. The units in the colorbar are m.

In Fig. (3.5), top panel, the distribution of easily erodible sediment in the Ems estuary is shown for the years 1980 and 2005. Since the bed profile is laterally uniform, the sediment availability is also uniform in the lateral direction. The easily erodible sediment is concentrated close to the seaward side, approximately 6 km into the estuary, for the year 1980. For the year 2005, the easily erodible sediment is concentrated approximately 41 km away from the entrance and is more widely spread (in along-channel direction) in the estuary than for 1980.

Next, we look at the tidally-averaged suspended sediment concentration at the surface. From Fig.(3.5), lower panel, it follows that for 1980, the maximum sediment concentration is found closer to the seaward side, approximately 7 km from the entrance and for 2005, at approximately 38 km from the entrance. The locations of maximum concentration are consistent with those found in Chernetsky *et al.* [11], i.e., the ETM is found close to the seaward side for 1980 and more landward for 2005. Note that, because of the Coriolis parameter, the maximum availability of fine sediments and the maximum sediment concentration at the surface for both the years, shown by grey dots in Fig. (3.5), are found on the northern sides than in the middle of the channel.
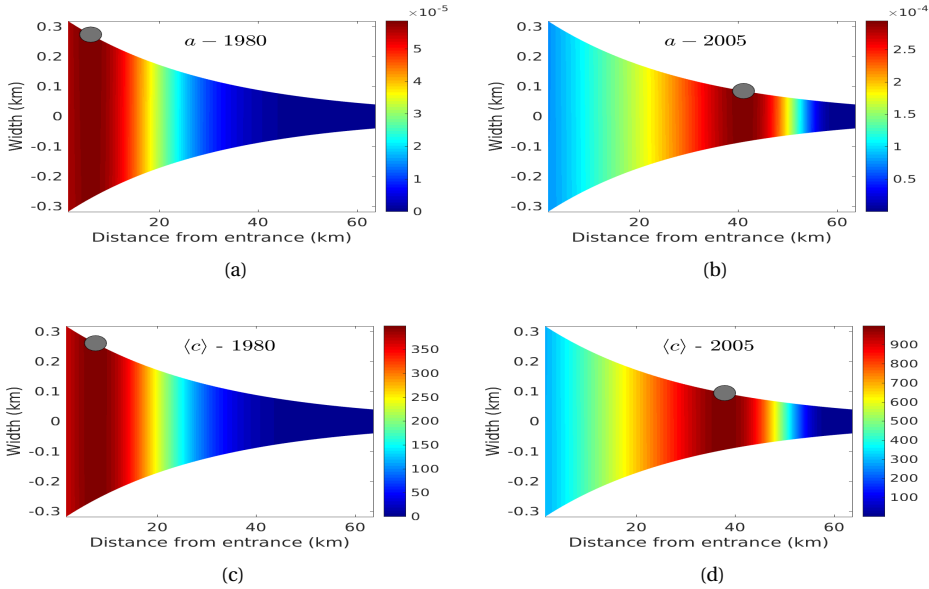
Figure 3.5: Sediment availability (dimensionless) in the channel for the years 1980 (*top left*) and 2005 (*top right*). The tidally-averaged suspended sediment concentration at the surface for the years 1980 (*bottom left*) and 2005 (*bottom right*). The units in the colorbar are mg l^{-1}. The grey dots show the location of the maxima of the quantity being plotted. Note that the total amount of easily erodible sediment a_{total} is chosen in such a way that the maximum concentration at the surface for 1980 is 400 mg l^{-1} and for 2005 is 1000 mg l^{-1}.

3.9.2. LATERALLY VARYING BATHYMETRY

In this experiment, the bathymetric profile in the lateral direction is varied parabolically requiring that the width-averaged depth remains the same as in the first experiment (Fig. 3.6). This preserves the mean depth of the channel in both the experiments. For both years, a_{total} used in the previous experiment is used.
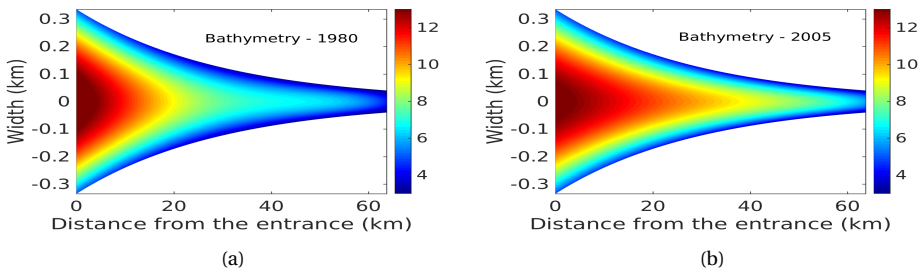
Figure 3.6: The bathymetry of the Ems estuary for the years 1980 and 2005 varying parabolically in the lateral direction. The units in the colorbar are m.

From Figs. 3.7(a) and 3.8(a), it follows that the easily erodible sediments are not dis-

tributed uniformly in the lateral direction: the availability is much higher on the shallow sides than in the deeper channel for both years. However, the along-channel location of maximum availability is approximately the same as in the experiment with laterally uniform bathymetry. The maximum availability of fine sediments is higher for a laterally varying bed profile than for a laterally uniform bed profile.

(a)

(b)

(c)

(d)
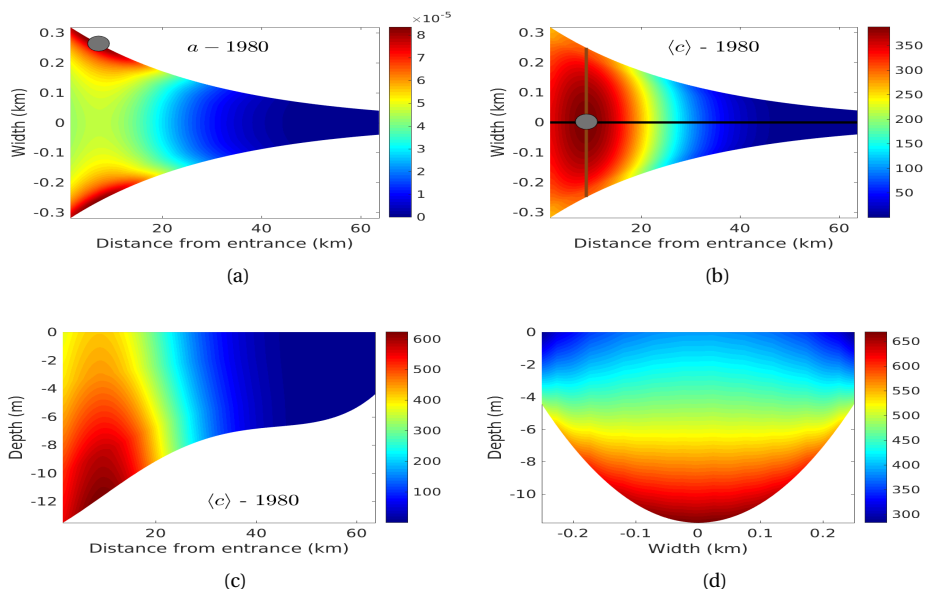
Figure 3.7: Sediment availability and sediment concentration for 1980 with laterally varying bed profile. The *top left panel* shows the sediment availability (dimensionless) and *top right panel*, the sediment concentration $(\mathrm{mg\,l^{-1}})$ at the surface. The black and chocolate lines pass through the location of maximum concentration at the surface in the x and y directions, respectively. The grey dot indicates the location of the maximum of the quantity being plotted. The *bottom left panel* shows the cross-sectional profile of the sediment concentration along the black line and the *bottom right panel*, along the chocolate line.

For the year 1980, the maximum sediment concentration at the surface is found at approximately 8 km from the entrance (Fig. 3.7(b)) compared with 38 km for the year 2005 (Fig. 3.8(b)). The locations of maximum concentration move slightly landward for 1980 compared with the case with laterally uniform bed profile. The maximum sediment concentrations are found in the middle of the channel even though the sediment availability is lower in the middle than on the shoals. Note that, unlike the case with laterally uniform bed profile, the Coriolis parameter does not significantly influence the location of the maximum concentration in the lateral direction. This is because the influence of laterally varying bathymetric profile on the longitudinal processes is stronger than those induced by the Coriolis force.

To illustrate the strength of the 3D model, the vertical profile of the sediment concentration is plotted in the along-channel and cross-channel directions passing through the location of maximum concentration at the surface. These locations are shown by black and chocolate lines in Fig. 3.7(b) for 1980 and Fig. 3.8(b) for 2005. The along-channel
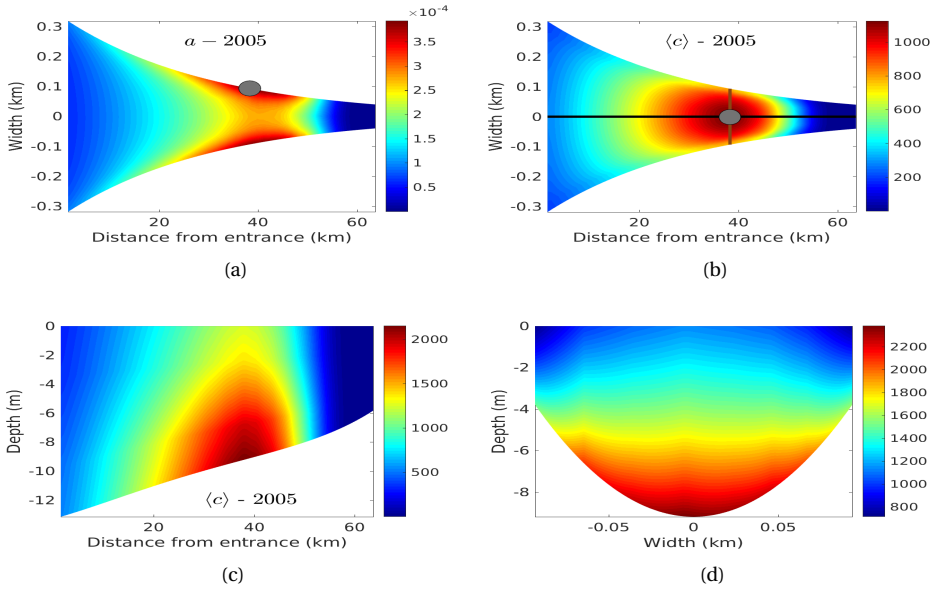
Figure 3.8: Sediment availability and sediment concentration for 2005 with laterally varying bed profile. The *top left panel* shows the sediment availability (dimensionless) and *top right panel*, the sediment concentration (mg l^{-1}) at the surface. The black and chocolate lines pass through the location of maximum concentration at the surface in the x and y directions, respectively. The grey dot indicates the location of the maximum of the quantity being plotted. The *bottom left panel* shows the cross-sectional profile of the sediment concentration along the black line and the *bottom right panel*, along the chocolate line.

profile of the sediment concentration (Figs. 3.7(c) and 3.8(c)) shows that the region of high concentration is much wider at the bottom than at the surface. Moreover, the ETM in the along-channel direction is stronger and wider for 2005 than for 1980. The vertical profile of the sediment concentration in the cross-channel direction for 1980 and 2005 (Figs. 3.7(d) and 3.8(d)) depicts similar structure. Also, for both years, the maximum concentrations are found in the deepest parts of the channel, with maximum concentration at the bottom being almost two times the maximum concentration at the surface (Figs. 3.7(d) and 3.8(d)).

Using a realistic (but smoothed) bathymetry and geometry for the Ems estuary in 2005, the trapping of fine sediments is still mainly observed at the landward side of the estuary (see Fig. 3.9(a), and Fig. 3.9(b) in which only the (scaled) surface suspended sediment concentrations is shown), which qualitatively agrees with observations (De Jonge *et al.* [4]). In Fig. (3.9(c)), the sediment availability in morphodynamic equilibrium is shown. Note that high sediment availability is not only found at locations where the suspended sediment concentrations are high, but also where tidal velocities are small (such as in the tributary).

3

(a)

(b)

(c)
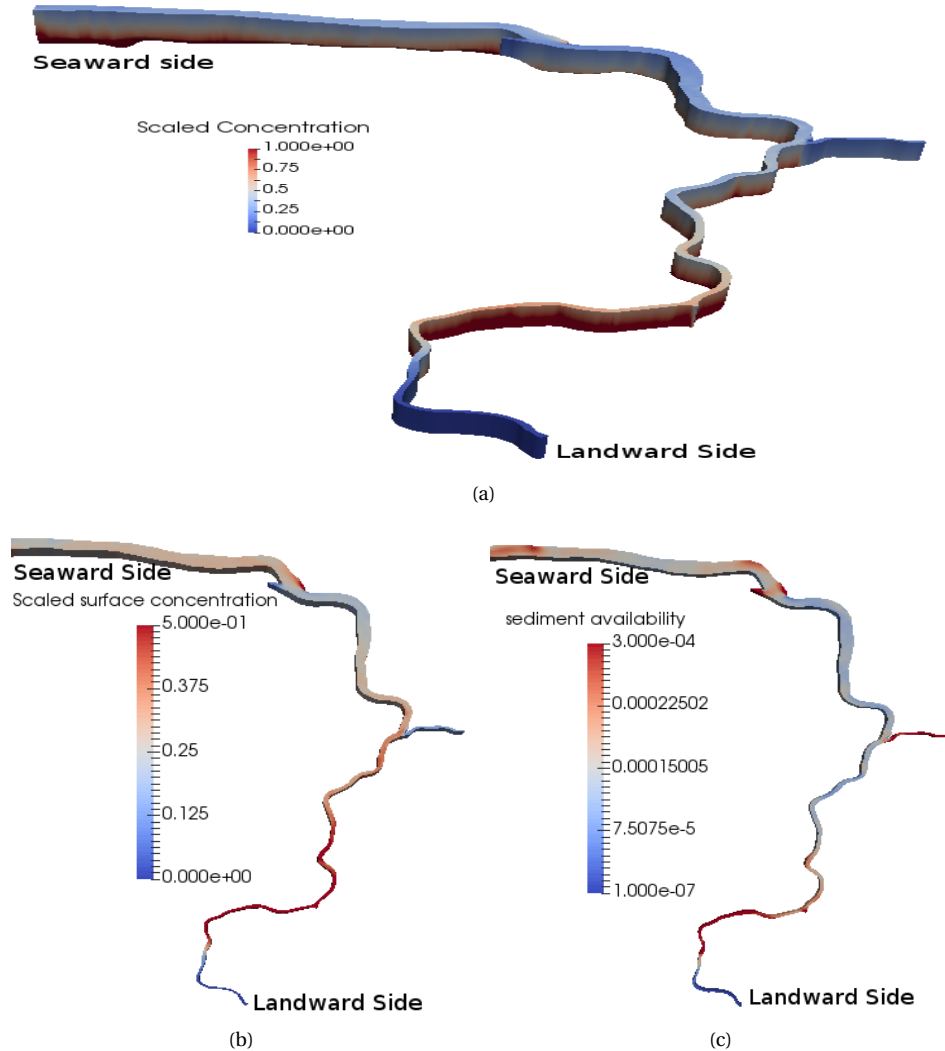
Figure 3.9: The scaled three–dimensional suspended sediment concentration (a), surface concentration (b) and sediment availability (c) for the Ems estuary.

3.10. CONCLUSIONS

A three-dimensional process-based semi-idealized model for estuarine turbidity maxima (ETM) in an estuary with arbitrary geometry and bathymetry has been developed. The water motion is driven by prescribed tidal forcing at the seaward side, and a river discharge at the river boundary. Furthermore, the horizontally varying, time- and depth-independent density field is prescribed (using, for example, observational data). The vertical eddy viscosity and diffusivity are assumed to be vertically constant and time-

independent. Horizontal viscous effects are neglected. The resulting three-dimensional equations for water motion and suspended sediment concentration are scaled using typical scales, appropriate for the system under consideration. The physical variables are expanded in the small parameter ϵ which is the ratio of the mean amplitude of the M_2 surface elevation and the mean water depth at the seaward boundary. This leads to a system of equations at each order of ϵ for the water motion and the suspended sediment concentration. Using rotating variables, the vertical profile of the velocity and the suspended sediment concentration can be obtained analytically in terms of the gradients of the surface elevation. To obtain the surface elevation at each order in ϵ, the continuity equation is integrated over the water column. This results in a two-dimensional elliptic partial differential equation for the surface elevation at that order. Using the concentrations and horizontal velocities, the horizontal sediment transport is calculated. The sediment still depends on the unknown sediment availability. By requiring the condition of morphodynamic equilibrium, an elliptic equation for the unknown sediment availability is obtained. These elliptic equations for the sediment availability and the surface elevation are solved numerically using the finite element method. In choosing the order of elements used for each order, special care is taken that the convergence rate of the numerical scheme used to calculate the sediment availability is at least of order one.

To test the model, we applied it to the Ems estuary with parameter values representative for years 1980 and 2005. The width is assumed to be exponentially convergent. The bathymetry in the longitudinal direction is taken from measurements and is approximated with a polynomial of degree four. In the first experiment, the bathymery is assumed to be uniform in the lateral direction. Focusing on the year 1980, the estuarine turbidity maximum (ETM) is found close to the seaward side. For the year 2005, the ETM is found far into the freshwater zone, approximately 38 km away from the entrance. This behaviour has been observed as well, indicating that the three-dimensional model is able to qualitatively reproduce the observed ETM behavior in the Ems estuary. As a first indication of the importance of the lateral variations, the bed profile in the lateral direction is varied parabolically. For both 1980 and 2005 cases, the location of ETM remains approximately the same. However, the highest concentration is found in the middle of the channel even though most of the easily erodible sediment is found at the sides. This clearly demonstrates the importance of using a 3D model to compare the influence of lateral dynamics on the longitudinal processes. In this chapter, we have mainly focused on the mathematical method used in the development of the model. In a forthcoming paper, the influence of bathymetric changes on each transport component will be discussed in detail, extending the sensitivity study of Schuttelaars *et al.* [8] by including lateral depth variations. The idealized model developed in this chapter is specifically aimed at studying estuaries in morphodynamic equilibrium, i.e., estuaries in which there are no convergences or divergences of sediment transport. To accommodate for the possibility of either a tidally-averaged import or export of sediment (due to, for example, the spring-neap cycle or human interventions), the condition of morphodynamic equilibrium has to be relaxed by allowing the sediment availability to vary on the long time scale, a model extension that is currently under investigation.

REFERENCES

[1] D. A. Jay, S. A. Talke, A. Hudson, and M. Twardowski, *Developments in Sedimentology*, Vol. 68 (Elsevier B.V., 2015) pp. 49–109.

[2] H. Burchard, H. M. Schuttelaars, and D. K. Ralston, *Sediment Trapping in Estuaries,* Annual Review of Marine Science **10** (2018).

[3] S. A. Talke, H. E. De Swart, and V. N. De Jonge, *An idealized model and systematic process study of oxygen depletion in highly turbid estuaries,* Estuaries and Coasts **32**, 602 (2009).

[4] V. N. De Jonge, H. M. Schuttelaars, J. E. E. Van Beusekom, S. A. Talke, and H. E. De Swart, *The influence of channel deepening on estuarine turbidity levels and dynamics, as exemplified by the Ems estuary,* Estuarine, Coastal and Shelf Science **139**, 46 (2014).

[5] A. B. Murray, *Contrasting the goals, strategies, and predictions associated with simplified numerical models and detailed simulations,* Prediction in geomorphology , 1 (2003).

[6] H. Weilbeer, *Numerical simulation and analyses of sediment transport processes in the Ems-Dollard estuary with a three-dimensional model,* Sediment and Ecohydraulics: INTERCOH 200 **30**, 447 (2008).

[7] D. Van Maren, T. Van Kessel, K. Cronin, and L. Sittoni, *The impact of channel deepening and dredging on estuarine sediment concentration,* Continental Shelf Research **95**, 1 (2015).

[8] H. M. Schuttelaars, V. N. De Jonge, and A. S. Chernetsky, *Improving the predictive power when modelling physical effects of human interventions in estuarine systems,* Ocean and Coastal Management **79**, 70 (2013).

[9] K. M. H. Huijts, H. M. Schuttelaars, H. E. De Swart, and A. Valle-Levinson, *Lateral entrapment of sediment in tidal estuaries: An idealized model study,* Journal of Geophysical Research **111**, C12016 (2006).

[10] S. A. Talke, H. E. De Swart, and H. M. Schuttelaars, *Feedback between residual circulations and sediment distribution in highly turbid estuaries: An analytical model,* Continental Shelf Research **29**, 119 (2009).

[11] A. S. Chernetsky, H. M. Schuttelaars, and S. A. Talke, *The effect of tidal asymmetry and temporal settling lag on sediment trapping in tidal estuaries,* Ocean Dynamics **60**, 1219 (2010).

[12] W. R. Geyer, R. P. Signell, and G. C. Kineke, *Lateral trapping of sediment in a partially mixed,* in *Physics of Estuaries and Coastal Seas*, edited by J. Dronkers and M. Scheffers, PECS 96 (Balkema, 1998) pp. 155–124.

[13] Y. H. Kim and G. Voulgaris, *Lateral circulation and suspended sediment transport in a curved estuarine channel: Winyah Bay, SC, USA,* Journal of Geophysical Research: Oceans **113**, 1 (2008).

[14] C. D. Winant, *Three-Dimensional Tidal Flow in an Elongated, Rotating Basin,* Journal of Physical Oceanography **37**, 2345 (2007).

[15] C. D. Winant, *Three-Dimensional Residual Tidal Circulation in an Elongated, Rotating Basin,* Journal of Physical Oceanography **38**, 1278 (2008).

[16] E. Ensing, H. E. De Swart, and H. M. Schuttelaars, *Sensitivity of tidal motion in well-mixed estuaries to cross-sectional shape, deepening, and sea level rise,* Ocean Dynamics , 933 (2015).

[17] M. Kumar, H. M. Schuttelaars, P. C. Roos, and M. Möller, *Three-dimensional semi-idealized model for tidal motion in tidal estuaries: An application to the Ems estuary,* Ocean Dynamics **66**, 99 (2016).

[18] B. Cushman-Roisin and J.-M. Beckers, *Introduction to geophysical fluid dynamics* (Academic Press, 2011).

[19] C. B. Vreugdenhil, *Numerical Methods for Shallow-Water Flow* (Springer Netherlands, 1994).

[20] J. T. F. Zimmerman, *On the Lorentz linearization of a nonlinearly damped tidal Helmholtz oscillator,* Proceedings of the Koninklijke Nederlandse Akademi **95**, 127 (1992).

[21] G. P. Schramkowski, H. M. Schuttelaars, and H. E. De Swart, *The effect of geometry and bottom friction on local bed forms in a tidal embayment,* Continental Shelf Research **22**, 1821 (2002).

[22] C. T. Friedrichs, B. D. Armbrust, and H. E. De Swart, *Hydrodynamics and equilibrium sediment dynamics of shallow, funnel shaped tidal estuaries,* In: Dronkers J, Scheffers MBAM (eds) Physics of Estuaries and Coastal Seas , 315 (1998).

[23] L. C. Van Rijn, *Principles of sediment transport in rivers, estuaries and coastal seas,* Aqua Publications , 690 (1993).

[24] A. H. Nayfeh, *Perturbation Methods*, edited by A. H. Nayfeh (Wiley-VCH, Weinheim, Germany, 2000).

[25] R. Soulsby, *Elsevier Oceanography Series,* Elsevier Oceanography Series, Vol. 35 (Elsevier, 1983) pp. 189–266.

[26] A. J. Souza, *On the use of the Stokes number to explain frictional tidal dynamics and water column structure in shelf seas,* Ocean Science **9**, 391 (2013).

[27] M. S. Gockenbach, *Understanding and Implementing the Finite Element Method* (Society of Industrial and Applied Mathematics (SIAM), Philadelphia, 2006).

3

[28] C. T. Friedrichs and J. M. Hamrick, *Effects of channel geometry on cross sectional variations in along channel velocity in partially stratified estuaries,* Buoyancy effects on coastal and estuarine dynamics **53**, 283 (1996).

3

4

INFLUENCE OF BATHYMETRIC CHANGES ON DYNAMICS OF ESTUARINE TURBIDITY MAXIMA

4.1. INTRODUCTION

An estuarine turbidity maximum (ETM) is a location in an estuary where the sediment concentration is higher than the concentrations on both the landward and seaward sides (Festa and Hansen [1]). ETMs have been observed in many estuaries around the world, e.g., Columbia River (USA), Kennebec (USA), Severn (UK), Tamar (UK), Ems (Netherlands), Gironde (France) and Mandovi (India). An estuary may have more than one ETM, examples of such estuaries are Columbia River (Jay and Musiak [2]), and Ems (De Jonge *et al.* [3]).

The occurrence of ETMs can have important consequences from both a commercial and ecological point of view (Ganju and Schoellhamer [4]). In these regions, the local deposition of sediments is often increased. If this turbidity zone is located near a navigation channel, extensive dredging is often required to keep the navigation channel at depth. Concerning ecological consequences, Peterson and Festa [5] showed that phytoplankton biomass and productivity are highly influenced by the suspended particle matter (SPM) concentration. Peterson and Festa [5] also suggested that phytoplankton productivity reduces drastically as SPM concentration increases from 10 to 100 mg l^{-1}.

Various process-based models have been developed to understand the influence of anthropogenic interventions on ETM dynamics, either in the longitudinal or in the lateral direction. Focusing on the class of idealized models (see Chapter 1), Chernetsky *et al.* [6] developed a two-dimensional width-averaged model for the water motion and sediment dynamics together with the use of the condition of morphodynamic equilibrium, focusing on the trapping mechanisms in the longitudinal direction. It was found that changes in the geometrical properties and/or external forcing conditions influence the location of the ETM (De Jonge *et al.* [3], Schuttelaars *et al.* [7]). Huijts *et al.* [8] focused

on the trapping mechanisms of the fine sediments in the lateral direction. The authors studied the impact of tidal forcing and water depth on the lateral patterns of the fine sediments. It was found that the residual lateral velocities resulting from cross-channel density gradients were strongly affecting the location of trapping of fine sediments in the cross section. The work of Huijts *et al.* [8] on lateral trapping of fine sediments has been extended by Chen and Sanford [9], Chen *et al.* [10], Schramkowski *et al.* [11], Huijts *et al.* [12] and Yang *et al.* [13].

Geyer *et al.* [14] and Kim and Voulgaris [15] showed that the lateral structure of these velocities and the lateral velocities themselves, together with the lateral variations of suspended sediment concentrations can significantly impact the processes in the longitudinal direction. This suggests that it is not enough to study the longitudinal and lateral processes in isolation, thus requiring the use of a three-dimensional model for the water motion and sediment dynamics. The development of such a model has been presented in Chapters 2 and 3.

The goal of this chapter is to understand the influence of anthropogenic and natural changes on the dynamics of estuarine turbidity maxima using the three-dimensional model developed in this thesis. In this chapter, both anthropogenic and natural changes are mimicked by the changes in the bathymetric profile for a prescribed density profile. To systematically investigate these influences, we first study the physical mechanisms and the trapping location for an estuary that has a longitudinally varying and laterally symmetrical bathymetric profile. Next, the sensitivity of the trapping location to asymmetries in the lateral bathymetry is systematically investigated. The effects of channel deepening and infilling on the ETM dynamics are studied by increasing or decreasing the maximum depth of the channel. To inspect the effects of sea level rise on the trapping mechanisms and locations, the overall depth of the estuarine system is increased.

The structure of this chapter is as follows: A brief introduction about the set up of the model including the details concerning governing equations is presented in section 4.2. In section 4.3, details about the experiments being performed in this chapter are discussed. The results of each of these experiments are discussed and compared in section 4.4. Finally, the conclusions are presented in section 4.6.

4.2. MODEL DESCRIPTION

4.2.1. GEOMETRY

A funnel shaped estuary with length L and width $2B_0$ at the entrance is considered (Fig. 4.1). The along-channel coordinate x varies from $x = 0$ at the seaward side to $x = L$ at the river side. The lateral coordinate y varies from $y = -B(x)$ at the lower boundary to $y = B(x)$ at the upper boundary with half-width of the estuary $B(x)$ given by

$$B(x) = B_0 e^{-x/L_b}. \tag{4.1}$$

Here L_b is the e-folding length scale, i.e., after moving over a distance of L_b in the landward direction, the width of the estuary is reduced by a factor e. The estuarine domain is denoted by Ω and the depth profile by $h(x, y)$.
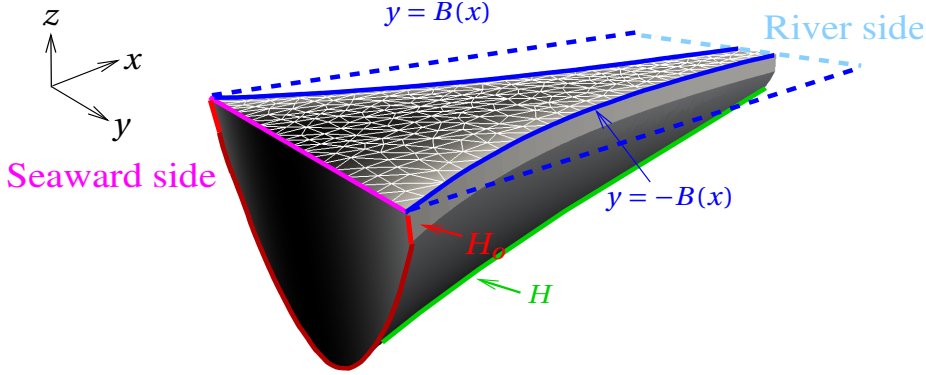
Figure 4.1: Sketch of funnel-shaped estuary used in this chapter. The half-width B (blue solid line) varies exponentially as $B(x) = B_0 e^{-x/L_b}$, with $2B_0$ the total width at the entrance (seaward side) and L_b the e-folding length. The green line denotes the longitudinal bed profile at $y = 0$ and the brown line, the lateral bed profile. A constant lateral depth H_0 (red line) is maintained at the sides ($y = \pm B$). Triangles at the surface visualize the triangulization of the surface which is used to compute the numerical solution.

4.2.2. GOVERNING EQUATIONS

In order to study the ETM dynamics, the equations for the water motion and suspended sediment concentration need to be solved. In Chapters 2 and 3, the details about the governing equations and the model development are explained. In these chapters, the details about the scaling analysis, perturbation analysis, decomposition of the physical variable in a residual component and various tidal constituents are also explained. In this section, only a brief overview is presented.

The water motion follows from the three-dimensional shallow water equations after using the Boussinesq approximation and the hydrostatic balance:

$$\frac{\partial u}{\partial x} + \frac{\partial v}{\partial y} + \frac{\partial w}{\partial z} = 0,$$

$$\frac{\partial u}{\partial t} + u\frac{\partial u}{\partial x} + v\frac{\partial u}{\partial y} + w\frac{\partial u}{\partial z} - fv = -g\frac{\partial \eta}{\partial x} - \frac{g}{\rho_0}\int_z^\eta \frac{\partial \rho}{\partial x}\mathrm{d}z' + \frac{\partial}{\partial z}(A_v\frac{\partial u}{\partial z}),$$

$$\frac{\partial v}{\partial t} + u\frac{\partial v}{\partial x} + v\frac{\partial v}{\partial y} + w\frac{\partial v}{\partial z} + fu = -g\frac{\partial \eta}{\partial y} - \frac{g}{\rho_0}\int_z^\eta \frac{\partial \rho}{\partial y}\mathrm{d}z' + \frac{\partial}{\partial z}(A_v\frac{\partial v}{\partial z}).$$

A Cartesian coordinate system is used, with x, y denoting the horizontal coordinates, and z the vertical coordinate, pointing in the upward direction. Here, $u(x, y, z, t)$, $v(x, y, z, t)$, and $w(x, y, z, t)$ denote the velocities in x, y and z directions, respectively, and $\eta(x, y, t)$ the free surface elevation. The dynamic density is denoted by ρ and the reference density by ρ_0. The eddy viscosity A_v, and the Coriolis parameter f, are assumed to be functions of horizontal coordinates x and y only.

At the seaward side, the system is forced by a prescribed surface elevation that consists of a combination of M_2 and M_4 tidal constituents,

$$\eta = A_{M_2}\cos(\omega t - \phi_{M_2}) + A_{M_4}\cos(2\omega t - \phi_{M_4}), \quad \text{for all } (x, y) \text{ in } \partial_S\Omega, \qquad (4.3)$$

where $A_{M_2}(x, y)$ and $A_{M_4}(x, y)$ are the (possibly) spatially varying amplitudes of the surface elevation of the M_2 and M_4 tidal constituents at the seaward boundary $\partial_S \Omega$. The phases of the M_2 and M_4 tides at the seaward side are denoted by $\phi_{M_2}(x, y)$ and $\phi_{M_4}(x, y)$, respectively and may depend on the horizontal coordinates as well. The parameter $\omega = 2\pi / T$ denotes the angular frequency of the M_2 tide with period $T = 12.42$ hrs.

At the free surface $z = \eta$, kinematic and dynamic boundary conditions are imposed,

$$w = \frac{\partial \eta}{\partial t} + u \frac{\partial \eta}{\partial x} + v \frac{\partial \eta}{\partial y}, \quad \text{at } z = \eta, \tag{4.4}$$

$$A_{\mathrm{v}} \frac{\partial \boldsymbol{u}_{\mathrm{h}}}{\partial z} = \boldsymbol{0}_{\mathrm{h}}, \qquad \text{at } z = \eta, \tag{4.5}$$

where $\boldsymbol{u}_{\mathrm{h}} = (u, v)$ denotes the horizontal velocity and $\boldsymbol{0}_{\mathrm{h}} = (0, 0)$, the two-dimensional horizontal null vector. At the bottom $z = -h$, the non-permeability condition (kinematic) and the dynamic boundary condition are prescribed,

$$w = -u \frac{\partial h}{\partial x} - v \frac{\partial h}{\partial y}, \quad \text{at } z = -h, \tag{4.6}$$

$$A_{\mathrm{v}} \frac{\partial \boldsymbol{u}_{\mathrm{h}}}{\partial z} = \frac{\boldsymbol{\tau}_b}{\rho_0} = s \boldsymbol{u}_{\mathrm{h}}, \quad \text{at } z = -h, \tag{4.7}$$

where $s(x, y)$ is the so-called stress parameter which follows from the linearization of the bed shear stress ($\boldsymbol{\tau}_b$) (see Zimmerman [16]). Following Chernetsky *et al.* [6], the physical parameters such as the vertical eddy viscosity A_{v} and the stress parameter s are assumed to vary with the local depth as

$$(A_{\mathrm{v}}, s) = (A_{\mathrm{v}0}, s_0) \frac{h}{H}. \tag{4.8}$$

Here $A_{\mathrm{v}0}$ and s_0 are the reference eddy viscosity and bottom stress, respectively, and H is the mean depth at the seaward side. At the river side ($x = L$), a constant river discharge Q is prescribed.

The suspended sediment concentration, denoted by c, follows from a three-dimensional advection-diffusion equation,

$$\frac{\partial c}{\partial t} + \frac{\partial}{\partial x} \left(cu - K_{\mathrm{h}} \frac{\partial c}{\partial x} \right) + \frac{\partial}{\partial y} \left(cv - K_{\mathrm{h}} \frac{\partial c}{\partial y} \right) + \frac{\partial}{\partial z} \left(c(w - w_{\mathrm{s}}) - K_{\mathrm{v}} \frac{\partial c}{\partial z} \right) = 0, \tag{4.9}$$

where $K_{\mathrm{h}}(x, y)$ and $K_{\mathrm{v}}(x, y)$ are the horizontal and vertical eddy diffusivities, and w_s is the settling velocity. At the surface, settling and diffusive fluxes balance each other. At the bottom, the sum of the settling and diffusive fluxes equals a specified erosion-deposition flux of volume concentration.

We consider the system to be in morphodynamic equilibrium, i.e.,

$$\langle D - E \rangle = 0, \tag{4.10}$$

where D denotes the sediment deposition, E, the erosion flux from the bed and $\langle \cdot \rangle$, a tidally-averaged quantity. A morphodynamic equilibrium can only be found by requiring

a specific spatial distribution of easily erodible sediment in the estuary. This sediment availability is denoted by $a(x, y)$, a dimensionless quantity.

Using scaling and perturbation analyses, the equations for the water motion and suspended sediment concentration can be approximated by linear systems of equations in various orders of a small parameter ϵ which is the ratio of the mean M_2 surface elevation and the mean depth at the seaward side. The leading-order (ϵ^0) and first-order (ϵ^1) system of equations for the water motion and suspended sediment concentration have to be solved to obtain the leading order condition of morphodynamic equilibrium. This results in the following condition for the sediment availability $a(x, y)$:

$$\nabla \cdot (\mathbf{D}^a \nabla a + a\mathbf{T}) = 0, \tag{4.11a}$$

with

$$\mathbf{D}^a = \begin{pmatrix} D_{K_h} + T_{M_2}^{xa_x} & T_{M_2}^{xa_y} \\ T_{M_2}^{ya_x} & D_{K_h} + T_{M_2}^{ya_y} \end{pmatrix}, \quad \text{and} \quad \mathbf{T} = \begin{pmatrix} T^{xa} \\ T^{ya} \end{pmatrix}.$$

Here, D_{K_h} is the transport contribution due to the horizontal diffusivity and the contributions $T_{M_2}^{xa_x}$, $T_{M_2}^{xa_y}$, $T_{M_2}^{ya_x}$, and $T_{M_2}^{ya_y}$ in $\mathbf{D}^a$ are transports generated by the covariance of the M_2 velocity and M_2 concentration due to advective processes. Note that these transport terms are proportional to a_x and a_y.

The terms T^{xa} and T^{ya} denote the leading-order tidally averaged sediment transport contributions in the x and y directions, respectively, that are proportional to a. These transport contributions can be further decomposed in sub-contributions, resulting from different physical processes. The transport T^{xa} can be decomposed as (see previous chapter for details)

$$T^{xa} = T_{M_0}^{xa} + T_{M_2}^{xa} + T_{M_4}^{xa} + T_{\text{surface}}^{xa} + T_{\text{diff}}^{xa}. \tag{4.11b}$$

Here, $T_{M_0}^{xa}$ denotes the transport due to the interaction of the M_0 velocity and M_0 concentration. In turn, the M_0 velocity itself consists of various contributions and therefore each of these contributions to $T_{M_0}^{xa}$ can be computed separately (see Table 4.1 for a complete list of all subcomponents). Similarly, $T_{M_2}^{xa}$ is the transport due to the correlation between the M_2 velocity and M_2 concentration. The M_2 concentration consists of various contributions and each of these contributions to $T_{M_2}^{xa}$ can be computed separately. Similarly, $T_{M_4}^{xa}$ is generated by the interaction of M_4 velocity and M_4 concentration. The M_4 velocity is a sum of various components as listed in Table 4.1 which allows us to decompose it into further subcomponents. The component T_{surface}^{xa} is the transport due to the interaction of M_2 surface elevation, M_2 velocity and the leading-order concentration at the surface and T_{diff}^{xa} is the diffusive transport contribution. A similar decomposition can be made for the transport T^{ya} in the y-direction.

4.2.3. NUMERICAL SOLUTION
To ensure the accuracy of the model, the funnel shaped domain is discretized using approximately 100,000 grid points at the surface (see sketch in Fig. 4.1) . Since the model is analytical in the vertical direction, no discretization in the vertical direction is needed. Cubic polynomial functions are used as basis functions for the leading-order water motion. The so-called DD-method is used to compute both the first- and second-order partial derivatives of the leading-order surface elevation. In this DD-method (see chapter 2),

4. INFLUENCE OF BATHYMETRIC CHANGES ON DYNAMICS OF ESTUARINE TURBIDITY

4

Velocity		Concentration		Transport
		$T_{M_0}^{xa}$		
u^{10}	u_{GC}^{10}	$\tilde{c}^{00}$		$T_{M_0,GC}^{xa}$
	u_{RD}^{10}			$T_{M_0,RD}^{xa}$
	u_{AC}^{10}			$T_{M_0,AC}^{xa}$
	u_{NS}^{10}			$T_{M_0,NS}^{xa}$
	u_{TRF}^{10}			$T_{M_0,TRF}^{xa}$
		$T_{M_2}^{xa}$		
u^{02}		$\tilde{c}_{AC}^{12}$		$T_{M_2,AC}^{xa}$
		$\tilde{c}_{S}^{12}$		$T_{M_2,S}^{xa}$
		$\tilde{c}_{BS}^{12}$	$\tilde{c}_{BS,GC}^{12}$	$T_{M_2,BS,GC}^{xa}$
			$\tilde{c}_{BS,RD}^{12}$	$T_{M_2,BS,RD}^{xa}$
			$\tilde{c}_{BS,AC10}^{12}$	$T_{M_2,BS,AC10}^{xa}$
			$\tilde{c}_{BS,NS10}^{12}$	$T_{M_2,BS,NS10}^{xa}$
			$\tilde{c}_{BS,TRF10}^{12}$	$T_{M_2,BS,TRF10}^{xa}$
			$\tilde{c}_{BS,EF}^{12}$	$T_{M_2,BS,EF}^{xa}$
			$\tilde{c}_{BS,AC14}^{12}$	$T_{M_2,BS,AC14}^{xa}$
			$\tilde{c}_{BS,NS14}^{12}$	$T_{M_2,BS,NS14}^{xa}$
			$\tilde{c}_{BS,TRF14}^{12}$	$T_{M_2,BS,TRF14}^{xa}$
		$T_{M_4}^{xa}$		
u^{14}	u_{EF}^{14}	$\tilde{c}^{04}$		$T_{M_4,EF}^{xa}$
	u_{AC}^{14}			$T_{M_4,AC}^{xa}$
	u_{NS}^{14}			$T_{M_4,NS}^{xa}$
	u_{TRF}^{14}			$T_{M_4,TRF}^{xa}$

Table 4.1: Decomposition of various transport terms $T_{M_0}^{xa}$, $T_{M_2}^{xa}$, and $T_{M_4}^{xa}$ into subcomponents. A similar decomposition can be made for the transport terms in the lateral direction.

the partial derivatives are obtained by taking the partial derivatives of the numerical approximation (see chapter 2 for more details). Quadratic polynomial functions are used to solve for the first-order water motion and the sediment availability. This ensures that all the physical variables, i.e., water motion, suspended sediment concentration and sediment availability give converging results. For detailed information, see Chapters 2 and 3.

4.3. NUMERICAL EXPERIMENTS

4.3.1. GENERAL INFORMATION

For all the experiments in this chapter, physical parameters characteristic for the Ems estuary in 2005 are used (Table 4.2). A realistic value of the Coriolis parameter $f = 1.34 \times 10^{-4}$ s^{-1}, corresponding to the Ems estuary, is taken. To determine the reference

Parameter	Value
L	63.7 km
L_b	30 km
B_0	335 m
g	9.8 m s^{-2}
ω	1.4×10^{-4} s^{-1}
f	1.34×10^{-4} s^{-1}
ρ_0	1020 kg m^{-3}
ρ_s	2650 kg m^{-3}
β	7.6 × 10^{-4} psu^{-1}
A_{M_2}	1.35 m
A_{M_4}	0.19 m
ϕ	-174.6°
A_v	0.0135 m^2 s^{-1}
s	0.0108 m s^{-1}
Q	80 m^3 s^{-1}
w_s	1.0 ×10^{-3} m s^{-1}
K_h	100 m^2 s^{-1}

Table 4.2: Parameters corresponding to the 2005 case of the Ems estuary.

stress parameter (s_0) and the eddy viscosity (A_{v0}) in Eq. (4.8), the model is calibrated using observed amplitude and phase of the M_2 tide for the Ems estuary. For calibration, the symmetric bed profile, defined in the next section, is used. To be consistent with the observations of the suspended sediment concentrations in the Ems estuary, the sediment availability a is scaled in such a way that the maximum concentration at the surface becomes 1000 mg l^{-1} for the reference experiment (see section 4.4). For the remaining cases in this chapter, the same scaling factor is used. This means that the maximum sediment concentration at the surface in the remaining cases need not be 1000 mg l^{-1}. However, the total amount of easily erodible sediment in the estuary remains unchanged in all cases considered in this chapter.

4.3.2. BATHYMETRY

Following Chernetsky *et al.* [6], the longitudinal bed profile $H_{max}(x)$ is obtained by approximating the along-channel bed profile of the Ems estuary with a fourth degree polynomial. The lateral variations in the bed profile are prescribed by a Gaussian profile (Ensing *et al.* [17]), given by

$$h = H_{max}(x) \exp(-CY^2), \tag{4.12}$$

where $C(x) = \log(H_{\max}(x)/H_0)$ is the steepness parameter and $H_{\max}(x)$ is the along chan-nel bed profile discussed above. H_0 is a fixed depth, prescribed at the lateral sides $y = \pm B$ (Fig. 4.1) and $Y(x, y)$ is defined as

$$Y(x, y) = \frac{1 - \sqrt{1 + \psi^2 - 2\psi y/B(x)}}{\psi}, \tag{4.13}$$

with ψ, the skewness parameter that varies between -1 and 1.

(a)   (b)
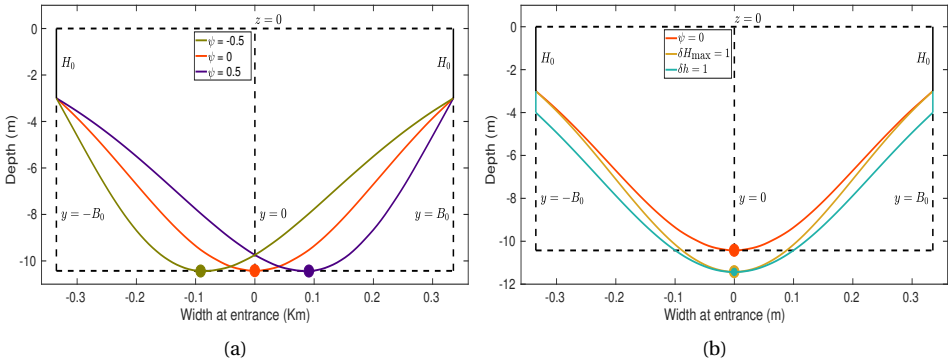
Figure 4.2: Bed profile in the lateral direction at the entrance (seaward side) when viewed from the river side to the seaward side. The *left panel* (Fig. a) shows the influence of ψ on symmetricity of the bed profile with $\delta h = 0$ and $\delta H_{\max} = 0$. For $\psi = 0$, the bed profile is symmetric around the middle axis $y = 0$, for $\psi = -0.5$, skewed to the left and for $\psi = 0.5$, skewed to the right of the middle axis. The *right panel* (Fig. b) shows symmetric lateral bed profiles with $\psi = 0$ at the entrance when the maximum depth $H_{\max}$ of the channel is increased by one meter ($\delta H_{\max} = 1$) and when the overall depth h is increased by one meter ($\delta h = 1$). The filled colored circles indicate the location of maximum depth.

Varying the skewness parameter ψ changes the skewness of the lateral bed profile. For $\psi = 0$, a perfectly symmetric bed profile in the lateral direction is obtained (Fig. 4.2(a)). For $\psi < 0$, when viewed from the river side to the seaward side, the lateral bed profile is skewed to the left relative to the middle axis $y = 0$, and for $\psi > 0$, skewed to the right (Fig. 4.2(a)). Figure 4.2(a) shows that changing the value of ψ does not alter the magnitude of maximum depth, only the location changes.

Furthermore, adding a small perturbation δh to the depth h changes the overall depth of the estuary, whereas adding a small perturbation $\delta H_{\max}$ to the maximum depth $H_{\max}$ only changes the maximum depth without influencing the lateral depths at $y = \pm B$. Figure 4.2(b) shows the lateral bed profile for symmetric case ($\psi = 0$) when the maxi-mum depth $H_{\max}$, attained at the middle of the channel, is increased by one meter, i.e., $\delta H_{\max} = 1$, while keeping the lateral depths H_0 unchanged and when the overall depth h is increased by one meter, i.e., $\delta h = 1$. The filled circles in Fig. 4.2(b) show that changing the maximum depth or overall depth of the channel does not affect the location of the maximum depth, only the magnitude changes. Note that, unless stated otherwise, the default value of parameters ψ, δh and $\delta H_{\max}$ are zero.

4.4. RESULTS

In this section, results regarding the dynamics of the estuarine turbidity maximum for different lateral depth profiles are presented. In the first experiment, a laterally symmetric bed profile is considered. We will refer to this case as the *reference case*. In section 4.4.2, the influence of laterally asymmetric bed profiles, which are obtained by varying the values of ψ (see Fig. 4.2(a)), on the ETM dynamics is systematically investigated. In section 4.4.3, the influence of channel shallowing (deepening) on the ETM characteristics is studied. This is modelled by decreasing (increasing) the maximum depth $H_{\max}$ of the channel (see Fig. 4.2(b)). Finally, we look at the influence of sea level rise and fall on the sediment dynamics in section 4.4.4. To model this phenomenon, the overall depth of the estuarine system h is increased and decreased (see Fig. 4.2(b)).

4.4.1. LATERALLY SYMMETRIC BED PROFILE

In the *reference experiment*, we consider a laterally symmetric bed profile using the default parameters as given in Table 4.2. The symmetric bed profile is obtained by taking
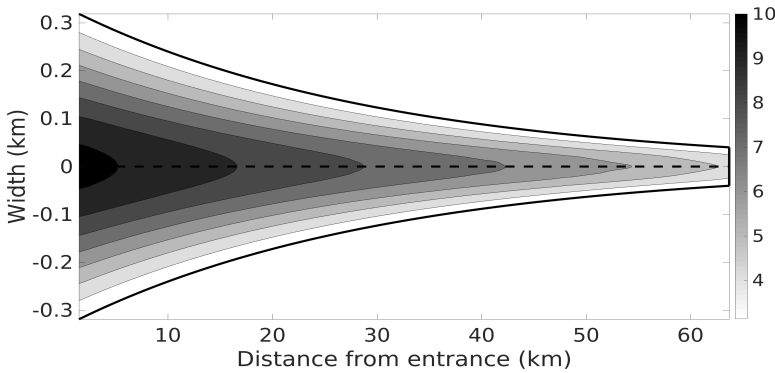
Figure 4.3: The bathymetric profile for the *reference case*. The dashed line passes through the middle of the channel. The solid lines on the sides indicate the boundaries of the estuary. For each transect in the y-direction, the maximum depth is attained at the middle of the channel. A constant minimum depth of 3 m is maintained at the shallow sides.

$\psi = 0$ in Eq. (4.12). The minimum water depth at the shoals, denoted by H_0, is taken to be 3 m. For the symmetric bed profile, the maximum depth along any transect in the y-direction is found in the middle of the channel, i.e., along $y = 0$. The maximum depth $H_{\max}$ of approximately 10 m is attained at the middle of the channel entrance.

   Figure 4.4 shows the distribution of fine sediments at the bottom (left panel) and suspended sediment concentration at the surface (right panel) for the reference case. From Fig. 4.4(a), it follows that the maximum amount of fine sediments is found towards the end (approximately 46 km from the entrance) of the estuary. The amount of fine sediments is higher at the shallow sides than in the middle of the channel. The distribution of fine sediments at the bottom is not symmetric about the middle axis ($y = 0$) of the channel due to the Coriolis effect. Furthermore, the availability of fine sediments becomes almost negligible near the landward end of the channel.

(a) Sed. availability

(b) SSC at surface (mg l^{-1})
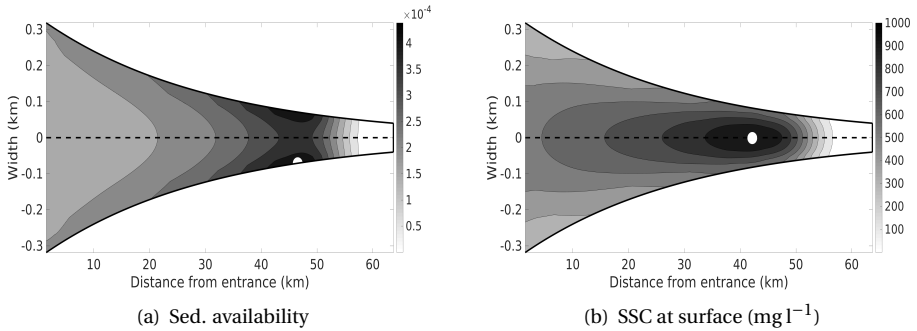
Figure 4.4: Sediment availability (*left-panel*) and suspended sediment concentration at the surface (*right-panel*) for the reference case. Note that sediment availability a is scaled in such a way that the maximum suspended sediment concentration at the surface for the reference case becomes 1000 mg l^{-1}. The white circle denotes the location of maximum quantity being plotted. The units for suspended sediment concentration is mg l^{-1}. The sediment availability is a dimensionless quantity and therefore no units are associated with the left colorbar.

The suspended sediment concentration at the surface is shown in Fig. 4.4(b). The location of maximum suspended sediment concentration at the surface is found approximately 42 km from the entrance with a maximum concentration at the surface of 1000 mg l^{-1}. Contrary to sediment availability, the maximum suspended sediment concentration at the surface is found almost in the middle of the channel. The maximum suspended sediment concentration at the surface is found more seaward than the location of maximum sediment availability. The suspended sediment concentration at the surface also becomes almost negligible towards the landward end of the channel.

Figure 4.5 shows the transport components $T_{M_0}^{xa}$, $T_{M_2}^{xa}$, $T_{M_4}^{xa}$ and T_{surface}^{xa} that are proportional to sediment availability a (see Eq. (4.11b)). Note that a positive sign of a transport component indicates transport in the landward direction and a negative sign, transport in the seaward direction. Figure 4.5 shows that the M_0 transport (top left panel) is seaward (negative) in most of the estuary. Also, the magnitude of positive M_0 transport in the estuary is smaller than the negative M_0 transport. The M_2 transport (top right panel) on the other hand is positive in most of the estuary, resulting in import of fine sediments. The M_4 transport is negative at the seaward side and positive at the landward side. The negative M_4 transport intrudes up to 36 km from the entrance. The magnitude of the M_4 transport component is smaller than the magnitude of the M_0 and M_2 transport components. The surface transport (T_{surface}^{xa}) as shown in the bottom right panel is positive throughout the estuary. Its magnitude is much smaller, compared to the magnitude of the other components. The longitudinal diffusive transport T_{diff}^{xa} is much weaker than the other components and hence not shown here.

Concerning the lateral transport T^{ya}, all components are negligible compared to the diffusive transport T_{diff}^{ya}. The magnitude of the lateral diffusive transport, shown in Fig. 4.6, suggests that the lateral diffusive transport is stronger than the longitudinal transport components (Fig. 4.5). The lateral diffusive transport is towards the left (looking seaward) in the lateral direction in the lower part and towards the right in the lateral
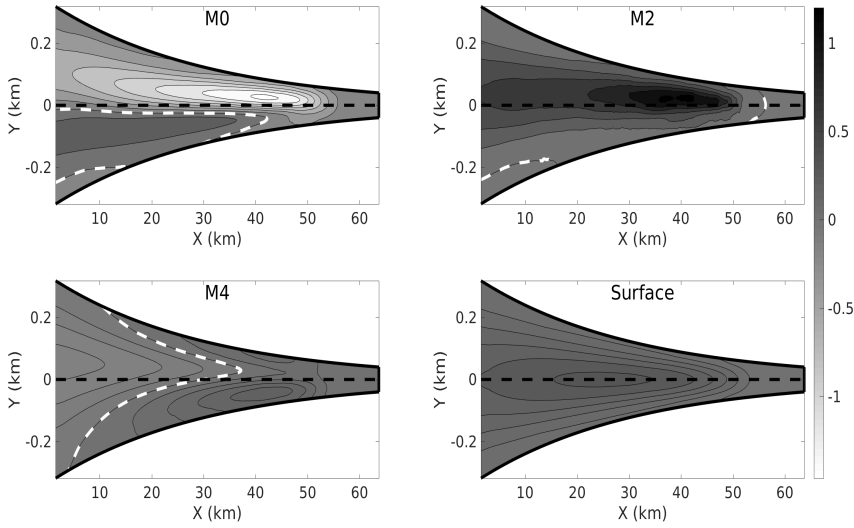
Figure 4.5: Longitudinal suspended sediment transport terms proportional to sediment availability a. *Top left panel* shows the M_0 transport, *top right panel* the M_2 transport, *bottom left panel* the M_4 transport and *bottom right panel* the surface transport. The black dashed line in the middle indicates the middle of the channel ($y = 0$) and the solid black lines at the sides the domain boundaries. The white dashed line indicates the zero contour of the transport component being plotted. No white dashed line for surface transport (bottom right) indicates a positive surface transport throughout the channel.
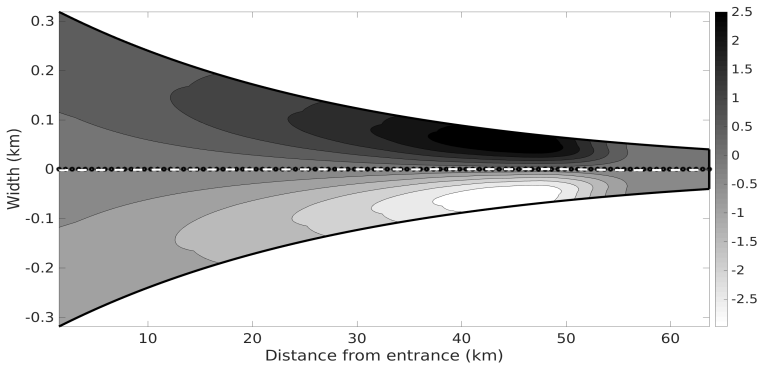
Figure 4.6: Lateral diffusive transport T_{diff}^{ya}. The black stars in the middle indicates the middle of the channel ($y = 0$) and the black solid lines at the sides, the domain boundaries. The white dashed line in the middle indicates the zero contour of the lateral diffusive transport. The white dashed line for the zero contour overlaps with the black stars in the middle indicating a clear partition between the negative transport in the lower part (below $y = 0$) and positive transport in the upper part (above $y = 0$) of the channel.

direction in the upper part of the estuary.

4.4.2. ASYMMETRIC BED PROFILE

In this section, the influence of a laterally asymmetric bed profile on the ETM dynamics is systematically investigated. The laterally asymmetric bed profile is obtained by taking non-zero values of ψ in Eq. (4.12). In this chapter, we will mainly focus on two values of $\psi = -0.5$ and $\psi = 0.5$. As mentioned in section 4.3.2, for $\psi = -0.5$, a laterally asymmetric
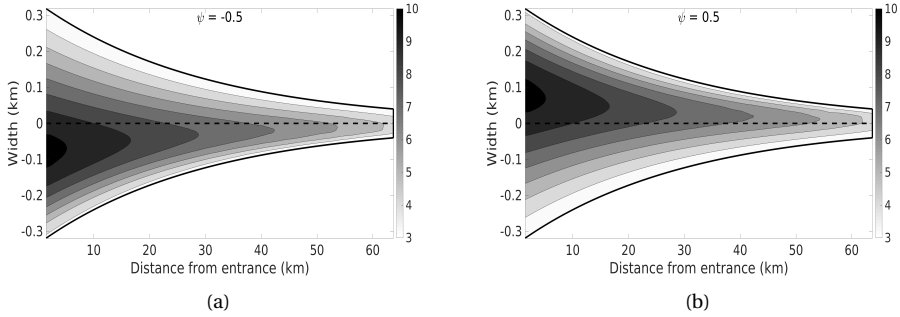
Figure 4.7: Laterally asymmetric bed profiles profiles for $\psi = -0.5$ (*left panel*) and $\psi = 0.5$ (*right panel*). For $\psi = -0.5$, the bed profile is skewed to the left when viewed from the river side to the seaward side and for $\psi = 0.5$, skewed to the right. The units in the colorbar are m.

bed profile skewed to the left (when viewed from the river side to the seaward side) is obtained (Fig. 4.7(a)). We refer to this profile as a negatively skewed bed profile. For $\psi = 0.5$, a similar bed profile but skewed to the right is obtained (Fig. 4.7(b)). This profile is referred to as positively skewed.

Figure 4.8 shows the availability of fine sediments (dimensionless) at the bottom for both asymmetric bed profiles. For the positively skewed bed profile (Fig. 4.8(b)), the
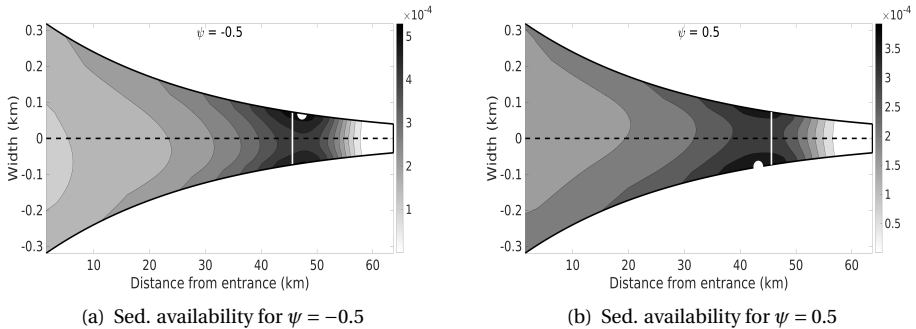
Figure 4.8: Sediment availability for positively skewed bed profile with $\psi = -0.5$ (*left panel*, a) and negatively skewed bed profile with $\psi = 0.5$ (*right panel*, b). The white circle denotes the location of maximum sediment availability. The white line denotes the x-location of the maximum sediment availability for the reference case with $\psi = 0$.

maximum sediment availability is found below the middle line through the estuary (y=0) and for negatively skewed profile (Fig. 4.8(a)) above the middle line.

Compared to the reference case, the distance of the maximum sediment availability to the seaward side is larger for the negative skewed bed profile and smaller for the positively skewed bed profile. Furthermore, the maximum sediment availability is higher for negatively skewed bed profile (approx. 5×10^{-4}) and smaller for positively skewed bed profile (approx. 4×10^{-4}) compared to the reference case (approx. 4.5×10^{-4}). Note that for both asymmetric bed profiles, the contour lines for sediment availability are also skewed, following the contour lines of the bathymetric profiles with maximum sediment availability found at the shallow sides.

Figure 4.9 shows the suspended sediment concentration at the surface for both bed profiles. Concerning the x-location, the ETM is less landward for the positively skewed

(a) SSC at surface for $\psi = -0.5$ (b) SSC at surface for $\psi = 0.5$
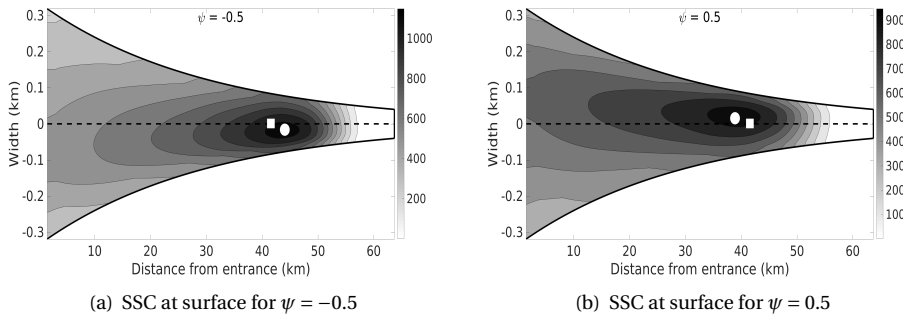
Figure 4.9: Suspended sediment concentration for negatively skewed bed profile with $\psi = -0.5$ (*left panel*, a) and positively skewed bed profile with $\psi = 0.5$ (*right panel*, b). The white circle denotes the location of maximum suspended sediment concentration at the surface. The white square shows the same for the reference case with $\psi = 0$. The units in the colorbar are mg l^{-1}.

bed profile (approx. 39 km from the entrance) and more landward for the negatively skewed bed profile (approx. 44 km from the entrance) compared to the reference case (approx. 42 km from the entrance). For the y-location, the ETM is skewed to the right of the middle axis for the positively skewed bed profile and skewed to the left for the negatively skewed bed profile when viewing from the river side to the seaward side. The ETM for the positively skewed bed profile has a maximum concentration of approx. 900 mg l^{-1} and is thus weaker than the ETM for the reference case (1000 mg l^{-1}). On the other hand, the ETM for the negatively skewed bed profile with a maximum concentration of 1100 mg l^{-1} is stronger than the ETM for the reference case (1000 mg l^{-1}).

Next, the smooth transition of the bed profile from negatively skewed ($\psi = -0.5$) to positively skewed ($\psi = 0.5$) is simulated by running the model for intermediate values of ψ. For each value of ψ, the location and the strength of the ETM is plotted. Figure 4.10(a) shows the distance of the ETM from the entrance for different values of the parameter ψ. Figure 4.10(a) suggests that the ETM consistently moves seaward for increasing values of ψ.

Concerning the y-location of the ETM, Fig.4.10(b) shows that increasing ψ, the ETM moves from the left to the right of the middle line $y = 0$ when looking into the seaward direction. The maximum concentration of the ETM, as shown in Fig. 4.10(c), becomes

(a) x-location of ETM   (b) y-location of ETM   (c) Maximum concentration at ETM
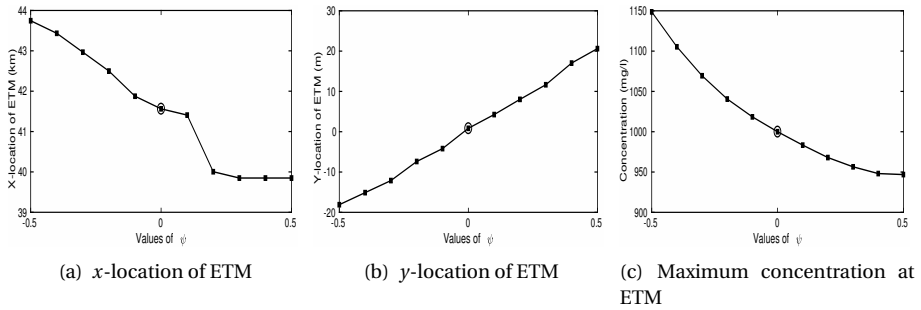
Figure 4.10: Location and strength of ETM for laterally asymmetric bed profiles for different values of ψ. The *top left panel* (a) shows the x-location or the distance of the ETM from the seaward side and the *top right panel* (b) the y-location of the ETM. The *bottom panel* (c) shows the strength of the ETM in terms of maximum suspended sediment concentration at the surface. In all the panels, solid black squares indicate the model results and the black circle indicates the data for the reference case.

lower for increasing values of ψ. In summary, when going from negatively skewed bed profiles to positively skewed ones, the ETM consistently moves seaward and from the left to right in lateral direction with decreasing maximum concentrations.

Next, we focus on the transport components for negatively and positively skewed bed profiles. Figure 4.11 shows individual longitudinal transport components as given by Eq. (4.11b) for both negatively and positively skewed bed profiles. For the sake of comparison, the scale of the colorbars in Figs. 4.11(a) and 4.11(b) are kept the same. Figure 4.11 suggests that the overall magnitude of the longitudinal sediment transport is higher in case of negatively skewed bed profile (Fig. 4.11(a)) and lower in case of positively skewed bed profile (Fig. 4.11(b)) when compared to the reference case (Fig. 4.5).

The following observations can be made from Fig.4.11:

M_0: Comparing the top left panels of Figs.4.11(b) and 4.11(a) shows that when moving from a positively skewed bed profile to a negatively skewed one, the intrusion of negative M_0 transport towards the landward side increases, and the location of maximum negative M_0 transport also moves towards the middle of the channel.

M_2: The top right panels of Figs. 4.11(b) and 4.11(a) show that the M_2 transport remains dominantly positive with increasing magnitude when going from positively skewed to negatively skewed bed profile. The location of the maximum M_2 transport also moves from the upper lateral boundary to the middle of the channel.

M_4: Concerning the M_4 transport, shown in the bottom left panels of Figs.4.11(b) and 4.11(a), the intrusion of negative M_4 transport increases with decreasing magnitude of the positive transport when going from positively skewed to negatively skewed bed profile.

Surface: The surface transport remains positive throughout the estuary for both cases but the magnitude decreases when going from a positively skewed to a negatively skewed bed profile.
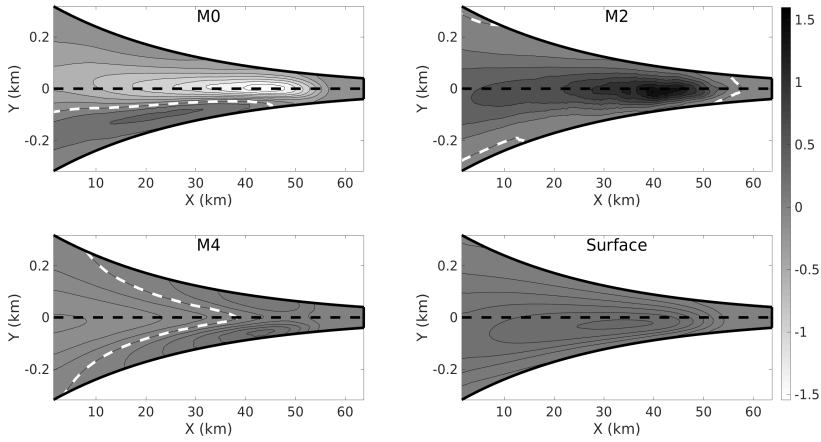
(a) Negatively skewed bed profile (ψ = -0.5)
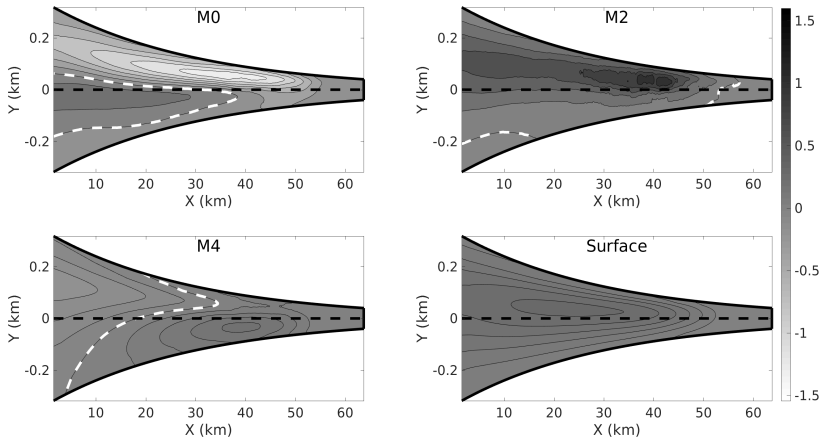
(b) Positively skewed bed profile (ψ = 0.5)

Figure 4.11: Longitudinal suspended sediment transport terms for negatively (*top figure*) and positively skewed (*bottom figure*) bed profiles. In each of these figures (top and bottom), *top right subpanel* shows the M_0 transport, *top right subpanel* the M_2 transport, *bottom left subpanel* the M_4 transport and *bottom right subpanel* the surface transport. The black dashed line indicates the middle of the channel and the black solid lines on the sides, the domain boundaries. The white dashed line indicates the zero contour of the transport component being plotted.

4.4.3. SHALLOWING AND DEEPENING OF CHANNEL

In this section, we systematically investigate the influence of shallowing (infilling) or deepening (dredging) of the estuarine channel on the sediment dynamics. It is assumed that the shallowing or deepening of the channel does not alter the symmetry of the bed

profile in the lateral direction. The lateral depths H_0 are kept unchanged as in the reference case, i.e., $H_0 = 3$ m.

(a) Channel shallowing by 1 m   (b) Channel deepening by 1 m
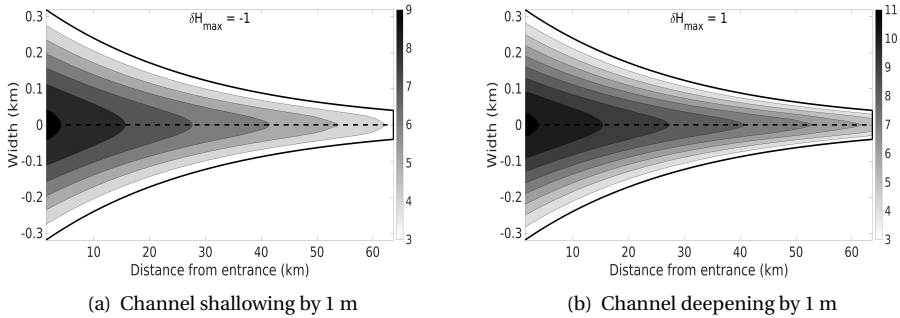
Figure 4.12: Bathymetric profiles for shallowing (*left panel*) and deepening (*right panel*) of the estuarine channel with $\psi = 0$. For channel shallowing, $\delta H_{max} = -1$ is used and for channel deepening, $\delta H_{max} = 1$. The units in the colorbar are m.

Changing the maximum depth $H_{max}(x)$ in Eq. (4.12) by a small overall perturbation δH_{max}, i.e., $H_{max}(x) \rightarrow H_{max}(x) + \delta H_{max}$, mimics the shallowing or deepening of the channel mainly occurring in the middle of the channel. A negative value of δH_{max} results in channel shallowing and a positive value in channel deepening. Here, we mainly focus on shallowing and deepening by 1 meter, i.e., $\delta H_{max} = -1$ m and 1 m as shown in Fig.4.12.

Figure 4.13 shows the availability of fine sediments (dimensionless) at the bottom for the shallowed and deepened channels. For the shallowed channel (Fig. 4.13(a)), the location of maximum sediment availability moves towards the seaward side.

(a) Sed. availability for $\delta H_{max} = -1$ (b) Sed. availability for $\delta H_{max} = 1$
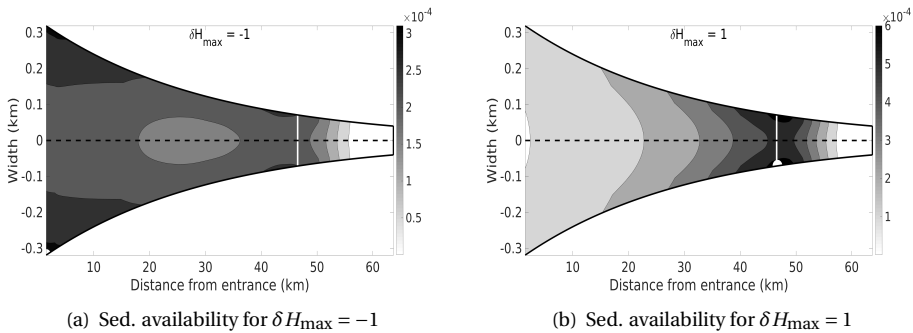
Figure 4.13: Availability of fine sediments at the bottom for shallowed (*left panel*) and deepened (*right panel*) channels. The white circle denotes the location of maximum sediment availability. The white solid line indicates the x-location of the sediment availability for the reference case. The sediment availability is a dimensionless quantity and hence no units are associated with the colorbar.

A large part of fine sediments is now available at the seaward side with reduced magnitude (approx. 3×10^{-4}) compared to the reference case (approx. 4.5×10^{-4}). For the

deepened channel (Fig. 4.13(b)), the location of maximum sediment availability remains close to that of the reference case. For this case, the sediment availability is also almost negligible up to 20 km from the seaward side and towards the landward side. Since the total amount of the fine sediments available for erosion is unchanged, this leads to a larger maximum of the sediment availability (approx. 6×10^{-4}) for the deepened channel compared to the reference case.

Figure 4.14 shows the suspended sediment concentration at the surface for both the shallowed and deepened channels. For the shallowed channel (Fig. 4.14(a)), the ETM

(a) SSC at surface for $\delta H_{\max} = -1$ (b) SSC at surface for $\delta H_{\max} = 1$
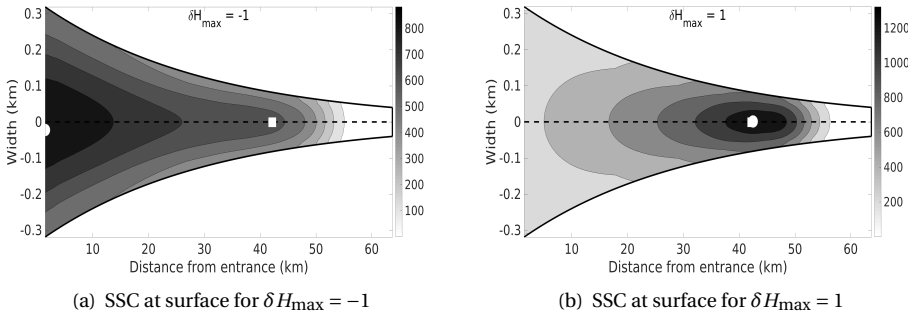
Figure 4.14: Suspended sediment concentration at the surface for shallowed (*left panel*, a) and deepened (*right panel*, b) channels. The white circle denotes the location of maximum suspended sediment concentration at the surface. The units in the colorbar are mg l^{-1}.

is found at the mouth of the channel below the middle line ($y = 0$) with a maximum concentration of approx. 850 mg l^{-1} compared to 1000 mg l^{-1} for the reference case. The suspended sediment concentration at the surface decreases in the landward direction. For the deepened channel (Fig. 4.14(b)), the location of the ETM remains unchanged but the strength of the ETM increases with a maximum concentration of approx. 1250 mg l^{-1}. The suspended sediment concentration at the surface in this case is small at the seaward side, increases up to the location of ETM and then decreases to the landward side.

Next, the influence of $\delta H_{\max}$ on the location and strength of ETM is systematically investigated. For this purpose, the model is run for various values of $\delta H_{\max}$ ranging between -1 m and 1 m. Figure 4.15(a) shows that with increasing values of $\delta H_{\max}$, i.e., from shallowing to deepening, the ETM moves landward. It is interesting to see that the ETM remains close to the seaward side for values of $\delta H_{\max}$ up to -0.8 m and then suddenly moves towards the landward end. Note that for all values of $\delta H_{\max}$, the ETM is either found at a fixed location close to the seaward side (for $\delta H_{\max} \leq -0.8$ m) or at a fixed location close to the landward side (for $\delta H_{\max} \geq -0.6$ m). A similar trend is seen for the lateral location of the ETM (Fig. 4.15(b)). The y-location of the ETM remains unchanged for $\delta H_{\max} \leq -0.8$ and $\delta H_{\max} \geq -0.6$. All the y-locations of the ETM are very close to the middle axis $y = 0$ of the channel. The strength of the ETM as shown in Fig. 4.15(c) first decreases linearly up to $\delta H_{\max} = -0.6$ and then increases linearly.

Figure 4.16 shows the main transport components for the critical values of $\delta H_{\max}$, -0.8 and -0.6. The top left panel of Figs. 4.16(a) and 4.16(b) shows that negative M_0

(a) *x*-location of ETM

(b) *y*-location of ETM

(c) Maximum concentration of ETM
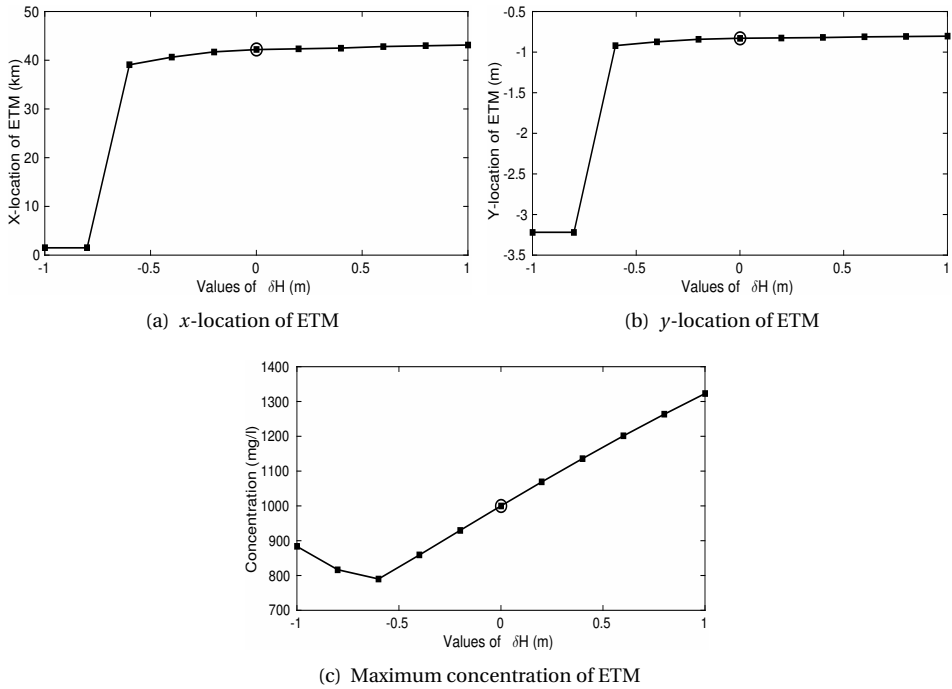
Figure 4.15: Influence of shallowing and deepening on the location and strength of ETM. The *top left panel* shows the *x*-location or the distance from the entrance of the ETM and the *top right panel* the *y*-location of the ETM. The *bottom panel* shows the strength of the ETM in terms of maximum suspended sediment concentration at the surface. In all the panels, solid black squares indicate the model results and black circle indicates the data for the reference case.

transport becomes much stronger when $\delta H_{\max}$ changes from -0.8 to -0.6. The other transport components (M_2, M_4 and surface) show minor changes for $\delta H_{\max} = -0.8$ to $\delta H_{\max} = -0.6$. These changes, however, are much smaller compared to ones for M_0 transport. This shows that the strong change in the M_0 transport is responsible for the change in the location of ETM when when increasing $\delta H_{\max}$ from -0.8 to -0.6.

4.4.4. RISE OR FALL OF THE SEA LEVEL

The influence of rise and fall in the sea level on the ETM dynamics is investigated by changing the overall depth h of the channel by a small amount δh, i.e., $h \to h + \delta h$. A positive value of δh mimics the rise in the sea level and a negative value, a fall in the sea level. In this chapter, we will mainly focus on the fall and rise in sea level by 1 m, i.e., δh = -1 and 1. As shown in Fig. 4.17, in both cases, the bed profile remains unchanged but the range of depth changes; 2 m to 9 m for fall in the sea level (Fig. 4.17(b)) and from 4 m to 11 m for rise in the sea level (Fig. 4.17(b)).

Figure 4.18 shows the availability of fine sediments due to fall and rise of the sea level. Concerning the fall of the sea level, Fig. 4.18(a), the maximum sediment availability is
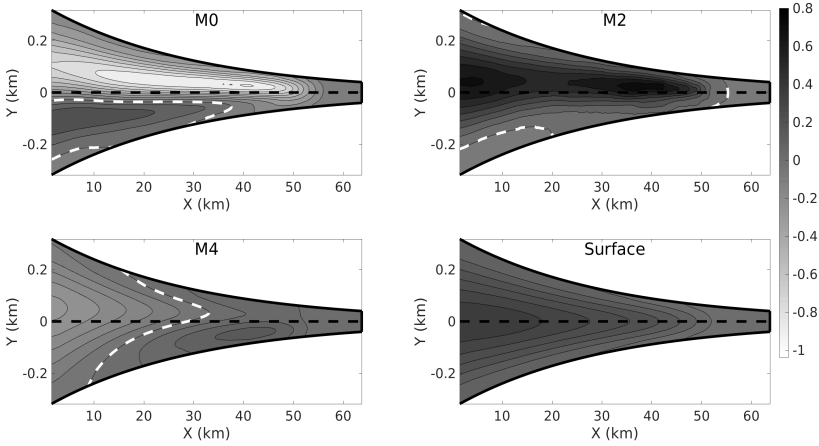
(a) Shallowed channel ($\delta H_{\max}$ = -0.8)
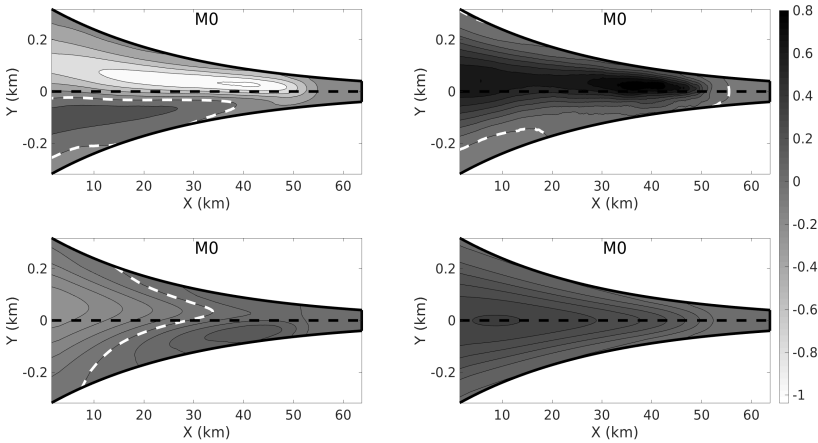
(b) Deepened channel ($\delta H_{\max}$ = -0.6)

Figure 4.16: Longitudinal suspended sediment transport terms for shallowed (*top figure*) and deepened (*bottom figure*) channels. In each of these figures (top and bottom), *top right subpanel* shows the M_0 transport, *top right subpanel* the M_2 transport, *bottom left subpanel* the M_4 transport and *bottom right subpanel* the surface transport. The black dashed line indicates the middle of the channel and the black solid lines on the sides, the domain boundaries. The white dashed line indicates the zero contour of the transport component being plotted.

found at the seaward side with a magnitude (approx. 4×10^{-4}) smaller than in the reference case (approx. 4.5×10^{-4}). Furthermore, the sediment availability decreases along the length of the estuary with maximum availability at the seaward side and minimum availability at the landward side. For the case with rise in the sea level, the location of

(a) Fall in the sea level by 1 m   (b) Rise in the sea level by 1 m
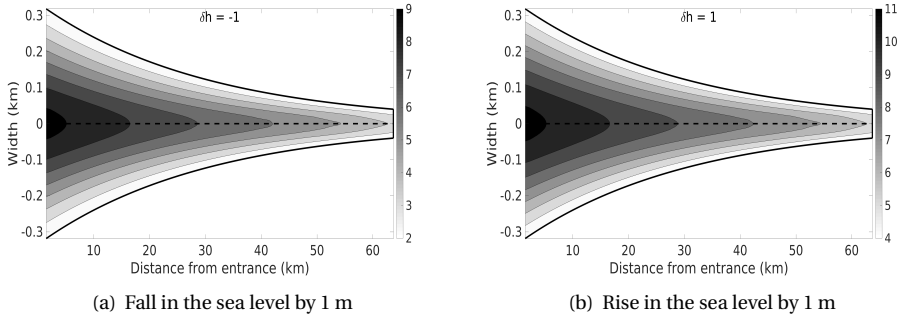
Figure 4.17: Bathymetric profiles due to fall (*left panel*) and rise (*right panel*) in the sea level. For fall in the sea level, $\delta h = -1$ is used and for rise in the sea level $\delta h = 1$. The units in the colorbar are m.

(a) Sed. availability for $\delta h = -1$ (b) Sed. availability for $\delta h = 1$
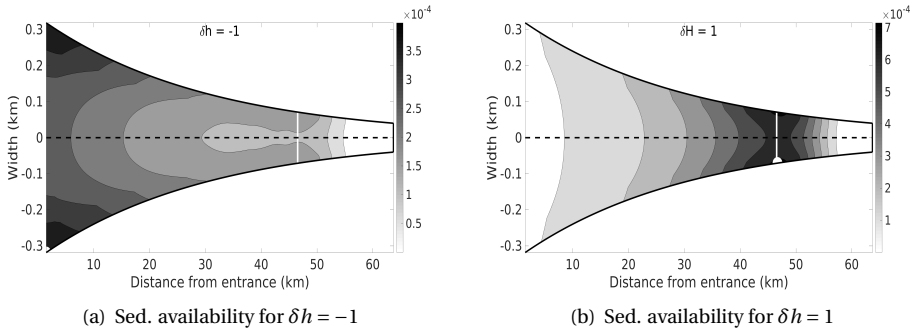
Figure 4.18: Availability of fine sediments at the bottom for fall (*left panel*) and rise (*right panel*) of the sea level. The white circle denotes the location of maximum sediment availability for the current case and white line, the x-location of maximum availability for the reference case. The sediment availability is a dimensionless quantity and hence no units are associated with the colorbar.

maximum availability remains the same as for the reference case. However, the maximum sediment availability becomes twice (approx. 7×10^{-4}) the reference case (approx. 4×10^{-4}). The sediment availability for rise in the sea level becomes almost negligible at the seaward and landward sides.

Next we look at the suspended sediment concentration at the surface for both these cases. Figure 4.19(a) shows that for the fall in the sea level, the ETM is found close to the seaward side with an enhanced strength (approx. $1100\,\mathrm{mg\,l^{-1}}$) compared to the reference case ($1000\,\mathrm{mg\,l^{-1}}$). The suspended sediment concentration decreases from the seaward side to the landward side. For rise in the sea level (Fig. 4.19(b)), the ETM is found close to the location for the reference case but with an enhanced strength (approx. 1400 mg $\mathrm{l^{-1}}$). The suspended sediment concentration at the surface is almost negligible at the seaward and landward sides. Furthermore, the ETM for this case is confined to a smaller region than in the reference case.

Next, we systematically change the values of δh and investigate the influence on the

(a) SSC at surface for $\delta h = -1$ (b) SSC at surface for $\delta h = 1$
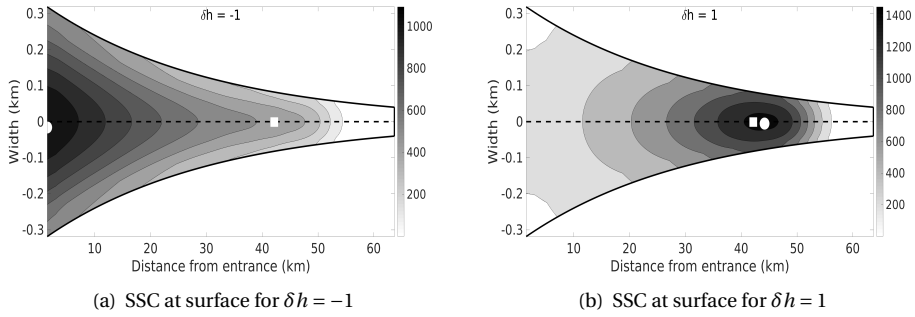
Figure 4.19: Suspended sediment concentration at the surface for fall (*left panel*) and rise (*right panel*) in the sea level. The white circle indicates the location of ETM for the current case and white square, for the reference case. The units in the colorbar are mg l^{-1}.

4

location and strength of the ETM. Figure 4.20(a) shows that the location of ETM remains

(a) x-location of ETM   (b) y-location of ETM

(c) Maximum concentration of ETM
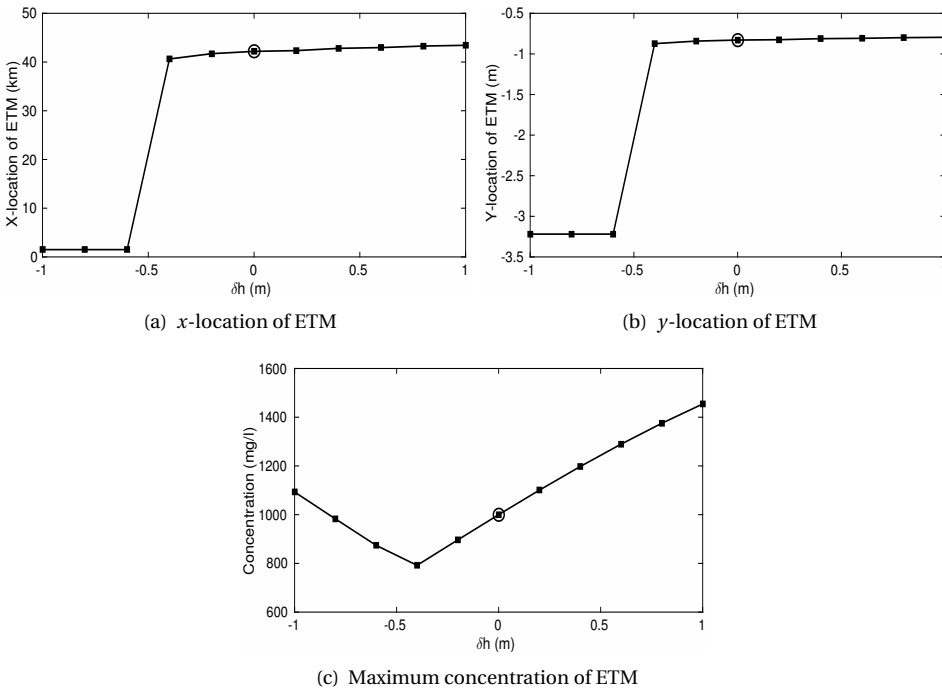
Figure 4.20: Influence of changes in the sea level (δh) on the location and strength of ETM. The *top left panel* shows the x-location or the distance of the ETM from the seaward side and the *top right panel*, the y-location of the ETM. The *bottom panel* shows the strength of the ETM in terms of maximum suspended sediment concentration at the surface. In all the panels, solid black squares indicate the model results and black circle indicates the reference case.

close to the seaward side for $\delta h \leq -0.6$ m. For $\delta h \geq -0.4$ m, the ETM is located towards the landward side (approx. 40 km from the entrance). Figure 4.20(b) suggests that the ETM remains located around the middle of the channel for all values of changes in the sea level. The strength of the ETM first decreases linearly up to $\delta h = -0.4$ m and then increases almost linearly.

We now focus on the main transport components for $\delta h = -0.6$ m and $\delta h = -0.4$ m. Like in the case of channel shallowing, the top left panels of Figs. 4.21(a) and 4.21(b) show that the M_0 transport change between $\delta h = -0.6$ m and $\delta h = -0.4$ m. The other transport components show little change between $\delta h = -0.6$ m and $\delta h = -0.4$ m, indicating that changes in the M_0 transport are the main cause for the shift of the ETM from the seaward side to the landward side.

4.5. DISCUSSION

4.5.1. ASYMMETRIC BED PROFILE

For asymmetric bed profiles, parameter $\psi = -0.5$ gives a negatively skewed bed profile, $\psi = 0.5$, a positively skewed bed profile and $\psi = 0$, a symmetric (nominal) bed profile. Figure 4.22(a) shows the major width-averaged subcomponents of the M_0 transport, i.e., $T_{M_0,RD}$, $T_{M_0,GC}$ and $T_{M_0,TRF}$ (see chapter 3 for the meaning of various symbols). Figure 4.22(a) shows that major change to M_0 transport is due to the contribution related to river discharge ($T_{M_0,RD}$). The strength of $T_{M_0,RD}$ transport component decreases when going from negatively skewed bed profile ($\psi = -0.5$, dashed line) to positively skewed bed profile ($\psi = 0.5$, dotted line) with location of maximum transport moving seaward. A minor change is seen for the other M_0 transport subcomponents such as $T_{M_0,GC}$ and $T_{M_0,TRF}$.

For the M_2 transport, the major contributions are $T_{M_2,RD}$, $T_{M_2,GC}$, $T_{M_2,EF}$, $T_{M_2,TRF14}$, and $T_{M_2,NS14}$. Figure 4.22(b) shows that contrary to the M_0 transport, the M_2 transport due to river discharge $T_{M_2,RD}$ increases when going from negatively skewed bed profile ($\psi = -0.5$) to positively skewed bed profile ($\psi = 0.5$). The M_2 transport due to externally prescribed M_4 tidal forcing $T_{M_2,EF}$ increases with increasing value of ψ. The maximum of $T_{M_2,EF}$ moves landward with increasing value of ψ pushing the sediment more into the estuary. The M_2 transport due to tidal return flow $T_{M_2,TRF14}$ also increases with increasing value of ψ. Note that the peaks of $T_{M_2,RD}$, $T_{M_2,EF}$, and $T_{M_2,TRF14}$ transport subcomponents are found in the same proximity. The M_2 transport due to gravitational circulation $T_{M_2,GC}$ and no-stress $T_{M_2,NS14}$ shows small changes in their magnitude.

4.5.2. SHALLOWING AND DEEPENING OF CHANNEL

Figure 4.23 shows the major subcomponents of the transport components T_{M_0} and T_{M_2} for the shallowing and deepening of the channel by 1 m, i.e., $\delta H_{\max} = -1$ m and $\delta H_{\max} = 1$ m, respectively. Note that unlike the previous case for asymmetric bed profile, the transport subcomponent $T_{M_0,TRF}$ also changes significantly together with $T_{M_0,RD}$ when going from shallowing by 1 m to deepening by 1 m. The changes in the transport component $T_{M_0,GC}$ are small. When going from shallowing to deepening by 1 m, the strength of the transport subcomponent $T_{M_0,RD}$ decreases at the landward side (approx. 48 km from the entrance) and increases at the seaward side. The transport subcompo-
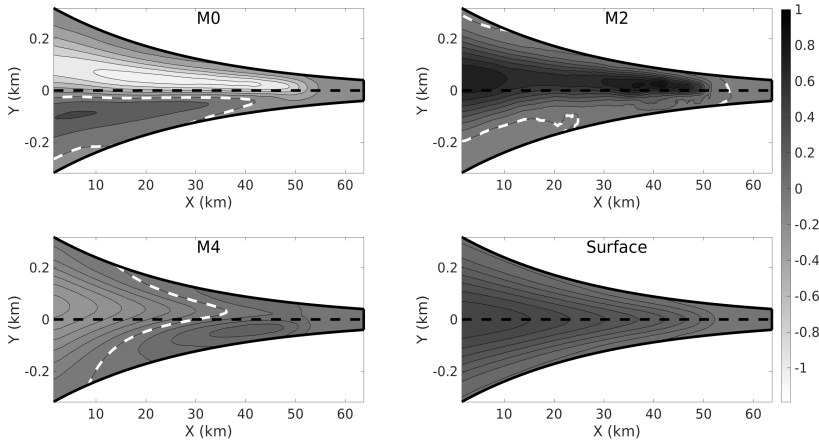
(a) Change in the sea level by δh = -0.6 m
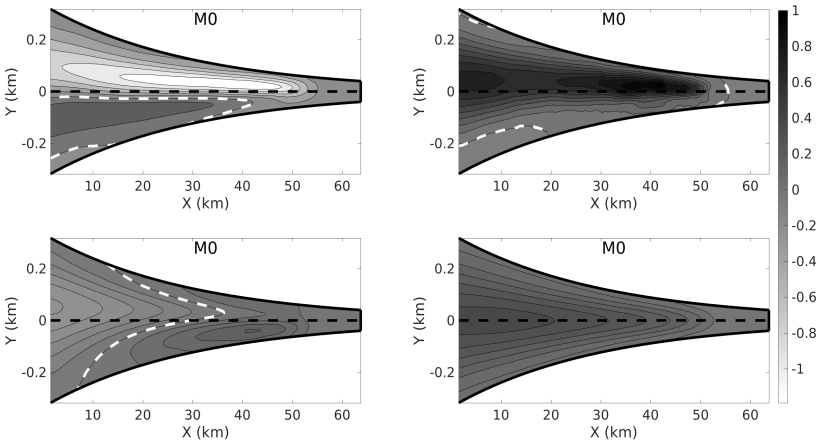
(b) Change in the sea level by δh = -0.4 m

Figure 4.21: Longitudinal suspended sediment transport terms for fall (*top figure*) and rise (*bottom figure*) of the sea level. In each of these figures (top and bottom), *top right subpanel* shows the M_0 transport, *top right subpanel* the M_2 transport, *bottom left subpanel* the M_4 transport and *bottom right subpanel* the surface transport. The black dashed line indicates the middle of the channel and the black solid lines on the sides, the domain boundaries. The white dashed line indicates the zero contour of the transport component being plotted.

nent $T_{M_0,TRF}$ becomes stronger at the seaward side with increasing $\delta H_{\max}$.

Concerning the M_2 transport component, the major subcomponents are shown in Fig. 4.23(b). Similar to the case with a asymmetric bed profile, the M_2 transport due to river discharge $T_{M_2,RD}$ increases with increasing $\delta H_{\max}$. The M_2 transport due to exter-

(a) Dominant subcomponents of M_0 transport   (b) Dominant subcomponents of M_2 transport
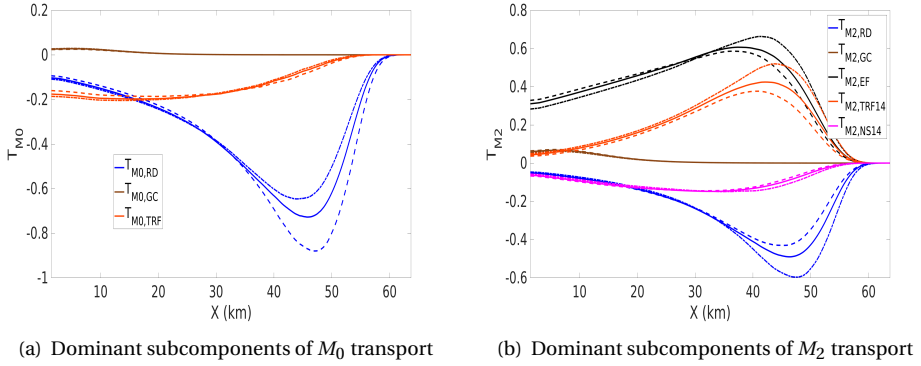
Figure 4.22: Dominant width-averaged subcomponents of the M_0 (*left panel*) and M_2 (*right panel*) transport components for bed profiles with $\psi = -0.5$ (dashed line), $\psi = 0$ (solid line) and $\psi = 0.5$ (dotted line).

(a) Dominant subcomponents of M_0 transport   (b) Dominant subcomponents of M_2 transport
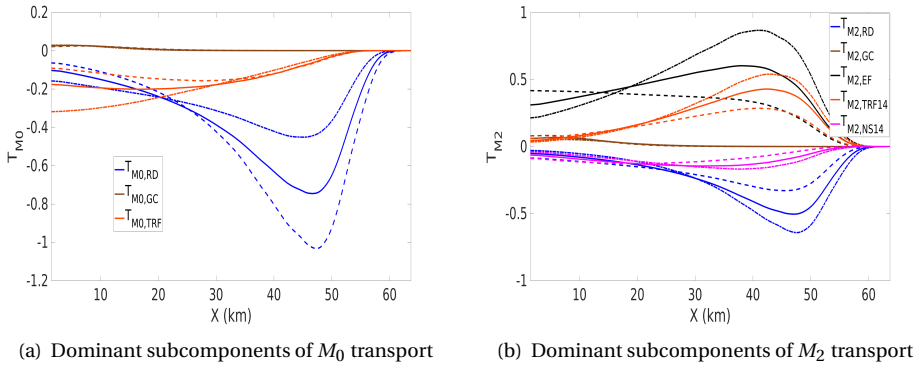
Figure 4.23: Dominant subcomponents of the M_0 (*left panel*) and M_2 (*right panel*) transport components for shallowing by 1 m ($\delta H_{\max} = -1$ m, dashed line) and deepening ($\delta H_{\max} = 1$ m, dotted line). The solid lines denote the nominal case i..e, $\delta H_{\max} = 0$ m.

nally prescribed M_4 tidal forcing $T_{M_2,EF}$ is the most dominating subcomponent and it increases with increasing value of $\delta H_{\max}$. The magnitude of the maximum $T_{M_2,EF}$ transport for $\delta H_{\max} = -1$ m is almost twice that of $\delta H_{\max} = 1$. The M_2 transport due to tidal return flow $T_{M_2,TRF14}$ also increases with increasing value of $\delta H_{\max}$. Again, the peaks of $T_{M_2,RD}$, $T_{M_2,EF}$, and $T_{M_2,TRF14}$ transport subcomponents are found in the same proximity. Rest of the subcomponents such as $T_{M_2,GC}$ and $T_{M_2,NS14}$ shows small or no changes.

The behavior of transport components for rise and fall of the sea level is similar to the behavior of transport components for shallowing and deepening of the channel and hence not shown here.

4.6. CONCLUSIONS

The influence of bathymetric changes on the location and the strength of the ETM has been investigated by using a three-dimensional semi-idealized model for water motion and sediment dynamics. The water motion is governed by the three-dimensional shallow water equations and the sediment concentration by the three-dimensional advection-diffusion equation. To obtain the spatial distribution of the sediment availability, the condition of morphodynamic equilibrium is imposed (see Kumar *et al.* [18], and Kumar *et al.* [19] for more details regarding the development of the model).

A funnel shaped estuary is considered for the experiments. The 2005 bathymetric data of the Ems estuary is used to model the along-channel profile of the estuary using a 4th degree polynomial. In the lateral direction, a possibly asymmetric Gaussian profile is prescribed. For a laterally symmetric profile, the maximum sediment availability is found approximately 46 km from the seaward side and the maximum suspended sediment concentration at the surface, approximately 42 km from the seaward side. The maximum sediment availability is found at the sides of the channel and the maximum sediment concentration, approximately in the middle of the channel.

When considering a negatively skewed bed profile, the location of maximum sediment availability is more landward and towards the upper lateral boundary compared to the symmetric case; with a higher magnitude of the maximum sediment availability in the ETM. The location of maximum suspended sediment concentration at the surface is more landward with a higher sediment concentration compared to the symmetric case. For a positively skewed bed profile, the location of maximum sediment availability is more seaward and towards the lower lateral boundary compared to the symmetric case. Furthermore, a lower magnitude of maximum sediment availability is observed in the ETM compared to the symmetric case. The location of maximum suspended sediment concentration at the surface is more seaward with a lower concentration compared to the symmetric case. Systematically varying the asymmetricity of the lateral bed profile shows that the location of maximum suspended sediment concentration at the surface consistently moves seaward and from left to right in the lateral direction with decreasing maximum concentrations.

The influence of shallowing or deepening of the channel is modeled by varying the maximum depth of the channel attained at the middle of the channel. The results show that when shallowing the channel by 1 m, the location of the maximum sediment availability moves completely to the seaward side. For deepening of the channel by 1 m, the location of the maximum sediment availability remains unchanged but its magnitude increases. For the shallowed channel, the maximum suspended sediment concentration at the surface is found at the seaward side with lower concentration compared to the symmetric case. For the deepened channel, the maximum suspended sediment concentration is found at the same location as for the laterally symmetric bed profile but with a higher concentration. Running the model for several values of shallowing and deepening shows that the location of maximum suspended sediment concentration at the surface moves landward and from left to right in the lateral direction when systematically moving from shallowing to the deepening of the channel.

Finally, the overall depth is varied to mimic the fall and rise of the sea level. For the fall of the sea level by 1 m, the location of the maximum sediment availability moves

completely to the seaward side. On the other hand, for rise of the sea level by 1 m, the location of the maximum sediment availability remains unchanged. For the fall of the sea level, the location of maximum suspended concentration at the surface moves to the seaward side with a higher concentration compared to the symmetric case. For the rise of the sea level by 1 m, the location of maximum suspended sediment concentration at the surface moves more landward with a much higher concentration compared to the symmetric case. The results show that the location of maximum suspended sediment concentration at the surface moves landward and from left to right in the lateral direction when systematically moving from fall to the rise of the sea level.

REFERENCES

[1] J. F. Festa and D. V. Hansen, *Turbidity maxima in partially mixed estuaries: A two-dimensional numerical model,* Estuarine and Coastal Marine Science **7**, 347 (1978).

[2] D. A. Jay and J. D. Musiak, *Particle trapping in estuarine tidal flows,* Journal of Geophysical Research **99**, 20,445 (1994).

[3] V. N. De Jonge, H. M. Schuttelaars, J. E. E. Van Beusekom, S. A. Talke, and H. E. De Swart, *The influence of channel deepening on estuarine turbidity levels and dynamics, as exemplified by the Ems estuary,* Estuarine, Coastal and Shelf Science **139**, 46 (2014).

[4] N. K. Ganju and D. H. Schoellhamer, *Chapter 24 Lateral variability of the estuarine turbidity maximum in a tidal strait,* Proceedings in Marine Science **9**, 339 (2008).

[5] D. H. Peterson and J. F. Festa, *Numerical Simulation of phytoplankton productivity in partially mixed estuaries,* Estuarine, Coastal and Shelf Science **19**, 563 (1984).

[6] A. S. Chernetsky, H. M. Schuttelaars, and S. A. Talke, *The effect of tidal asymmetry and temporal settling lag on sediment trapping in tidal estuaries,* Ocean Dynamics **60**, 1219 (2010).

[7] H. M. Schuttelaars, V. N. De Jonge, and A. S. Chernetsky, *Improving the predictive power when modelling physical effects of human interventions in estuarine systems,* Ocean and Coastal Management **79**, 70 (2013).

[8] K. M. H. Huijts, H. M. Schuttelaars, H. E. De Swart, and A. Valle-Levinson, *Lateral entrapment of sediment in tidal estuaries: An idealized model study,* Journal of Geophysical Research **111**, C12016 (2006).

[9] S. N. Chen and L. P. Sanford, *Axial Wind Effects on Stratification and Longitudinal Salt Transport in an Idealized, Partially Mixed Estuary*,* Journal of Physical Oceanography **39**, 1905 (2009).

[10] S. N. Chen, L. P. Sanford, and D. K. Ralston, *Lateral circulation and sediment transport driven by axial winds in an idealized, partially mixed estuary,* Journal of Geophysical Research: Oceans **114**, 1 (2009).

[11] G. P. Schramkowski, H. E. De Swart, and H. M. Schuttelaars, *Effect of bottom stress formulation on modelled flow and turbidity maxima in cross-sections of tide-dominated estuaries,* Ocean Dynamics **60**, 205 (2010).

[12] K. M. H. Huijts, H. E. De Swart, G. P. Schramkowski, and H. M. Schuttelaars, *Transverse structure of tidal and residual flow and sediment concentration in estuaries,* Ocean Dynamics **61**, 1067 (2011).

[13] Z. Yang, H. E. De Swart, H. Cheng, C. Jiang, and A. Valle-Levinson, *Modelling lateral entrapment of suspended sediment in estuaries: The role of spatial lags in settling and m4 tidal flow,* Continental Shelf Research **85**, 126 (2014).

[14] W. R. Geyer, R. P. Signell, and G. C. Kineke, *Lateral trapping of sediment in a partially mixed,* in *Physics of Estuaries and Coastal Seas,* edited by J. Dronkers and M. Scheffers, PECS 96 (Balkema, 1998) pp. 155–124.

[15] Y. H. Kim and G. Voulgaris, *Lateral circulation and suspended sediment transport in a curved estuarine channel: Winyah Bay, SC, USA,* Journal of Geophysical Research: Oceans **113**, 1 (2008).

[16] J. T. F. Zimmerman, *On the Lorentz linearization of a nonlinearly damped tidal Helmholtz oscillator,* Proceedings of the Koninklijke Nederlandse Akademi **95**, 127 (1992).

[17] E. Ensing, H. E. De Swart, and H. M. Schuttelaars, *Sensitivity of tidal motion in well-mixed estuaries to cross-sectional shape, deepening, and sea level rise,* Ocean Dynamics , 933 (2015).

[18] M. Kumar, H. M. Schuttelaars, P. C. Roos, and M. Möller, *Three-dimensional semi-idealized model for tidal motion in tidal estuaries: An application to the Ems estuary,* Ocean Dynamics **66**, 99 (2016).

[19] M. Kumar, H. M. Schuttelaars, and P. C. Roos, *Three-dimensional semi-idealized model for estuarine turbidity maxima in tidally dominated estuaries,* Ocean Modelling **113**, 1 (2017).

4

5

CONCLUSIONS

5.1. RETROSPECTION

The following research questions were posed in the introduction chapter of this thesis:

1. *How can the three-dimensional water motion in an estuary with complex shape and bathymetry be decomposed in contributions resulting from different forcing mechanisms?*

2. *How can such a model be extended to include the three-dimensional sediment dynamics and sediment trapping, resulting in the formation of ETM?*

3. *What is the sensitivity of the trapping location to anthropogenic (e.g., channel deepening) and natural changes (e.g., sea level rise) in a funnel shaped estuary?*

These questions have systematically been answered in this thesis by developing a three dimensional idealized model for tidal motion and sediment dynamics and by performing bathymetric sensitivity analyses. In the next section (5.2), we present the main conclusions together with the answers to above questions.

5.2. MAIN CONCLUSIONS

The goal of this thesis was to develop an idealized model that is specifically geared towards increasing our understanding of the dynamics of the estuarine turbidity maximum in estuaries of arbitrary shape (geometry and bathymetry), including Coriolis effects. Due to the arbitrary shape of the estuary and inclusion of Coriolis effects, there is a strong correlation between the longitudinal and lateral processes. Hence, a three-dimensional model is needed. For this purpose, the water-motion is described by three-dimensional shallow water equations and the suspended sediment concentration follows from a three-dimensional advection-diffusion equation with sources and sinks. Furthermore, the estuary is required to be in morphodynamic equilibrium which means that there is no evolution of the bed averaged over the tidal scale. This condition can

111

only be achieved if the fine sediments have a specific spatial distribution on the bottom of the estuary. While developing the model, the following assumptions were made;

- The horizontal viscous and diffusivity effects are ignored compared to the vertical viscous effects. It means that the horizontal boundary layer is ignored compared to the vertical boundary layer.

- The estuary is assumed to be partially- to well-mixed.

- The eddy viscosity and stress parameter are assumed to be functions of horizontal coordinates only.

- The M_2 tidal constituent is assumed to be the dominant one compared to the M_4 tidal constituent and river discharge.

- The total amount of easily erodible sediments in the estuary is prescribed.

The model developed to describe the M_2 water motion is presented in **chapter 2**. This answers Research Question 1 posed in section 5.1 with respect to the M_2 water motion. The striking feature of the model lies in the fact that the vertical profile of the M_2 velocity is known completely analytically in terms of the surface elevation gradients. Integrating the continuity equation for M_2 water motion in the vertical direction over the water column and using the appropriate boundary conditions, results in a two-dimensional elliptic partial differential equation for the M_2 surface elevation. Since the shape (geometry and bathymetry) of the estuary is assumed to be arbitrary and physical parameters are assumed to be arbitrary functions of the horizontal coordinates, the elliptic equation for the M_2 surface elevation can, in general, not be solved analytically. The finite element method is adopted to solve this equation. Linear and quadratic polynomial functions are chosen as basis functions for the finite element method. The first-order partial derivatives are computed using so-called direct derivative (DD) method and ZZ-method. For the second-order partial derivatives, a new method called mixed-method, which is a hybrid of DD-method and ZZ-method, is introduced. To check the accuracy of the model, the model results are first compared with the model results of a width-averaged (2DV) idealized model developed by Chernetsky *et al.* [1] for an exponentially converging domain. The results for the surface elevation and the partial derivatives converge with the expected rate of convergence. Next, the model results are compared with the model results of a three-dimensional idealized model developed by Winant [2] for a narrow (width is much smaller than the length) rectangular channel. The results for the surface elevation and horizontal and vertical velocities agree well. These two comparisons ensure the accuracy of the model. The model is then applied to the Ems estuary using a realistic geometry and bathymetry for the year 2005. A good agreement is found for the M_2 water level and phase among the observations, model results of the newly developed semi-idealized model and the models results of a complex numerical model (Van Maren *et al.* [3]). To understand the influence of the width-profile only (meandering effects neglected), the width-profile of the Ems estuary is approximated using an exponential function and a polynomial function. The model results suggest that, for surface elevation and the absolute value of the depth-averaged horizontal velocity, approximating the width-profile with a polynomial function gives better results than approximating with an exponential function. This indicates that a more accurate description

of the geometry of the Ems estuary must be taken into account. To summarize I find: *the three-dimensional idealized model of Winant [2] for the M_2 water motion developed for a narrow channel with simplified bed profile is extended to an estuary with arbitrary geometry and bathymetry with horizontally varying physical parameters. The extensive convergence analyses show that the model converges with expected rate of convergence. When applied to the Ems estuary using a realistic geometric and bathymetric data of the year 2005, the model produces satisfactory results for the amplitude and the phase of the M_2 water motion.*

Chapter 3 focuses on the development of the model for the trapping of fine sediments in tidally-dominated estuaries. To this end, residual and M_4 water motion and suspended sediment concentration have to be solved as well. This answers the remaining part of the first Research Question and complete second Research Question posted in section 5.1. As in chapter 2, the vertical profile of the residual and M_4 velocities can be expressed in terms of the gradients of the residual and M_4 water level, respectively. Integrating the continuity equation in the vertical over the water column gives a two-dimensional elliptic partial differential equation for the surface elevation. The three-dimensional profile of the suspended sediment concentration (residual, M_2 and M_4 constituents) is completely known in terms of the horizontal velocity (residual, M_2 and M_4 constituents) at the bottom (bed shear stress) and can be computed analytically. However, the suspended sediment concentration also depends on an unknown coefficient called the sediment availability. Assuming morphodynamic equilibrium, the spatial profile of the easily erodible fine sediment follows from a two-dimensional partial differential equation for the sediment availability. As in chapter 2, the elliptic equations for the residual and M_4 water level and the sediment availability are solved numerically using the finite element method. We find that when the polynomials of degree q for the M_2 water motion and polynomials of degree at least $q-1$ for the residual and M_4 water motion and sediment availability are used as basis functions in the finite element method, the overall model converges with rate $q-1$. For this reason, the third-degree polynomials for the M_2 water motion and second-degree polynomials for the rest of the component are used as basis functions. Next, this model is applied to the Ems estuary for parameters representative for years 1980 and 2005. The width is assumed to be exponentially convergent. The bathymetry in the longitudinal direction is taken from the measurements and is approximated with a smooth function (polynomial of degree four). In the first experiment, the bathymery is assumed to be uniform in the lateral direction. Focusing on the year 1980, the estuarine turbidity maximum (ETM) is found close to the seaward side. For the year 2005, the ETM moves far landward, approximately 38 km away from the entrance, indicating that the three-dimensional model is able to qualitatively reproduce the observed ETM behavior in the Ems estuary. Next, the bed profile in the lateral direction is changed to a parabolic profile. For both the 1980 and 2005 cases, it is found that the location of the ETM remains approximately the same compared to the case with laterally uniform bed profile. However, the highest concentration is found in the middle of the channel even though most of the easily erodible sediment is found at the sides. To summarize I find: *the semi-idealized model developed in chapter 2 for the M_2 water motion is extended to the trapping of the fine sediments by solving for the residual and M_4 water motion and suspended sediment concentration together with the con-*

dition of morphodynamic equilibrium. The overall accuracy of the model is guaranteed by choosing a proper combination of cubic and quadratic polynomials as basis functions. As a first application, the model is applied to the Ems estuary with simplified geometry and bathymetry and the model is able to qualitatively reproduce the locations of the ETM for both 1980 and 2005.

In chapter 4, the influence of bathymetric changes on the location and strength of the estuarine turbidity maximum is investigated. The anthropogenic and natural changes are limited to changes in the bathymetric profile and therefore this chapter answers the third Research Question from section 5.1. An exponential domain with laterally symmetric bathymetric profile acts as a reference case. Systematically varying the asymmetricity of the lateral bed profile, i.e., the maximum depth in the lateral direction is no more attained in the middle, from negatively skewed to positively skewed bed profile shows that the location of maximum suspended sediment concentration at the surface consistently moves seaward and from left to right in the lateral direction with decreasing maximum concentration. To understand the impact of shallowing or deepening of the channel, the maximum depth, which is attained at the middle of the channel, is varied. When moving from shallowing of the channel to the deepening of the channel, the location of maximum suspended sediment concentration at the surface moves landward and from left to right in the lateral direction. Finally, to mimic the fall and rise of the sea level, the overall depth of the channel is varied. The model suggests that when going from fall of the sea level to the rise of the sea level, the location of maximum suspended sediment concentration at the surface moves landward and from left to right in the lateral direction. To summarize: *these numerical experiments demonstrate that the three-dimensional idealized model developed in this thesis can be used to gain physical insight of the system related to the dynamics of the estuarine turbidity maximum. The quick simulation time allows to perform sensitivity analyses of various parameters as done for the bathymetric profile in this chapter. This opens the door of the use of this model for other applications.*

5.3. RECOMMENDATIONS

This thesis has mainly focussed on the development of a three-dimensional idealized model that is able to capture the dynamics of the estuarine turbidity maximum. Both concerning the physical description and the solution method, specific choices and parametrizations were made. We list specific aspects which can be improved and few suggested applications of this model:

Depth-dependent eddy viscosity: In this model, the eddy viscosity is assumed to be uniform in the vertical direction and time. This can be extended by using a more realistic profile of the eddy viscosity varying in the vertical direction and also with time. Doing this for an arbitrary profile of depth-dependent eddy viscosity may no longer allow to solve the vertical profile of the velocity analytically.

More accurate numerical solution: The surface elevation and the sediment availability follow from a two-dimensional elliptic partial differential equation. The velocity and the suspended sediment concentration depend on the partial derivatives of the surface

elevation. In this paper, the DD-method was used to compute the partial derivatives. The accuracy of the numerical solution decreases by one each time the DD-method is used to compute the partial derivatives. This has a direct impact on the overall accuracy of the model. This problem can be overcome by solving the surface elevation and its partial derivatives simultaneously. In this case, instead of having one differential equation for the surface elevation, one will have to solve a system of differential equations which will contain surface elevation and its partial derivatives as unknowns.

Time dependent availability: The availability of fine sediments is computed when the system has reached morphodynamic equilibrium. However, the behaviour of fine sediments while reaching that process is also of great importance. This can be achieved by taking the sediment availability to be varying in time as well. This will help us to understand the behaviour of sediment availability during the tidal cycle till it reaches the morphodynamic equilibrium.

Retention basin: The influence of retention basins on the water motion has been studied extensively (Roos and Schuttelaars [4], Alebregtse and De Swart [5], Alebregtse *et al.* [6]). However, no idealized modelling approach has been used to understand the impact of a retention basin on the sediment transport and the location of the estuarine turbidity maximum. This model can be easily used to study this case.

Application to other estuaries: In this thesis, the model has been applied to the Ems estuary. However, this model is an excellent tool to systematically understand the influence of shape of the estuary and the various physical parameters on the sediment transport in any tidally dominated estuary. Hence, this model can be applied to any tidally-dominated and partially-mixed estuary satisfying the underlying assumptions. The Pearl River Estuary in China is an excellent example of such an estuary. Like the Ems estuary, this estuary has also gone through anthropogenic changes and the water motion and sediment dynamics has also changed. This model then can be applied to identify the most dominating factor causing the changes.

REFERENCES

[1] A. S. Chernetsky, H. M. Schuttelaars, and S. A. Talke, *The effect of tidal asymmetry and temporal settling lag on sediment trapping in tidal estuaries,* Ocean Dynamics **60**, 1219 (2010).

[2] C. D. Winant, *Three-Dimensional Tidal Flow in an Elongated, Rotating Basin,* Journal of Physical Oceanography **37**, 2345 (2007).

[3] D. S. Van Maren, J. C. Winterwerp, and J. Vroom, *Fine sediment transport into the hyper-turbid lower Ems River: the role of channel deepening and sediment-induced drag reduction,* Ocean Dynamics **65**, 589 (2015).

[4] P. C. Roos and H. M. Schuttelaars, *Resonance properties of tidal channels with multiple retention basins: role of adjacent sea,* Ocean Dynamics **65**, 311 (2015).

[5] N. C. Alebregtse and H. E. De Swart, *Effect of a secondary channel on the non-linear tidal dynamics in a semi-enclosed channel: a simple model,* Ocean Dynamics **64**, 573 (2014).

[6] N. C. Alebregtse, H. E. De Swart, and H. M. Schuttelaars, *Resonance characteristics of tides in branching channels,* Journal of Fluid Mechanics **728**, R31 (2013).

5

SUMMARY

Estuaries have played a crucial role in the development of human civilization. In the course of time, estuaries have gone through several adverse changes in terms of increase in the water level and sediment concentration. This has lead to changes in the location and strength of sediment trapping locations, also known as estuarine turbidity maxima. The main objective of this thesis is to develop a three-dimensional model to understand the dynamics of estuarine turbidity maxima in tidally dominated estuaries with arbitrary geometry and bathymetry. A major part of this thesis is dedicated to the development of this model.

To develop such a model, three dimensional equations governing the water motion and sediment dynamics are needed. Three-dimensional shallow water equations for water motion and three-dimensional advection-diffusion equation for sediment concentration are solved. An extra condition of morphodynamic equilibrium is imposed to govern the availability of fine sediments in the estuary. This condition together with the proper boundary conditions complete the mathematical model. Using scaling and perturbation analyses results in a small parameter ϵ which is the ratio of the mean amplitude of the M_2 surface elevation and the mean water depth at the seaward boundary. This leads to a system of equations at each order of ϵ for the water motion and the suspended sediment concentration. A striking feature of the model is that for both leading-order and first-order water motion, the vertical structure of the velocity can be analytically expressed in terms of the gradients of the water level. As a first step towards the development of the model, we focus on the leading-order water motion. A combination of analytical and numerical (finite element method) techniques are used to solve these equations for leading-order water motion. The model is verified by comparing the model results with results of other idealized models. The model for leading-order water motion shows that approximating the geometry of the Ems estuary with 9th degree polynomial gives better results for the amplitude and phase of the M_2 tide than approximating it with an exponential function. Furthermore, the leading-order model captures the amplitude and phase of the M_2 tide of the Ems estuary quite well when compared to the field observations and results from a state-of-the-art complex model.

Next, the first-order system of equations for water motion and leading- and first-order systems of equations for the suspended sediment concentration are solved. The first-order water motion consists of M_0 (residual) and M_4 (overtide) constituents which themselves can be decomposed into several contributions due to externally prescribed and internally generated forcing terms. For each of these contributions, a system of equations similar to the leading-order water motion is solved. The strength of the model lies in the fact that each contribution can be investigated independently. Regarding the sediment concentration, both leading-order and first-order system of equations are solved analytically in terms of the leading-order and first-order horizontal velocities and can be decomposed into various subcomponents. The condition of morphody-

namic equilibrium yields a two-dimensional elliptic differential equation for the sediment availability which is solved numerically. With the choice of proper basis functions in the numerical solution, the convergence of the whole model is ensured. When applied to the Ems estuary with parameter values representative of year 2005, the model wonderfully mimics the location of the estuarine turbidity maximum.

To understand the influence of anthropogenic and natural changes on the location and strength of estuarine turbidity maximum, the three-dimensional model is applied to an estuary with an exponentially converging domain and a laterally symmetric bathymetric profile. The model shows that the distance from the seaward side and the strength of the estuarine turbidity maximum changes with varying asymmetry of the bathymetry. In all cases, the maximum availability of fine sediments is found at the lateral sides and the maximum suspended sediment concentration, close to the middle of the channel. As expected, the presence of the Coriolis force distorts the symmetry of the various transport subcomponents. The model also suggests that shallowing or deepening of the channel can completely shift the estuarine turbidity maximum from seaward side to the landward side. A similar trend is seen when investigating the influence of long term changes in the sea level on estuarine turbidity maximum. These numerical experiments demonstrate the strength of the model and its use in several applications.

SAMENVATTING

Estuaria hebben een cruciale rol gespeeld in de ontwikkeling van de menselijke beschaving. In de loop van de tijd zijn estuaria veranderd door ontwikkelingen zoals een toename van het water niveau en de sedimentconcentratie. Dit heeft geleid tot veranderingen in de positie en sterkte van locaties waar sediment wordt ingevangen, bekend als estuariene turbiditeitsmaxima. The doel van dit proefschrift is het ontwikkelen van een drie-dimensioneel model om de dynamica van estuariene turbiditeitsmaxima in getijgedomineerde estuaria met arbitraire geometrie en bathymetrie te begrijpen. Een groot deel van dit proefschrift is gewijd aan de ontwikkeling van dit model.

Voor de ontwikkeling van het model worden de drie-dimensionele ondiepwatervergelijkingen voor de waterbeweging en een drie-dimensionele advectie-diffusievergelijking voor de sedimentconcentratie gebruikt en opgelost. Daarnaast wordt de morfodynamisch-evenwichtsvoorwaarde voorgeschreven om de beschikbaarheid van fijn sediment in het estuarium te bepalen. Deze vergelijkingen vormen, samen met de randvoorwaarden, het totale model. Door gebruik te maken van schalings- en storingsanalyse, wordt een kleine parameter ϵ afgeleid, welke de verhouding tussen de gemiddelde M_2 getijamplitude en de gemiddelde waterdiepte aan de zeewaartse rand voorstelt. De analyse leidt vervolgens tot een stelsel vergelijkingen op iedere orde van ϵ voor de water beweging en de sedimentconcentratie. Een opvallende eigenschap van het model is dat, voor zowel de leidende- als eerste-orde water beweging, het verticale snelheidsprofiel analytisch kan worden uitgedrukt in termen van de waterniveaugradiënt. Als eerste stap in de modelontwikkeling richten we ons op de leidende-orde waterbeweging. De vergelijkingen hiervoor worden opgelost met een combinatie van analytische en numerieke (eindige elementen methode) technieken. Het model is geverifieerd door de resultaten te vergelijken met resultaten van andere geïdealiseerde modellen. Het model voor de leidende-orde waterbeweging laat zien dat betere resultaten voor de M_2 getijamplitude en –fase worden verkregen als de geometrie van het Eems estuarium wordt benaderd met een negende-orde polynoom dan wanneer dit wordt benaderd met een exponentiele functie. Daarnaast is het model in staat de amplitude en fase van het M_2 getij in het Eems estuarium goed te beschrijven in vergelijking met veldmetingen en resultaten van een 'state-of-the-art' complex model.

Hierna zijn de eerste-orde vergelijkingen voor de waterbeweging en leidende- en eerste-orde vergelijkingen voor de sedimentconcentratie opgelost. De eerste-orde waterbeweging bestaat uit een M_0 (residuele) en M_4 (overtij) component, welke elk weer verder opgedeeld kunnen worden in verscheidene bijdragen door extern voorgeschreven en intern gegenereerde forceringen. Voor ieder van deze bijdragen wordt een systeem van vergelijkingen opgelost dat lijkt op het systeem voor de leidende-orde waterbeweging. De kracht van het model is dat iedere bijdrage afzonderlijk bestudeerd kan worden. De vergelijkingen voor de sedimentconcentratie worden, voor zowel de leidende- als eerste-orde, analytisch opgelost in termen van de leidende- en eerste-orde horizon-

119

tale snelheden. Ook de sedimentconcentratie kan worden opgedeeld in verscheidene bijdragen. De morfodynamish-evenwichtsvoorwaarde leidt tot een twee-dimensionele elliptische differentiaalvergelijking voor de sedimentbeschikbaarheid, welke numeriek wordt opgelost. Door gebruik te maken van geschikte basisfuncties in de numerieke oplossing, wordt de convergentie van het gehele model gegarandeerd. Toegepast op het Eems estuarium met parameterwaarden die representatief zijn voor 2005 geeft het model een wonderbaarlijk goede representatie van de locatie van het estuarien turbiditeitsmaximum.

Om het effect van menselijke en natuurlijke veranderingen op de dynamica van het turbiditeitsmaximum te bestuderen, wordt het drie-dimensionele model toegepast op een estuarium met exponentieel convergerende geometrie en lateraal symmetrisch bodemprofiel. Het model laat zien dat de locatie en de sterkte van het turbiditeitsmaximum veranderen bij veranderende asymmetrie van het bodemprofiel. In alle gevallen wordt de grootste beschikbaarheid van fijn sediment gevonden op de laterale randen en worden de maximale gesuspendeerde sedimentconcentraties gevonden rond het midden van de hoofdgeul in de laterale richting. Zoals verwacht verstoort de Corioliskracht de symmetrie van de fysische grootheden. Het model suggereert ook dat het dieper of ondieper maken van de hoofdgeul kan leiden tot een verschuiving van het turbiditeitsmaximum van de zeewaartse naar de landwaartse kant van het estuarium. Een zelfde trend wordt waargenomen als het effect van daling of stijging van de zeespiegel op het turbiditeitsmaximum wordt bestudeerd. Deze numerieke experimenten demonstreren de kracht van het model en het gebruik ervan in verscheidene toepassingen.

ACKNOWLEDGEMENTS

Looking back, I realize that pursuing a PhD was probably one of the most important decisions I have made so far. Choosing between a job offer from a Dutch company and a PhD offer from TU Delft, was a tough choice for me. I am very glad that at that moment, I decided to go for a PhD. I believe that the PhD process has not only brought my scientific knowledge to a higher level but has also brought positive changes in my personality and attitude. This was definitely not possible because of me alone. There are many people who have contributed to it. I would like to express my deepest gratitude to these people.

First of all, I would like to express my sincere gratitude to my daily supervisor and promoter Dr. Henk Schuttelaars. I feel lucky that I could work directly with him. Apart from being a fabulous scientist, he is also a nice human being with an amazing sense of humor. He has been consistently supportive of me. I am also indebted to my co-promoter Dr. Pieter Roos for his consistent guidance and discussions. Henk and Pieter have always helped to improve the quality of my work. My special thanks to Prof. Dr. Arnold Heemink for his support and tracking the progress of my PhD. I would also like to thank Dr. Matthias Möller for helping me with computing the accurate partial derivatives of the numerical solution. Technical discussions with Dr. George Schramkowski and Prof. Dr. Huib de Swart helped me to expand my understanding about coastal dynamics. A special thanks to all my committee members for reading my thesis and giving useful comments which has helped to improve the quality of my thesis.

I would like to thank Kees Lemmens for introducing me to the world of Linux and then helping me out with many issues. Also, it is because of Kees Lemmens that I took my first gliding flight in Holland and became interested in airplanes. I am grateful to my colleagues Evelyn Sharabi and Dorothee Engering for helping me out with several matters and helping me to improve my Dutch skills through conversation.

It was great to share my workplace with some amazing people. It was a pleasure working with Wei in the daytime and then playing badminton in the evening. Thanks to Corine and Yoeri for their support and helping me out with the Dutch language including translating my summary. I am thankful to Bijan and Hoda for interesting discussions we had during and after work. I would like to thank my other colleagues Kaihua, Tugce, Eka, Atif, Nick, and Mahya for making my stay memorable.

I would like to say special thanks to Shruti for listening to all my complaints and keeping me motivated throughout my PhD. Also, thanks to Shruti for helping me to rehearse my presentations, correcting my grammatical mistakes and pronunciation. I am also grateful to Adelaide for her constant support during and after my stay in Delft. Thanks to Noopur and Abhigyan for inviting me for dinner on several occasions and having long conversations about several topics including our own experiences during PhD. It was a pleasure to meet Rahul during the PhD startup program and we have remained good friends from there on. Occasionally working with Pawan in the library, then playing badminton in the evening, followed by cooking and eating at his place kept my days

well-balanced.

My PhD journey continued in Eindhoven. This would not have been possible without the support of Hrishikesh and Shubhendu. Thanks to both of you for useful discussions (work and non-work related) in the library and for helping me out in several matters. I would also like to thank my other friends in Eindhoven and Utrecht for making my life in the Netherlands enjoyable. I feel blessed to have such friends around me. A big thank to Tina for her affection, support and deep conversations we have. It has been a long journey and I have met and enjoyed the company of many people that have directly or indirectly contributed to my PhD process.

I would like to share my deepest gratitude to my parents Sushma and Sheetal, my sisters Rupa and Hema and my brother Vishal for their unconditional love and support. Finally, in the words of Abraham Lincoln "All that I am, or hope to be, I owe to my angel mother".

Namaste
Mohit Kumar
November 2018

5

A

SCALING AND PERTURBATION ANALYSES

A.1. SCALING ANALYSES

To make the equations dimensionless, typical scales of the various quantities have to be introduced. The time t is made dimensionless using the frequency ω of the M_2 tidal constituent. In this paper, we focus on phenomena that vary on the estuarine length scale. Thus, as a length scale, the length L of the estuary is used. As a vertical length scale, the mean water depth H at the seaward side is used, defined as

$$H = \frac{1}{\text{Len}(\partial_S \Omega)} \int_{\partial_S \Omega} h \, ds, \tag{A.1}$$

where $\text{Len}(\partial_S \Omega)$ denotes the length of the seaward boundary. The local water depth h is also scaled with this parameter H. The typical scales for the surface elevation η, the vertical eddy viscosity A_v and the vertical diffusivity K_v by $\bar{A}$, $\bar{A}_v$ and $\bar{K}_v$, respectively, defined as

$$(\bar{A}, \bar{A}_v, \bar{K}_v) = \frac{1}{\text{Len}(\partial_S \Omega)} \int_{\partial_S \Omega} (A_{M_2}, A_v, K_v) \, ds. \tag{A.2}$$

The horizontal diffusivity K_h is assumed to be spatially uniform and constant in time.

The cross-sectionally averaged continuity equation is used to obtain a typical scale for the horizontal velocity $U = \frac{\bar{A}\omega L}{H}$. The typical scale W for the vertical velocity w follows from the assumption that all the terms in the three-dimensional continuity equation are of the same order of magnitude, i.e., $U/L = V/L = W/H$, implying that $W = HU/L$. Note that U is the dominant scale of the horizontal velocity in the tidally dominated estuaries. The typical magnitude for the density gradients ρ_x and ρ_y is denoted by ρ_H. The river discharge Q is made dimensionless by comparing it with the typical tidal discharge $\bar{Q}$, defined as

$$\bar{Q} = U \, \text{Len}(\partial_R \Omega) \, H, \tag{A.3}$$

Physical quantity (Symbol)	Typical scale	Symbol	Dimensionless quantity
Domain			
Time (t)	M_2 frequency	ω	$t^* = \omega t$
Horizontal coordinates (x, y)	Estuarine length	L	$(x^*, y^*) = (x, y)/L$
Domain (Ω)	Estuarine length	L	$\Omega^* = \Omega/L$
Vertical coordinate (z)	Mean depth	H	$z^* = z/H$
Water depth (h)	Mean depth	H	$h^* = h/H$
Water Motion			
Coriolis (f)	M_2 frequency	ω	$f^* = f/\omega$
Surface elevation (η)	Eq. (A.2)	$\bar{A}$	$\eta^* = \eta/\bar{A}$
Horizontal velocity (U, V)	Follows from cross-sectionally averaged continuity equation	$U = \frac{\bar{A}\omega L}{H}$	$(u^*, v^*) = (u, v)/U$
Vertical velocity (W)	Follows from three-dimensional continuity equation	$W = \frac{H}{L}U$	$w^* = w/W$
Eddy viscosity (A_v)	Eq. (A.2)	$\bar{A}_v$	$A_v^* = A_v/\bar{A}_v$
External forcing (A_{M_2}, A_{M_4})	Eq. (A.2)	$\bar{A}$	$(A_{M_2}^*, A_{M_4}^*) = (A_{M_2}, A_{M_4})/\bar{A}$
River discharge (Q)	Eq. (A.3)	$\bar{Q}$	$Q^* = Q/\bar{Q}$
Density gradients (ρ_x, ρ_y)	Typical magnitude	ρ_H	$(\rho_x^*, \rho_y^*) = (\rho_x, \rho_y)/\rho_H$
Sediment Concentration			
Sediment availability (a)	Eq. (A.4)	$\bar{a}$	$a^* = a/\bar{a}$
Sediment concentration (c)	Eq. (A.5)	C	$c^* = c/C$
Vertical diffusivity (K_v)	Eq. (A.2)	$\bar{K}_v$	$K_v^* = K_v/\bar{K}_v$
Settling velocity (w_s)	Typical scale	$\bar{w}_s$	$w_s^* = w_s/\bar{w}_s$

Table A.1: Non-dimensionalization of various physical quantities.

where Len($\partial_R\Omega$) denotes the length of the river boundary.

Finally, the variables used for the concentration equation and the condition for mor-

phodynamic equilibrium are scaled. First, the sediment availability is scaled by the mean amount of sediment available in the estuary for erosion:

$$\bar{a} = \frac{1}{\text{Ar}(\Omega)} \iint_{\Omega} a \, d\Omega, \tag{A.4}$$

where $\text{Ar}(\Omega)$ denotes the total surface area of the estuary. Using this scale, and requiring that there is an approximate balance between erosion and deposition, it follows that a typical scale for the sediment concentration is given by

$$C = \frac{\rho_s s \bar{a} U}{g' d_s}. \tag{A.5}$$

The settling velocity w_s is scaled with $\bar{w}_\text{s} = \omega H$, i.e., the dimensionless settling velocity w_s^* is the ratio of the tidal time scale and the deposition time scale. We define the parameter ϵ as the ratio of the mean elevation amplitude and the mean water depth at the seaward side, i.e.,

$$\epsilon = \bar{A}/H. \tag{A.6}$$

Using the dimensionless variables listed in Table A.1, the shallow water equations in the dimensionless form read,

$$u_{x^*}^* + v_{y^*}^* + w_{z^*}^* = 0,$$

$$u_{t^*}^* + \epsilon(u^* u_{x^*}^* + v^* u_{y^*}^* + w^* u_{z^*}^*) - f^* v^* = -\left(\frac{L_g}{L}\right)^2 \eta_{x^*}^* - \frac{U_d}{U}(\epsilon\eta^* - z^*)\rho_x^*$$

$$+ \frac{1}{2}\text{S}_\text{v}^2 (A_\text{v}^* u_{z^*}^*)_{z^*},$$

$$v_{t^*}^* + \epsilon(u^* v_{x^*}^* + v^* v_{y^*}^* + w^* v_{z^*}^*) + f^* u^* = -\left(\frac{L_g}{L}\right)^2 \eta_{y^*}^* - \frac{U_d}{U}(\epsilon\eta^* - z^*)\rho_y^*$$

$$+ \frac{1}{2}\text{S}_\text{v}^2 (A_\text{v}^* v_{z^*}^*)_{z^*}.$$

Here L_g is, apart from a factor 2π, the wavelength of the frictionless tidal wave, the vertical Stokes number $\text{S}_\text{v} = \sqrt{2\bar{A}_\text{v}/\omega H^2}$ is the ratio of the frictional depth and the wavelength, and $U_d = \frac{gH\rho_H}{\rho_0\omega}$ is the scale for density driven residual circulation.

The boundary condition at the seaward side (Eq. 4.3) becomes

$$\eta^* = A_{M_2}^* \cos(t^* - \phi_{M_2}) + A_{M_4}^* \cos(2t^* - \phi_{M_4}), \quad \text{for all } (x^*, y^*) \text{ in } \partial_S\Omega^*, \tag{A.7a}$$

where Ω^* denotes the domain in the dimensionless coordinates and $A_{M_2}^*$ and $A_{M_4}^*$ are defined in Table A.1. At the riverine boundary, we find

$$\int_{\partial_R\Omega} \left(\int_{-h^*}^{\epsilon\eta^*} \boldsymbol{u}_\text{h}^* \cdot \hat{\boldsymbol{n}} \, dz^* \right) ds^* = Q^*, \tag{A.7b}$$

where Q^* is defined in Eq. (A.4). At the lateral walls, we have

$$\int_{-h^*}^{\epsilon\eta^*} \boldsymbol{u}_\text{h}^* \cdot \hat{\boldsymbol{n}} \, dz^* = 0, \quad \text{for all } (x^*, y^*) \text{ in } \partial_L\Omega^*, \tag{A.7c}$$

At the free surface $z^* = \epsilon \eta^*$, the boundary conditions become,

$$w^* = \eta_{t^*}^* + \epsilon(u^* \eta_{x^*}^* + v^* \eta_{y^*}^*), \quad \text{and} \quad A_v^*(\boldsymbol{u}_h^*)_{z^*} = \boldsymbol{0}_h, \tag{A.7d}$$

and at the bottom $z^* = -h^*$, they read

$$w^* = -u^* h_{x^*}^* - v^* h_{y^*}^* \quad \text{and} \quad A_v^*(\boldsymbol{u}_h^*)_{z^*} = \frac{sH}{\bar{A}_v} \boldsymbol{u}_h^*. \tag{A.7e}$$

The three-dimensional advection-diffusion equation governing the suspended sediment concentration in dimensionless form reads,

$$c_{t^*}^* + \epsilon \left[(c^* u^*)_{x^*} + (c^* v^*)_{y^*} + (c^* w^*)_{z^*} \right] - \frac{K_h}{\omega L^2} \left[c_{x^* x^*}^* + c_{y^* y^*}^* \right]$$

$$- \frac{\bar{K}_v}{\omega H^2} (K_v^* c_{z^*}^*)_{z^*} - w_s^* c_{z^*}^* = 0. \tag{A.8}$$

Since we assume that $K_v = A_v$, it follows that $\bar{K}_v / \omega H^2 = \frac{1}{2} S_v^2$. The boundary condition for suspended sediment concentration at the free surface reads

$$-\epsilon \frac{K_h}{\omega L^2} \left[c_{x^*}^* \eta_{x^*}^* + c_{y^*}^* \eta_{y^*}^* \right] + w_s^* c^* + \frac{\bar{K}_v}{\omega H^2} K_v^* c_{z^*}^* = 0, \quad \text{at} \quad z^* = \epsilon \eta^*, \tag{A.9a}$$

and at the bottom

$$-\frac{K_h}{\omega L^2} (c_{x^*}^* h_{x^*}^* + c_{y^*}^* h_{y^*}^*) - \frac{\bar{K}_v}{\omega H^2} K_v^* c_{z^*}^* = w_s^* a^* \sqrt{u^{*2} + v^{*2}}, \quad \text{at} \quad z^* = -h^*. \tag{A.9b}$$

The condition of morphodynamic equilibrium in the dimensionless form becomes,

$$\left\langle \frac{\partial}{\partial x^*} \int_{-h^*}^{\epsilon \eta^*} \left(\epsilon c^* u^* - \frac{K_h}{\omega L^2} c_{x^*}^* \right) \mathrm{d}z^* + \frac{\partial}{\partial y^*} \int_{-h^*}^{\epsilon \eta^*} \left(\epsilon c^* v^* - \frac{K_h}{\omega L^2} c_{y^*}^* \right) \mathrm{d}z^* \right\rangle = 0. \tag{A.10}$$

A.2. PERTURBATION ANALYSES

For the estuaries under consideration, the typical elevation amplitude is much smaller than the typical water depth,

$$\epsilon = \frac{\bar{A}}{H} \ll 1. \tag{A.11}$$

Using this information, we can asymptotically expand the vector of unknown physical variables $\boldsymbol{\psi}^* = (\eta^*, u^*, v^*, w^*, c^*)$ as

$$\boldsymbol{\psi}^* = \boldsymbol{\psi}^{0*} + \epsilon \boldsymbol{\psi}^{1*} + \epsilon^2 \boldsymbol{\psi}^{2*} + \dots. \tag{A.12}$$

Next, the asymptotic expansion is substituted in the scaled equations and the dimensionless coefficients appearing in these scaled equations are related to different orders in ϵ. A full list of these dimensionless coefficients is given in Table A.2. In the following,

Dimensionless variables	Order
f^*	$\mathcal{O}(1)$
$U/\omega L = \epsilon$	$\mathcal{O}(\epsilon)$
L/L_g	$\mathcal{O}(1)$
U_d/U	$\mathcal{O}(\epsilon)$
$A^*_{M_2}$	$\mathcal{O}(1)$
$A^*_{M_4}$	$\mathcal{O}(\epsilon)$
Q^*	$\mathcal{O}(\epsilon)$
S_v	$\mathcal{O}(1)$
$sH/\bar{A}_v$	$\mathcal{O}(1)$
w^*_s	$\mathcal{O}(1)$
$K_h/\omega L^2$	$\mathcal{O}(\epsilon^2)$

Table A.2: Order of various dimensionless parameters appearing in the dimensionless equations for water motion, suspended sediment concentration and the condition of morphodynamic equilibrium. Refer to Table A.1 for definition of these parameters.

we are going to derive the differential problems for the water motion and suspended sediment concentration, at subsequent orders in ϵ.

With the assumption that $\epsilon \ll 1$, the boundary conditions and integrals evaluated at $z^* = \epsilon\eta^*$ can be simplified. For boundary conditions at river boundary and lateral walls, the integrals from $z^* = -h^*$ to $z^* = \epsilon\eta^*$ can be split into two integrals with limits ranging from $z^* = -h^*$ to $z^* = 0$ and from $z^* = 0$ to $z^* = \epsilon\eta^*$. By using the Taylor expansion of u^* and v^* around $z^* = 0$ in the latter integral, the boundary conditions at the river side and lateral boundaries reduce to

$$\int_{\partial_R\Omega^*} \left[\int_{-h^*}^{0} \boldsymbol{u}^*_h \cdot \hat{\boldsymbol{n}}\, dz^* + \epsilon\eta^* \boldsymbol{u}^*_h|_{z^*=0} \cdot \hat{\boldsymbol{n}} \right] ds^* + \mathcal{O}(\epsilon^2) = -Q^*. \tag{A.13}$$

$$\int_{-h^*}^{0} \boldsymbol{u}^*_h \cdot \hat{\boldsymbol{n}}\, dz^* + \epsilon\eta^* \boldsymbol{u}^*_h|_{z^*=0} \cdot \hat{\boldsymbol{n}} + \mathcal{O}(\epsilon^2) = 0, \quad \text{for all } (x^*, y^*) \text{ in } \partial_C\Omega^*, \tag{A.14}$$

where $\mathcal{O}(\epsilon^2)$ denotes all the terms of the order two or more. Using the same approach, the dimensionless dynamic and kinematic boundary conditions at the free surface $z^* = \epsilon\eta^*$ can be rewritten as

$$w^* + \epsilon\eta^* w^*_{z^*} + \mathcal{O}(\epsilon^2) = \eta^*_{t^*} + \epsilon(u^*\eta^*_x + v^*\eta^*_y) + \mathcal{O}(\epsilon^2), \quad \text{at } z^* = 0, \tag{A.15}$$

$$A^*_v(\boldsymbol{u}^*_h)_{z^*} + \epsilon A^*_v\eta^*(\boldsymbol{u}^*_h)_{z^*z^*} + \mathcal{O}(\epsilon^2) = \boldsymbol{0}_h, \quad \text{at } z^* = 0. \tag{A.16}$$

The boundary condition for the suspended sediment concentration at the free surface becomes,

$$-\epsilon \frac{K_h}{\omega L^2}[c^* + \epsilon\eta^* c^*_{z^*} + \mathcal{O}(\epsilon^2)]_{x^*}\eta^*_{x^*} - \epsilon \frac{K_h}{\omega L^2}[c^* + \epsilon\eta^* c^*_{z^*} + \mathcal{O}(\epsilon^2)]_{y^*}\eta^*_{y^*}$$

$$+ w^*_s[c^* + \epsilon\eta^* c^*_{z^*} + \mathcal{O}(\epsilon^2)] + \frac{\bar{K}_v}{\omega H^2}K^*_v[c^*_{z^*} + \epsilon\eta^* c^*_{z^*z^*} + \mathcal{O}(\epsilon^2)], \quad \text{at } z^* = 0. \tag{A.17}$$

A

Next, the asymptotic expansion of unknown physical variables given by Eq. (A.12) is substituted into the governing equations for water motion, suspended sediment concentration and the condition of morphodynamic equilibrium. Using Table A.2, dimensionless systems of equations are found at different orders of ϵ by collecting terms of equal order.

Leading-order water motion   The leading-order (ϵ^0) system of equations for water motion in the dimensionless form is given by

$$u_{x^*}^{0*} + v_{y^*}^{0*} + w_{z^*}^{0*} = 0,$$

$$u_{t^*}^{0*} - f^* v^{0*} = -\left(\frac{L_g}{L}\right)^2 \eta_{x^*}^{0*} + \frac{1}{2}S_v^2(\bar{A}_v u_{z^*}^{0*})_{z^*},$$

$$v_{t^*}^{0*} + f^* u^{0*} = -\left(\frac{L_g}{L}\right)^2 \eta_{y^*}^{0*} + \frac{1}{2}S_v^2(\bar{A}_v v_{z^*}^{0*})_{z^*},$$

together with boundary conditions

$$A_v^*(\boldsymbol{u}_h^{0*})_{z^*} = \boldsymbol{0}_h, \ \ \text{and} \ \ w^{0*} = \eta_t^{0*}, \ \ \text{at} \ \ z^* = 0,$$

$$A_v^*(\boldsymbol{u}_h^{0*})_{z^*} = \frac{Hs}{\bar{A}_v}\boldsymbol{u}_h^{0*}, \ \ \text{and} \ \ w^{0*} = -u^{0*}h_{x^*}^* - v^{0*}h_{y^*}^*, \ \ \text{at} \ \ z^* = -h^*,$$

$$\eta^{0*} = A_{M_2}^* \cos(t^*) \ \ \text{for all} \ \ (x^*, y^*) \ \text{in} \ \partial_S\Omega^*,$$

$$\int_{\partial_R\Omega^*} \left(\int_{-h^*}^0 \boldsymbol{u}_h^{0*} \cdot \hat{\boldsymbol{n}} \, dz^*\right) ds^* = 0,$$

$$\int_{-h^*}^0 \boldsymbol{u}_h^{0*} \cdot \hat{\boldsymbol{n}} \, dz^* = 0, \ \ \text{for all} \ \ (x^*, y^*) \ \text{in} \ \partial_C\Omega^*.$$

First-order water motion   The first-order (ϵ^1) system of equations for the water motion is given by

$$u_{x^*}^{1*} + v_{y^*}^{1*} + w_{z^*}^{1*} = 0,$$

$$u_{t^*}^{1*} + u^{0*}u_{x^*}^{0*} + v^{0*}u_{y^*}^{0*} + w^{0*}u_{z^*}^{0*} - f^*v^{1*} = -\left(\frac{L_g}{L}\right)^2 \eta_{x^*}^{1*} + \frac{U_d}{U}z^*\rho_x^*$$

$$+\frac{1}{2}S_v^2(\bar{A}_v u_{z^*}^{1*})_{z^*},$$

$$v_{t^*}^{1*} + u^{0*}v_{x^*}^{0*} + v^{0*}v_{y^*}^{0*} + w^{0*}v_{z^*}^{0*} + f^*u^{1*} = -\left(\frac{L_g}{L}\right)^2 \eta_{y^*}^{1*} + \frac{U_d}{U}z^*\rho_y^*$$

$$+\frac{1}{2}S_v^2(\bar{A}_v u_{z^*}^{1*})_{z^*},$$

with boundary conditions

$$(\boldsymbol{u}_{\mathrm{h}}^{1*})_{z^*} = -\eta^{0*}(\boldsymbol{u}_{\mathrm{h}}^{0*})_{z^*z^*},$$

$$w^{1*} = \eta_t^{1*} - (\eta^{0*} w_{z^*}^{0*} - u^{0*} \eta_{x^*}^{0*} - v^{0*} \eta_{y^*}^{0*}) \quad \text{at} \quad z^* = 0,$$

$$A_{\mathrm{v}}^*(\boldsymbol{u}_{\mathrm{h}}^{1*})_{z^*} = \frac{Hs}{\bar{A}_{\mathrm{v}}} \boldsymbol{u}_{\mathrm{h}}^{1*}, \quad \text{and} \quad w^{1*} = -u^{1*} h_{x^*}^* - v^{1*} h_{y^*}^* \quad \text{at} \quad z^* = -h^*,$$

$$\eta^{1*} = A_{M_4}^* \cos(2t^* - \phi) \quad \text{for all} \quad (x^*, y^*) \text{ in } \partial_S \Omega^*,$$

$$\int_{\partial_R \Omega^*} \left[\int_{-h^*}^{0} \boldsymbol{u}_{\mathrm{h}}^{1*} \cdot \hat{\mathbf{n}} \, dz^* + \eta^{0*} \boldsymbol{u}_{\mathrm{h}}^{0*}|_{z^*=0} \cdot \hat{\mathbf{n}} \right] ds^* = -Q^*,$$

$$\int_{-h^*}^{0} \boldsymbol{u}_{\mathrm{h}}^{1*} \cdot \hat{\mathbf{n}} \, dz^* + \eta_0^* \boldsymbol{u}_{\mathrm{h}}^{0*}|_{z^*=0} \cdot \hat{\mathbf{n}} = 0, \quad \text{for all} \quad (x^*, y^*) \text{ in } \partial_C \Omega^*.$$

Leading-order suspended sediment concentration The leading-order (ϵ^0) system of equations for the suspended sediment concentration is given by

$$c_{t^*}^{0*} - \frac{\bar{K}_{\mathrm{v}}}{\omega H^2} \left(K_{\mathrm{v}}^* c_{z^*}^{0*} \right)_{z^*} - (w_s^* c^{0*})_{z^*} = 0,$$

with boundary conditions

$$-\frac{\bar{K}_{\mathrm{v}}}{\omega H^2} K_{\mathrm{v}}^* c_{z^*}^{0*} = w_s^* c^{0*}, \quad \text{at} \quad z^* = 0,$$

$$-\frac{\bar{K}_{\mathrm{v}}}{\omega H^2} K_{\mathrm{v}}^* c_{z^*}^{0*} = w_s^* a^* |\boldsymbol{u}_{\mathrm{h}}^{0*}|, \quad \text{at} \quad z^* = -h^*.$$

The above equation shows that the leading-order suspended sediment concentration is solely governed by the absolute value of the leading-order horizontal velocity.

First-order suspended sediment concentration The first-order (ϵ^1) system of equations for the suspended sediment concentration is given by

$$c_{t^*}^{1*} + u^{0*} c_{x^*}^{0*} + v^{0*} c_{y^*}^{0*} + w^{0*} c^{0*} z^* - \frac{\bar{K}_{\mathrm{v}}}{\omega H^2} \left(K_{\mathrm{v}}^* c_{z^*}^{1*} \right)_{z^*} - (w_s^* c^{1*})_{z^*} = 0,$$

with boundary conditions

$$\frac{\bar{K}_{\mathrm{v}}}{\omega H^2} K_{\mathrm{v}}^* \left[c_{z^*}^{1*} + \eta_0^* c_{z^*z^*}^{0*} \right] + w_s^* \left[c^{1*} + \eta^{0*} c_{z^*}^{0*} \right] = 0 \quad \text{at} \quad z = 0,$$

$$\frac{\bar{K}_{\mathrm{v}}}{\omega H^2} K_{\mathrm{v}}^* c_{z^*}^{1*} + w_s^* a^* \frac{\boldsymbol{u}_{\mathrm{h}}^{0*} \cdot \boldsymbol{u}_{\mathrm{h}}^{1*}}{|\boldsymbol{u}_{\mathrm{h}}^{0*}|} = 0, \quad \text{at} \quad z^* = -h^*.$$

Note that the boundary condition at the bottom $z^* = -h^*$ contains the first-order horizontal velocity $\boldsymbol{u}_{\mathrm{h}}^{1*}$, which as we have seen in the main text (Eq. 3.19), can be written as a sum of various components. It means that the first-order suspended sediment concentration due to the bed shear stress can also be written as sum of various components, one corresponding to each component of the first-order horizontal velocity.

B

LEADING ORDER SCALING ANALYSIS AND WEAK FORMULATION

B.1. SCALING ANALYSIS

The water motion is described by the three-dimensional shallow water equations. Using the Boussinesq approximation and hydrostatic balance, the system of equations can be written as,

$$u_x + v_y + w_z = 0, \tag{B.1a}$$

$$u_t + u u_x + v u_y + w u_z - f v = -g \eta_x - \frac{g}{\rho_o}(\eta - z)\rho_x$$
$$+ (A_h u_x)_x + (A_h u_y)_y + (A_v u_z)_z, \tag{B.1b}$$

$$v_t + u v_x + v v_y + w v_z + f u = -g \eta_y - \frac{g}{\rho_o}(\eta - z)\rho_y$$
$$+ (A_h v_x)_x + (A_h v_y)_y + (A_v v_z)_z. \tag{B.1c}$$

It is assumed that the estuary is partially to well mixed such that the density can be approximated as $\rho := \rho(x, y, t)$. A_h is the coefficient of horizontal mixing. To scale the equations, the following dimensionless variables are introduced;

$$t^* = \omega t, \quad f^* = f/\omega, \quad (x^*, y^*) = (x, y)/L,$$
$$(z^*, h^*) = (z, h)/H, \quad u^* = u/U, \quad v^* = v/V, \quad w^* = w/W,$$
$$\eta^* = \eta/A, \quad \rho_x^* = \rho_x/|\rho_x|, \quad \rho_y^* = \rho_y/|\rho_y|,$$

where asterisk ($*$) denotes the dimensionless variables and $\epsilon = A/H \ll 1$, where A is the amplitude of the surface elevation and H is the mean depth at the seaward side, L is the typical length scale, $U = V = \epsilon \omega L$, and $W = \epsilon \omega H$ are the typical scales of tidal velocities.

131

In the above scaling, gradients of the density are scaled instead of the density itself. This is because it is the variation in density that drives density driven currents. The primitive equations in dimensionless form reduce to:

$$u^*_{x^*} + v^*_{y^*} + w^*_{z^*} = 0,$$

$$u^*_{t^*} + \epsilon(u^* u^*_{x^*} + v^* u^*_{y^*} + w^* u^*_{z^*}) - f^* v^*$$

$$= -\frac{gH}{\omega^2 L^2}\eta^*_{x^*} - \frac{gH|\rho_x|}{\rho_o U \omega}(\epsilon\eta^* - z^*)\rho^*_x$$

$$+ \frac{1}{\omega L^2}\left[(A_h u^*_{x^*})_{x^*} + (A_h u^*_{y^*})_{y^*}\right] + \frac{1}{\omega H^2}(A_v u^*_{z^*})_{z^*},$$

$$v^*_{t^*} + \epsilon(u^* v^*_{x^*} + v^* v^*_{y^*} + w^* v^*_{z^*}) + f^* u^*$$

$$= -\frac{gH}{\omega^2 L^2}\eta^*_{y^*} - \frac{gH|\rho_y|}{\rho_o V \omega}(\epsilon\eta^* - z^*)\rho^*_y$$

$$+ \frac{1}{\omega L^2}\left[(A_h v^*_{x^*})_{x^*} + (A_h v^*_{y^*})_{y^*}\right] + \frac{1}{\omega H^2}(A_v v^*_{z^*})_{z^*}.$$

We also assume that the horizontal mixing is much smaller compared to the vertical mixing ([1]), i.e., $A_h H^2/A_v L^2 \ll 1$. With this assumption, x and y momentum equations further reduce to,

$$u^*_{t^*} + \epsilon(u^* u^*_{x^*} + v^* u^*_{y^*} + w^* u^*_{z^*}) - f^* v^*$$

$$= -\frac{gH}{\omega^2 L^2}\eta^*_{x^*} - \frac{gH|\rho_x|}{\rho_o U \omega}(\epsilon\eta^* - z^*)\rho^*_x$$

$$+ \frac{1}{\omega H^2}(A_v u^*_{z^*})_{z^*},$$

$$v^*_{t^*} + \epsilon(u^* v^*_{x^*} + v^* v^*_{y^*} + w^* v^*_{z^*}) + f^* u^*$$

$$= -\frac{gH}{\omega^2 L^2}\eta^*_{y^*} - \frac{gH|\rho_y|}{\rho_o V \omega}(\epsilon\eta^* - z^*)\rho^*_y$$

$$+ \frac{1}{\omega H^2}(A_v v^*_{z^*})_{z^*}.$$

Using typical scales for the density gradients in partially to well mixed estuaries, we find that $\frac{gH}{\rho_0 U \omega}\nabla\rho$ is of order ϵ. Next, we expand the unknown variables. u^*, v^*, w^*, and η^* in the small parameter ϵ,

$$u^* = u^*_0 + \epsilon^1 u^*_1 + \mathcal{O}(\epsilon^2),$$

$$v^* = v^*_0 + \epsilon^1 v^*_1 + \mathcal{O}(\epsilon^2),$$

$$w^* = w^*_0 + \epsilon^1 w^*_1 + \mathcal{O}(\epsilon^2),$$

$$\eta^* = \eta^*_0 + \epsilon\eta^*_1 + \mathcal{O}(\epsilon^2).$$

Substituting the asymptotic expansions in the dimensionless equations results in the following leading-order system of equations,

$$u^*_{0,x^*} + v^*_{0,y^*} + w^*_{0,z^*} = 0,$$
$$u^*_{0,t^*} - f^* v^*_0 = -\frac{gH}{\omega^2 L^2} \eta^*_{0,x^*} + \frac{1}{\omega H^2}(A_v u^*_{0,z^*})_{z^*},$$
$$v^*_{0,t^*} + f^* u^*_0 = -\frac{gH}{\omega^2 L^2} \eta^*_{0,y^*} + \frac{1}{\omega H^2}(A_v v^*_{0,z^*})_{z^*}.$$

In the dimensional form, the system reads

$$u_{0,x} + v_{0,y} + w_{0,z} = 0,$$
$$u_{0,t} - f v_0 = -g\eta_{0,x} + (A_v u_{0,z})_z,$$
$$v_{0,t} + f u_0 = -g\eta_{0,y} + (A_v v_{0,z})_z.$$

For the sake of simplicity we remove the subscript 0 from the variables, i.e., $(\eta_0, u_0, v_0, w_0) = (\eta, u, v, w)$. Similar treatment can be given to the boundary conditions.

B.2. WEAK FORMULATION

To solve the system (2.12) to obtain the surface elevation, the finite element method is adopted ([2]). As a first step towards the finite element method, a weak form of system (2.12) has to be derived. To this end, define $L^2(\Omega)$ and $H^1(\Omega)$ function spaces as

$$L^2(\Omega) = \{\phi \text{ such that } ||\phi||_2 = \left(\iint\limits_\Omega |\phi|^2 \right)^{1/2} < \infty\},$$
$$H^1(\Omega) = \{\phi \in L^2(\Omega) \text{ such that } \phi_x, \phi_y \in L^2(\Omega)\}.$$

Assume that there exists a function N_D in $H^1(\Omega)$ such that $N_D = A$ on $\partial_D\Omega$. Then the function $\tilde{N} = N - N_D$ vanishes over $\partial_D\Omega$ and $N = \tilde{N} + N_D$. Define a function space Σ for test functions as

$$\Sigma = \{\phi \in H^1(\Omega) \text{ such that } \phi = 0 \text{ on } \partial_D\Omega\}.$$

Multiplying Eq. (2.12a) by $\phi \in \Sigma$ and integrating over the domain Ω gives,

$$\iint_\Omega \{\nabla \cdot [\mathbf{D}(0)\nabla N] + i\omega N\}\,\phi\,\mathrm{d}\Omega = 0,$$

$$\Rightarrow \int_{\partial_D\Omega} [\mathbf{D}(0)\nabla N]\cdot\hat{\mathbf{n}}\,\underbrace{\phi}_{=0}\,\mathrm{d}\Omega + \int_{\partial_N\Omega\cup\partial_R\Omega} \underbrace{[\mathbf{D}(0)\nabla N]\cdot\hat{\mathbf{n}}}_{=0}\phi\,\mathrm{d}\Omega$$

$$-\iint_\Omega [\mathbf{D}(0)\nabla N]\cdot\nabla\phi\,\mathrm{d}\Omega + i\omega\iint_\Omega N\phi\,\mathrm{d}\Omega = 0,$$

$$\Rightarrow -\iint_\Omega [\mathbf{D}(0)\nabla N]\cdot\nabla\phi\,\mathrm{d}\Omega + i\omega\iint_\Omega N\phi\,\mathrm{d}\Omega = 0,$$

$$\Rightarrow -\iint_\Omega [\mathbf{D}(0)\nabla(\tilde{N}+N_D)]\cdot\nabla\phi\,\mathrm{d}\Omega + i\omega\iint_\Omega (\tilde{N}+N_D)\phi\,\mathrm{d}\Omega = 0,$$

$$\Rightarrow -\iint_\Omega [\mathbf{D}(0)\nabla\tilde{N}]\cdot\nabla\phi\,\mathrm{d}\Omega + i\omega\iint_\Omega \tilde{N}\phi\,\mathrm{d}\Omega$$

$$= \iint_\Omega [\mathbf{D}(0)\nabla N_D]\cdot\nabla\phi\,\mathrm{d}\Omega - i\omega\iint_\Omega N_D\phi\,\mathrm{d}\Omega. \tag{B.3}$$

Eq. (B.3) is the weak formulation of system (2.12). The solution $N = \tilde{N} + N_D$ obtained after solving the Eq. (B.3) is called the weak solution of system (2.12). This equation is solved numerically.

Let $\tilde{N}_{\tilde{h}}$ denote the finite element approximation of $\tilde{N}$ defined on the discretized domain $\Omega_{\tilde{h}}$ (see main text) as

$$\tilde{N} \approx \tilde{N}_{\tilde{h}} = \sum_{l=1}^{n} N_l \phi_l, \tag{B.4}$$

where $N_l's$ are *unknown* complex coefficients, $\phi_l's$ are so-called Lagrange basis functions. Now, substituting Eq. (B.4) in Eq. (B.3) and choosing $\phi = \phi_k$, $k = 1, \dots, n$ gives

$$\sum_{l=1}^{n} N_l \underbrace{\iint_\Omega [-\mathbf{D}(0)\nabla\phi_l]\cdot\nabla\phi_k}_{[\mathbf{S}]_{k,l}} + \sum_{l=1}^{n} N_l \underbrace{i\omega\iint_\Omega \phi_l\,\phi_k}_{[\mathbf{M}]_{k,l}}$$

$$= \underbrace{\iint_\Omega [\mathbf{D}(0)\nabla N_D]\cdot\nabla\phi_k - i\omega\iint_\Omega N_D\,\phi_k}_{[\mathbf{F}]_k}, \quad \forall k = 1, \dots, n.$$

which can be compactly written as

$$(\mathbf{S}+\mathbf{M})\mathbf{N} = \mathbf{F},$$

where $\mathbf{S}$, $\mathbf{M} \in \mathbb{C}^{n\times n}$ are called the stiffness and mass matrices, respectively. $\mathbf{F} \in \mathbb{C}^{n\times 1}$ is the forcing vector and $\mathbf{N} = \{N_1, N_2, \dots, N_n\}^\mathrm{T} \in \mathbb{C}^{n\times 1}$ is the unknown vector consisting of

complex surface elevation amplitudes at unconstrained nodes. Once **N** is known, we can write the numerical approximation of N over the whole domain as

$$N(x, y) \approx N_{\tilde{h}}(x, y) = \sum_{l=1}^{n} N_l \phi_l(x, y) + \sum_{l=n+1}^{n+m} A(x_l, y_l) \phi_l(x, y).$$

B

REFERENCES

[1] C. D. Winant, *Three-Dimensional Tidal Flow in an Elongated, Rotating Basin,* Journal of Physical Oceanography **37**, 2345 (2007).

[2] M. S. Gockenbach, *Understanding and Implementing the Finite Element Method* (Society of Industrial and Applied Mathematics (SIAM), Philadelphia, 2006).

C

SUSPENDED SEDIMENT CONCENTRATION

C.1. LEADING-ORDER SUSPENDED SEDIMENT CONCENTRATION

The equation governing the leading-order suspended sediment concentration is given by

$$c_t^{0n} - (w_s c^{0n})_z - (K_v c_z^{0n})_z = 0, \quad n = 4m, \text{ where, } m = 0, 1, 2, \ldots$$

such that,

$$K_v c_z^{0n} + w_s c^{0n} = 0 \quad \text{at} \quad z = 0,$$
$$K_v c_z^{0n} + a \frac{w_s \rho_s}{\rho_0 g' d_s} \Re\{\tilde{\boldsymbol{\tau}}_b{}^{0n} e^{\frac{ni\omega t}{2}}\} = 0 \quad \text{at} \quad z = -h,$$

where $\Re\{\tilde{\boldsymbol{\tau}}_b{}^{0n} e^{\frac{ni\omega t}{2}}\}$ is the n-th order harmonics of the absolute value of the leading-order bed shear stress $|\boldsymbol{\tau}_b|^0$. Assuming $c^{0n} = \Re\{C^{0n} e^{\frac{ni\omega t}{2}}\}$, the above equation becomes

$$(K_v C_z^{0n})_z + w_s C_z^{0n} - \frac{ni\omega}{2} C^{0n} = 0.$$

Since $K_v := K_v(x, y)$ and K_h is constant, and using that the above equation is a linear second-order ordinary differential equation in the vertical coordinate z, it can be solved analytically in the vertical for C^{0n}:

$$C^{0n}(x, y, z) = A^{0n}(x, y) e^{r_{n,1} z} + B^{0n}(x, y) e^{r_{n,2} z},$$

where $r_{n,1}$ and $r_{n,2}$ are the roots of the quadratic polynomial equation: $K_v r_n^2 + w_s r_n - \frac{ni\omega}{2} = 0$, and $A^{0n}(x, y)$ and $B^{0n}(x, y)$ are given by

$$A^{0n} = -B^{0n} \frac{w_s + K_v r_{n,2}}{w_s + K_v r_{n,1}},$$

$$B^{0n} = a \frac{w_s \rho_s \tilde{\boldsymbol{\tau}}_b^{0n}}{\rho_0 g' d_s K_v} \left[\frac{w_s + K_v r_{n,1}}{r_{n,1} e^{-r_{n,1} h}(w_s + K_v r_{n,2}) - r_{n,2} e^{-r_{n,2} h}(w_s + K_v r_{n,1})} \right].$$

We can rewrite c^0 as

$$c^0 = a \tilde{c}^0,$$

where $\tilde{c}^0$ is the solution of the leading-order suspended sediment concentration with $a = 1$.

C.2. FIRST-ORDER SUSPENDED SEDIMENT CONCENTRATION

The equation governing the first-order suspended sediment concentration c^1 is given by

$$c_t^1 + F_{AC}^c - (K_v c_z^1)_z - (w_s c^1)_z = 0, \tag{C.1a}$$

where $F_{AC}^c = u^0 c_x^0 + v^0 c_y^0 + w^0 c_z^0$. At the surface, the boundary condition reads

$$w_s c^1 + K_v c_z^1 = F_S^c, \quad \text{at} \ \ z = 0, \tag{C.1b}$$

where $F_S^c = -\eta_0 \left[w_s c_z^0 + K_v c_{zz}^0 \right]$. At the bottom, the boundary condition reads

$$K_v c_z^1 + a \frac{w_s \rho_s}{\rho_0 g' d_s} |\boldsymbol{\tau}_b|^1 = 0, \quad \text{at} \ \ z = -h. \tag{C.1c}$$

Here $|\boldsymbol{\tau}_b|^1$ denotes the first-order component of the absolute value of the bed shear stress. Next, the first-order suspended sediment concentration is solved each forcing term individually.

C.2.1. CONTRIBUTION DUE TO ADVECTION

The forcing term F_{AC}^c appearing in Eq. (C.1) is generated by the interaction of leading-order velocity and the leading-order suspended sediment concentration can be expressed as

$$F_{AC}^c = a F_{AC}^a + a_x F_{AC}^{a_x} + a_y F_{AC}^{a_y},$$

where $F_{AC}^a = \tilde{c}_x^{0a} u^0 + \tilde{c}_y^{0a} v^0 + \tilde{c}_z^{0a} w^0$, $F_{AC}^{a_x} = \tilde{c}^{0a} u^0$, and $F_{AC}^{a_y} = \tilde{c}^{0a} v^0$ are the components proportional to a, a_x, and a_y, respectively. Since we are interested in the M_2 constituent of the first-order concentration, we can write

$$(F_{AC}^a, F_{AC}^{a_x}, F_{AC}^{a_y}, c_{AC}^{12}) = \Re\{(f_{AC}^a, f_{AC}^{a_x}, f_{AC}^{a_y}, C_{AC}^{12}) e^{i\omega t}\}.$$

Now, the governing equation becomes,

$$(K_v C^{12}_{AC,z})_z + w_s C^{12}_{AC,z} - i\omega C^{12}_{AC} = a f^c + a_x f^{a_x}_{AC} + a_y f^{a_y}_{AC}, \qquad (C.2)$$

with boundary conditions

$$K_v c^{12}_{AC,z} + w_s C^{12}_{AC} = 0, \text{ at } z = 0,$$
$$K_v c^{12}_{AC,z} = 0 \text{ at } z = -h.$$

This equation can be solved analytically for C^{12}_{AC} for each forcing $\tilde{f}$ on the right hand side separately using the method of variation of parameters, resulting in

$$C^{12}_{AC}(x,y,z) = A e^{r_1 z} + B e^{r_2 z} + \frac{1}{r_2 - r_1} \int_{-h}^{z} [e^{r_2(z-z')} - e^{r_1(z-z')}] \tilde{f}(z')\, dz',$$

where r_1, r_2 are the roots of the quadratic polynomial

$$K_v r^2 + w_s r - i\omega = 0,$$

and coefficients A and B are given as

$$A = -\frac{r_2 e^{-r_2 h}}{r_2 - r_1} \int_{-h}^{0} \left[\frac{(K_v r_2 + w_s) e^{-r_2 z} - (K_v r_1 + w_s) e^{-r_1 z}}{r_2 (K_v r_1 + w_s) e^{-r_2 h} - r_1 (K_v r_2 + w_s) e^{-r_1 h}} \right] \tilde{f}(z)\, dz,$$
$$B = -A \frac{r_1}{r_2} e^{(r_2 - r_1)h}.$$

The complete solution can be written as

$$C^{12}_{AC} = a \tilde{C}^{12,a}_{AC} + a_x \tilde{C}^{12,a_x}_{AC} + a_y \tilde{C}^{12,a_y}_{AC},$$

where $\tilde{C}^{12,a}_{AC}$, $\tilde{C}^{12,a_x}_{AC}$ and $\tilde{C}^{12,a_y}_{AC}$ are the solutions of the above equation for $a = 1$, $a_x = 1$ and $a_y = 1$, respectively. Note that when computing the solution for $a = 1$, a_x and a_y are set to zero. The similar strategy holds when computing the solution for $a_x = 1$ ($a = 0$ and $a_y = 0$) and $a_y = 1$ ($a = 0$ and $a_x = 0$). The M_2 concentration c^{12}_{AC} can thus be expressed as

$$c^{12}_{AC} = a \tilde{c}^{12,a}_{AC} + a_x \tilde{c}^{12,a_x}_{AC} + a_y \tilde{c}^{12,a_y}_{AC},$$

where,

$$(\tilde{c}^{12,a}_{AC}, \tilde{c}^{12,a_x}_{AC}, \tilde{c}^{12,a_y}_{AC}) = \Re\{(\tilde{C}^{12,a}_{AC}, \tilde{C}^{12,a_x}_{AC}, \tilde{C}^{12,a_y}_{AC}) e^{i\omega t}\}.$$

C.2.2. Contribution due to first-order bed-shear stress
See the main text.

C.2.3. CONTRIBUTION DUE TO FORCING AT THE SURFACE

The M_2 component of the surface boundary contribution $F_S^c = -\eta^0 \left[w_s c_z^0 + K_v c_{zz}^0 \right]$ can be expressed at $\Re\{a f_S^c e^{i\omega t}\}$. Writing $c_S^{12} = \Re\{C_S^{12} e^{i\omega t}\}$, the equation governing the first-order sediment concentration due to forcing at the surface reads

$$(w_s C_S^{12})_z + (K_v C_{S,z}^{12})_z - i\omega C_S^{12} = 0,$$

together with the boundary conditions,

$$K_v C_{S,z}^{12} + w_s C_S^{12} = a f_S^c, \quad \text{at} \ \ z = 0,$$
$$K_v C_{S,z}^{12} = 0, \quad \text{at} \ \ z = -h.$$

This equation can be solved analytically in the vertical as

$$C_S^{12} = A e^{r_1 z} + B e^{r_2 z},$$

where r_1, r_2 are the roots of the polynomial $K_v r^2 + w_s r - i\omega = 0$ and the coefficients A and B are given by

$$A = a \left[\frac{r_2 r^{r_1 h}}{r_2 (w_s + K_v r_1) e^{r_1 h} - r_1 (w_s + K_v r_2) e^{r_2 h}} \right] f_S^c,$$
$$B = -A \frac{r_1}{r_2} e^{(r_2 - r_1) h}.$$

D

CONDITION OF MORPHODYNAMIC EQUILIBRIUM

The condition of morphodynamic equilibrium reads

$$\langle \frac{\partial}{\partial x} \int_{-h}^{\eta} \left(cu - K_{\mathrm{h}} \frac{\partial c}{\partial x} \right) \mathrm{d}z + \frac{\partial}{\partial y} \int_{-h}^{\eta} \left(cv - K_{\mathrm{h}} \frac{\partial c}{\partial y} \right) \mathrm{d}z \rangle = 0. \tag{D.1}$$

Using the dimensionless variables introduced in Eq. (A.1) of A, the above equation becomes

$$\langle \frac{\partial}{\partial x^*} \int_{-h^*}^{\epsilon \eta^*} \left(\epsilon c^* u^* - \frac{K_{\mathrm{h}}}{\omega L^2} c_{x^*}^* \right) \mathrm{d}z^* + \frac{\partial}{\partial y^*} \int_{-h^*}^{\epsilon \eta^*} \left(\epsilon c^* v^* - \frac{K_{\mathrm{h}}}{\omega L^2} c_{y^*}^* \right) \mathrm{d}z^* \rangle = 0. \tag{D.2}$$

First, we will consider the first term in Eq. (D.2). The integral from $z^* = -h^*$ to $z^* = \epsilon \eta^*$ can be split into two integrals; one from $z^* = -h^*$ to $z^* = 0$ and one from $z^* = 0$ to $z^* = \epsilon \eta^*$ as,

$$\int_{-h^*}^{\epsilon \eta^*} c^* u^* \, \mathrm{d}z^* = \int_{-h^*}^{0} c^* u^* \, \mathrm{d}z^* + \int_{0}^{\epsilon \eta^*} c^* u^* \, \mathrm{d}z^*.$$

The asymptotic expansions of c^* and u^* can be used directly in the first integral,

$$\int_{-h^*}^{0} c^* u^* \, \mathrm{d}z^* = \int_{-h^*}^{0} \left[c^{0*} u^{0*} + \epsilon (c^{0*} u^{1*} + c^{1*} u^{0*}) + \mathcal{O}(\epsilon^2) \right] \, \mathrm{d}z^*,$$

while for the second integral, c^* and u^* are first expanded around $z^* = 0$ using the Taylor series expansion and then asymptotic expansions of c^* and u^* are used,

$$\int_0^{\epsilon\eta^*} c^* u^* \, dz^* = \int_0^{\epsilon\eta^*} \left[(c^* u^*)|_{z^*=0} + z^* (c^* u^*)_{z^*}|_{z^*=0} + \dots \right] dz^*,$$

$$= \epsilon \left[\eta^* (c^* u^*)|_{z^*=0} + \epsilon \frac{\eta^{*2}}{2} (c^* u^*)_{z^*}|_{z^*=0} + \mathcal{O}(\epsilon^2) \right],$$

$$= \epsilon \eta^{0*} c^{0*} u^{0*}|_{z^*=0} + \epsilon^2 \left[\eta^{0*} c^{0*} u^{1*}|_{z^*=0} + \eta^{0*} c^{1*} u^{0*}|_{z^*=0} \right.$$

$$\left. + \eta^{1*} c^{0*} u^{0*}|_{z^*=0} + \frac{(\eta^{0*})^2}{2} (c^{0*} u^{0*})_{z^*}|_{z^*=0} \right] + \mathcal{O}(\epsilon^3).$$

Hence, we have

$$\left\langle \int_{-h^*}^{\epsilon\eta^*} c^* u^* \, dz^* \right\rangle = \int_{-h^*}^0 \langle c^{0*} u^{0*} \rangle \, dz^* + \epsilon \left[\int_{-h^*}^0 \langle c^{0*} u^{1*} + c^{1*} u^{0*} \rangle \, dz^* + \langle \eta^{0*} c^{0*} u^{0*}|_{z^*=0} \rangle \right] + \mathcal{O}(\epsilon^2).$$

Since the leading order concentration itself consists of M_0 and M_4 contributions i.e., $c^{0*} = c^{00*} + c^{04*}$, and the leading-order water motion is semi-diurnal (M_2), the leading-order contribution is $c^{0*} u^{0*} = c^{00*} u^{02*} + c^{04*} u^{02*}$. The first term $c^{00*} u^{02*}$ gives an M_2 signal and the second term $c^{04*} u^{02*}$ both an M_2 and M_6 signal. When averaged over the tidal period, these contributions vanish i.e., $\langle c^{00*} u^{02*} \rangle = \langle c^{04*} u^{02*} \rangle = 0$, implying that $\langle c^{0*} u^{0*} \rangle = 0$.

The first-order velocity u^{1*} consists of an M_0 and M_4 contributions, resulting in

$$c^{0*} u^{1*} = (c^{00*} + c^{04*})(u^{10*} + u^{14*}) = c^{00*} u^{10*} + c^{00*} u^{14*} + c^{04*} u^{10*} + c^{04*} u^{14*}.$$

In the above expression, on the extreme right, the first term gives an M_0 contribution, the second and third terms both give M_4 contributions, and the fourth term gives an M_0 and M_4 contribution. When averaged over a tidal period, all contributions vanish except the residual (M_0) ones, i.e., $\langle c^{0*} u^{1*} \rangle = c^{00*} u^{10*} + \langle c^{04*} u^{14*} \rangle$.

The first-order suspended sediment concentration contains an M_2 contribution i.e., $c^{1*} = c^{12*}$, resulting in $\langle c^{1*} u^{0*} \rangle = \langle c^{12*} u^{02*} \rangle$. Using this information, it follows that

$$\left\langle \int_{-h^*}^{\epsilon\eta^*} c^* u^* \, dz^* \right\rangle = \epsilon \left[\int_{-h^*}^0 c^{00*} u^{10*} + \langle c^{04*} u^{14*} + c^{12*} u^{02*} \rangle \, dz^* + \langle \eta^{0*} c^{0*} u^{0*}|_{z^*=0} \rangle \right] + \mathcal{O}(\epsilon^2).$$

Next, we will derive the leading-order contribution to the second term in Eq. (D.2). Again, we split the integral in two parts:

$$\int_{-h^*}^{\epsilon\eta^*} c_{x^*}^* \, dz^* = \int_{-h^*}^0 c_{x^*}^* \, dz^* + \int_0^{\epsilon\eta^*} c_{x^*}^* \, dz^*.$$

Using the same approach as above, we find that

$$\left\langle \int_{-h^*}^{\epsilon\eta^*} c_{x^*}^* \, dz^* \right\rangle = \int_{-h^*}^0 \langle c_{x^*}^{0*} \rangle \, dz^* + \epsilon \left[\int_{-h^*}^0 \langle c_{x^*}^{1*} \rangle \, dz^* + \langle \eta^{0*} (c^{0*}|_{z^*=0})_{x^*} \rangle \right] + \mathcal{O}(\epsilon^2).$$

In a similar way as above, we find that

$$c^{0*} = c^{00*} + c^{04*} \Rightarrow \langle c_{x^*}^{0*}\rangle = c_{x^*}^{00*},$$

$$c^{1*} = c^{12*} \Rightarrow \langle c_{x^*}^{1*}\rangle = 0,$$

$$\eta^{0*}c^{0*} = \eta^{02*}(c^{00*} + c^{04*}) = \underbrace{\eta^{02*}c^{00*}}_{M_2} + \underbrace{\eta^{02*}c^{04*}}_{M_2+M_6} \Rightarrow \langle \eta^{0*}c^{0*}\rangle = 0.$$

Hence the second term in Eq. (D.2) after averaging over a tidal period becomes,

$$\langle \int_{-h^*}^{\epsilon\eta^*} c_{x^*}^* \, dz^* \rangle = \int_{-h^*}^{0} c_{x^*}^{00*} \, dz^* + \mathcal{O}(\epsilon^2).$$

Hence we obtain,

$$\langle \partial_{x^*} \int_{-h^*}^{\epsilon\eta^*} \left(\epsilon c^* u^* - \frac{K_h}{\omega L^2} c_{x^*}^*\right) dz^* \rangle = \epsilon^2 \partial_{x^*} \Big[\int_{-h^*}^{0} c^{00*} u^{10*} + \langle c^{04*} u^{14*} + c^{12*} u^{02*}\rangle \, dz^*$$
$$+ \langle \eta^{0*} c^{0*} u^{0*}|_{z^*=0}\rangle \Big] - \frac{K_h}{\omega L^2} \partial_{x^*} \int_{-h^*}^{0} c_{x^*}^{00*} \, dz^* + \mathcal{O}(\epsilon^3).$$
$$\text{(D.3)}$$

Repeating the same procedure for the third and fourth terms of Eq. (D.2) gives,

$$\langle \partial_{y^*} \int_{-h^*}^{\epsilon\eta^*} \left(\epsilon c^* v^* - \frac{K_h}{\omega L^2} c_{y^*}^*\right) dz^* \rangle = \epsilon^2 \partial_{y^*} \Big[\int_{-h^*}^{0} c^{00*} v^{10*} + \langle c^{04*} v^{14*} + c^{12*} v^{02*}\rangle \, dz^* + \langle \eta^{0*} c^{0*} v^{0*}|_{z^*=0}\rangle \Big]$$
$$- \frac{K_h}{\omega L^2} \partial_{y^*} \int_{-h^*}^{0} c_{y^*}^{00*} \, dz^* + \mathcal{O}(\epsilon^3).$$
$$\text{(D.4)}$$

Using Eqs. (D.3) and (D.4) in Eq. (D.2), collecting leading-order terms and transforming back in to dimensional form gives,

$$\partial_x \left(\int_{-h}^{0} \left[u^{10} c^{00} + \langle u^{14} c^{04} + u^{02} c^{12}\rangle \right] dz + \langle \eta^{02} u^{02} c^0|_{z=0}\rangle - K_h \int_{-h}^{0} c_x^{00} dz \right)$$
$$+ \partial_y \left(\int_{-h}^{0} \left[v^{10} c^{00} + \langle v^{14} c^{04} + v^{02} c^{12}\rangle \right] dz + \langle \eta^{02} v^{02} c^0|_{z=0}\rangle - K_h \int_{-h}^{0} c_y^{00} dz \right) = 0. \quad \text{(D.5)}$$

Next, using the relations,

$$(c^0, c^{00}, c^{04}) = a(\tilde{c}^{0a}, \tilde{c}^{00a}, \tilde{c}^{04a}), \text{ and } c^{12} = a\tilde{c}^{12a} + a_x \tilde{c}^{12a_x} + a_y \tilde{c}^{12a_y},$$

and defining the following components:

$$(T_{M_0}^{xa}, T_{M_0}^{ya}) = \int_{-h}^{0} \boldsymbol{u}_h^{10} \tilde{c}^{00a} \, dz, \quad (T_{M_2}^{xa}, T_{M_2}^{ya}) = \int_{-h}^{0} \langle \boldsymbol{u}_h^{02} \tilde{c}^{12a}\rangle \, dz,$$

$$(T_{M_2}^{xa_x}, T_{M_2}^{ya_x}) = \int_{-h}^{0} \langle \boldsymbol{u}_h^{02} \tilde{c}^{12a_x}\rangle \, dz, \quad , (T_{M_2}^{xa_y}, T_{M_2}^{ya_y}) = \int_{-h}^{0} \langle \boldsymbol{u}_h^{02} \tilde{c}^{12a_y}\rangle \, dz$$

$$(T_{M_4}^{xa}, T_{M_4}^{ya}) = \int_{-h}^{0} \langle \boldsymbol{u}_h^{14} \tilde{c}^{04a}\rangle \, dz, \quad (T_{\text{surface}}^{xa}, T_{\text{surface}}^{ya}) = \langle \eta^{02} \boldsymbol{u}_h^{02} \tilde{c}^{0a}|_{z=0}\rangle,$$

$$(T_{\text{diff}}^{xa}, T_{\text{diff}}^{ya}) = -K_h \int_{-h}^{0} (\tilde{c}_x^{00a}, \tilde{c}_y^{00a}) \, dz, \quad D_{K_h} = -K_h \int_{-h}^{0} \tilde{c}^{00a} \, dz,$$

we can write the total horizontal sediment transport vector $\mathbf{T} = (T^{xa}, T^{ya})$ as

$$
(T^{xa}, T^{ya}) = (T^{xa}_{M_0}, T^{ya}_{M_0}) + (T^{xa}_{M_2}, T^{ya}_{M_2}) + (T^{xa}_{M_4}, T^{ya}_{M_4}) + (T^{xa}_{\text{surface}}, T^{ya}_{\text{surface}})
$$
$$
+ (T^{xa}_{\text{diff}}, T^{ya}_{\text{diff}}). \tag{D.6}
$$

Collecting terms that result from horizontal diffusivity explicitly, together with advective contributions that exhibit diffusive behaviour, we can define a diffusivity matrix $\mathbf{D}^a$ for the sediment availability $a(x, y)$ as

$$
\mathbf{D}^a = \begin{pmatrix} D_{K_{\text{h}}} + T^{xa_x}_{M_2} & T^{xa_y}_{M_2} \\ T^{ya_x}_{M_2} & D_{K_{\text{h}}} + T^{ya_y}_{M_2} \end{pmatrix}.
$$

D

Using these results, the condition of morphodynamic equilibrium becomes an elliptic equation for the sediment availability $a(x, y)$ as

$$
\nabla \cdot (\mathbf{D}^a \nabla a + a\mathbf{T}) = 0.
$$

PUBLICATIONS

FIRST AUTHOR

- **M. Kumar**, H. M. Schuttelaars, P. C. Roos, and M. Möller, Three-dimensional semi-idealized model for tidal motion in tidal estuaries: An application to the Ems estuary, Ocean Dynamics 66, pp 99-118, 2016.

- **M. Kumar**, H. M. Schuttelaars, and P. C. Roos, Three-dimensional semi-idealized model for estuarine turbidity maxima in tidally dominated estuaries, Ocean Modelling 113, pp 1-21, 2017.

CO-AUTHOR

- X. Wei, **M. Kumar**, and H. M. Schuttelaars, Three-Dimensional Sediment Dynamics in Well-Mixed Estuaries: Importance of the Internally Generated Overtide, Spatial Settling Lag, and Gravitational Circulation, Journal of Geophysical Research: Oceans, 123 (2), pp. 1062-1090, 2018.

- X. Wei, **M. Kumar**, and H. M. Schuttelaars, Three-dimensional salt dynamics in well-mixed estuaries: Influence of estuarine convergence, Coriolis, and bathymetry, Journal of Physical Oceanography 47 (7) pp. 1843-1871, 2017.

- W. L. Chen, P. C. Roos, H. M. Schuttelaars, **M. Kumar**, T. J. Zitman, and S. J. M. H. Hulscher, Response of large-scale coastal basins to wind forcing: influence of topography, Ocean Dynamics 66, pp 549-565, 2016.